Laser Ion-Acceleration from tailored Micro-Plasmas

Johannes Gebhard

München 2022

Laser Ion-Acceleration from tailored Micro-Plasmas

Dissertation

an der Fakultät für Physik
Ludwig–Maximilians–Universität München

vorgelegt von

Johannes Gebhard
geboren in Eichstätt

München, den 29.06.2022

Erstgutachter: Prof. Dr. Jörg Schreiber

Zweitgutachter: Prof. Dr. Matt Zepf

Tag der mündlichen Prüfung: 07.09.2022

Kurzfassung

Isolierte Mikrokugeln haben als Target für Experimente mit hochintensiven Laserpulsen ein großes Interesse erzeugt. Dies gilt insbesondere für die lasergetriebene Ionenbeschleunigung. Im Rahmen dieser Arbeit wurde unser einzigartiges, auf einer Paul-Falle basierendes Targetpositionierungssystem erheblich verbessert und für eine neuartige Studie mit relativistischen Hochleistungslaserpulsen eingesetzt. Unter anderem wurde das Paul-Fallen System mit einer vollständigen Fernsteuerung erweitert, was die Zuverlässigkeit erhöht und einen Schussbetrieb mit einer Wiederholungsrate von einem Schuss pro zehn Minuten gewährleistet. Dies ermöglichte zum ersten Mal ausgedehnte Mehrschuss Studien mit Targets, die kleiner als die Fokusgröße sind.
Diese Fähigkeit wurde während einer experimentellen Kampagne am JETi-Laser demonstriert, bei der mehr als 200 Schüsse auf sphärische Targets durchgeführt wurden. Das wissenschaftliche Neuland dieser Studie zur Laser-Ionen-Beschleunigung besteht darin, dass ein schwächerer Laserpuls die Mikrokugel vor der Wechselwirkung mit dem Hauptlaserpuls kontrolliert zündet. Dadurch interagiert der relativistische Laserpuls effektiv mit einem mikroskopischen Plasma mit reduzierter Dichte. In diesen Fällen stieg die Ausbeute beschleunigter Protonen im Vergleich zu nicht expandierten, sphärischen Targets um bis zu einem Faktor 19 an, womit ein vorwärts gerichteter Strahl anzunehmen ist. Wir finden eine ausgeprägte, hochenergetische Protonenkomponente mit maximalen Protonenenergien von bis zu 27 MeV. Dies entspricht im Vergleich zu planaren Folientargets, die im gleichen Aufbau mit dem Laserpuls bestrahlt wurden, einer Verdopplung der maximalen Protonenenergie. Der Wirkungsgrad bei der Umsetzung von Laserenergie in maximale Protonenenergie beträgt 18 MeV/J. Dies entspricht ca. einer um den Faktor zwei verbesserten Performance im Vergleich zum Optimum von 10 MeV/J, der üblicherweise für Folientargets angegeben wird.
Die experimentellen Ergebnisse werden durch 3D3V-PIC-Simulationen unterstützt,

welche die experimentellen Protonen- und Kohlenstoffspektren über einen weiten Bereich von Targetdichten und Beschleunigungsmechanismen gut reproduzieren. Die energiereichsten Protonen, die wir für expandierte Targets beobachtet haben, lassen sich auf einen Plasmadichtebereich zurückführen, der knapp oberhalb der relativistischen Plasmadichte liegt. Hier haben wir eine effiziente Hole-Boring Phase im ansteigenden Dichteprofil, bei zeitgleichem Anstieg der Intensität des Laserpulses, identifiziert. Unter idealen Bedingungen werden die vorbeschleunigten Protonen in den Plasmafeldern nachbeschleunigt, wo sie ihre Energie nahezu verdoppeln. Die Skalierung der Simulationen auf höhere Laserpulsenergien sagt einen Anstieg der Protonenenergien mit der Quadratwurzel der Laserenergie voraus. Insbesondere scheinen in den Simulationen 4 J ausreichend, um mehr als 100 MeV Protonen zu erreichen, die das Fenster zum medizinisch relevanten Energiebereich öffnen.

Abstract

Levitating, isolated micro-spheres have gained interest as target in high intensity laser plasma experiments, in particular for laser-driven ion acceleration. Within this thesis, our unique Paul-trap based target positioning system was significantly improved and employed for a novel study with relativistic high power laser pulses. Among others, the Paul-trap system was equipped with full remote control capabilities, increasing its reliability and enabling operation at a rate of one shot every ten minutes. This enabled extended multi-shot studies using sub-focus sized targets for the first time.

This capability was demonstrated during an experimental campaign at the JETi laser, where more than 200 shots on spherical targets were conducted. The scientific novelty of this study in laser-ion acceleration was that a weaker laser pulse ignited the micro-sphere at controlled times before the interaction with the main laser pulse. Therefore, the relativistic laser pulse effectively interacted with a microscopic plasma at reduced density. In these cases, accelerated proton yield increased by up to a factor of 19 as compared to non-expanded spherical targets and indicate a forward-directed beam. We find a distinct, high energetic proton component with maximum energies of up to 27 MeV, which is more than 2 times higher compared to planar foil targets irradiated with laser pulse in the same setup. The laser energy to proton maximum energy conversion efficiency is 18 MeV/J. This is also a factor of 2 larger compared to the optimum of 10 MeV/J that is commonly stated for foil targets.

The experimental results are supported by 3D3V-PIC simulations that reproduce experimental proton and carbon spectra over a wide range of target densities and acceleration mechanisms well. The most energetic protons that we observed for expanded targets can be attributed to a plasma density range that is just above the relativistic plasma density. Here, we identify an efficient hole-boring phase in the upramp of the density profile during the intensity rise of the laser pulse.

Under ideal conditions, the pre-accelerated protons undergo post acceleration in the plasma fields where they nearly double their energy. Scaling the simulations to larger laser pulse energies predicts an increase of the proton energies with the square root of the laser energy, in particular 4 J seem sufficient for reaching more than 100 MeV protons, meeting the relevant window for bio-medical applications.

Contents

Chapter 1

Introduction

Particle accelerators play a fundamental role in industry, pharmacy, science and security. They further resemble a key technology for future wealth and scientific discovery [1]. Fundamental scientific discoveries are frequently based on the development of new accelerating techniques [2]. Since Wideroe [3] set the fundamentals for staged linear accelerators, using alternating potentials together with increasing drift tubes, accelerators have been reduced in size, by increasing the operating frequency of the alternating accelerating structures. Nowadays accelerators are based on resonant cavities. Electric fields form a standing wave, which are designed such that the accelerated particles always reach the next cavity in the right phase to be further accelerated. These structures support accelerating gradients up to 10 MeV/m, [2, 4]. Current accelerator technology used in a scientific context e.g. at CERN[1], DESY[2] or SLAC[3] are large scale facilities with km long accelerators built by multi billion investments, with annual operational costs reaching up to 1 billion dollar [5]. As today's technologies reach economic feasibility, the need for new accelerator technologies becomes ever clearer. One candidate for a further increased operating frequency of the cavities are laser-based accelerators known as dielectric laser-accelerators (DLA) [6]. An even more brute-force approach is to allow the electric break down and apply a non-equilibrium state in a laser-plasma based accelerator.

Even before the demonstration of the first laser by Maiman [7], Veksler [8] proposed a laser-based acceleration scheme in 1957 for charged particles. With the

[1] Conseil europén pour la recherche nucléaire
[2] Deutsche Elektronen-Synchrotron
[3] Stanford Linear Accelerator Center

invention of Chirped Pulse Amplification (CPA), [9] strong enough laser pulses became available for direct laser electron acceleration. This break through in laser amplification technology was awarded with the Nobel Prize in 2018 for Donna Strickland and Gérald Mourou, [10], as it enabled a large number of fs-laser applications. CPA also pushed the current limits of maximum peak intensity above $10^{22}\,\mathrm{W/cm^2}$ [11, 12], which became available [13]. Theses intensities, however, are still not strong enough to reach the threshold for direct proton acceleration (laserfields $> 5 \cdot 10^{24}\,\mathrm{W/cm^2}(\mu\mathrm{m}/\lambda)^2$, [14]). Acceleration of protons thus requires an indirect process, moderated through the electrons in a plasma. Since the demonstration of proton acceleration up to 58 MeV in 2000, [15, 16], laser-plasma-based ion acceleration gained great scientific interest. The most prominent process is known as Target Normal Sheath Acceleration (TNSA), where the direct acceleration of electrons induces charge separation in the plasma. A high-intensity ($I = 1 \times 10^{19} - 1 \times 10^{22}\,\mathrm{W/cm^2}$) laser pulse is focused to a micron-size focal spot size on a thin ($l \approx 1 - 10\,\mu\mathrm{m}$) foil. The target gets ionized, and electrons are accelerated through the foil, forming a sheath field on the target rear side, supporting acceleration gradients in the order of TV/m, which is comparable to the strength of the laser field. Advances in laser- and target technology now also enable the production of thinner foils, and hybrid acceleration schemes such as the break-out-after burner (BOA), [17]. Just recently the barrier for the highest recorded laser-accelerated protons has been increased from 85 MeV [18] to 94 MeV [19]. Laser-accelerated ions typically feature a small source size and ultra low emittance at least 100-fold better than known from conventional accelerators, [20] short bunch length in the order of 3.5 ps [21], and mostly an exponentially decaying energy spectrum towards high particle energies. Motivated by these properties, a research field on the properties theoretically and experimentally has evolved, [14, 22] leading to developments of large scale facilities [4].

Laser-accelerated ions, among many others, find applications in various fields such as material testing [23], bi-modal imaging using X-rays and protons of biological and technical samples [24], as ignitor for fast ignition [25], studies of biological samples [26] or a source for medical applications such as radiation therapy [27, 28]. Recent promising indications of the so called FLASH effect (delivering radiation doses in short time-scales) [29], could be one significant advantage. Oncological studies on mice samples [30] mark a new milestone making use of laser-

accelerated protons for radiation therapy, whereas commercial use is likely still years away.

Even though the maximum proton energy has increased in the recent years, the spectral shape has not changed much, yet is not suitable for most applications. For extended targets, the acceleration process involves physics in intensity ranges covering multiple orders of magnitude starting from the ionization threshold at $10^{13}\,\mathrm{W/cm^2}$, for multi-photon ionization, [31] up to the full relativistic case with peak intensities in excess of $10^{22}\,\mathrm{W/cm^2}$. Additionally, extended targets over ranges of several mm allow lateral electron transport [32], which potentially lowers the accelerating field through electrons being removed from the interaction region. To avoid this boundary effects one ideally limits the interaction to the high intensity area. With focus areas in the $\mu\mathrm{m}^2$ range, this can not be achieved easily. Multiple approaches for mass limited targets have been made by applying structured targets, [33], droplet targets, [34–36], cluster targets [37] or mounting spheres on a needle [38]. All of these targets have in common that they either have a mounting structure or are surrounded by residual gas. Truly isolating particles is known from mass-spectroscopy applying e.g. Paul traps, [39]. Efforts have been made to apply these traps for isolating targets for laser-plasma experiemnts [40] for the cost of reduced repetition rates, as compared to e.g. droplet or foil targets. Our approach facilitates a linear Paul trap [41] that has been specifically designed for the operation at high power lasers. It allows target diameters ranging from 500 nm up to 50 µm covering the size of typical high-power laser focus sizes. Different materials can be researched to find the best parameter set for a specific laser system, that would then allow the design of a specific higher repetition rate droplet target system. Two experimental campaigns at petawatt class laser systems have already been performed at the Texas Petawatt Laser (TPW)[42] and the Petawatt Hoch-Energie Laser für Schwerionenexperimente (PHELIX) [43]. Both systems are glass systems with multi 10 J pulse energies in >150 fs pulse length. While in the ultrahigh contrast regime, a transition from Coulomb explosion to ambipolar expansion [42] was reported, the inherent temporal laser contrast of the PHELIX laser resulted in significant pre-expansion of the target to the near critical density ($n_e \simeq n_c$) area [43]. The reduced density allows for a volumetric interaction of the pulse and the target, which also has gained more and more theoretical interest as a new acceleration scheme [44–47].

In practice high power lasers typically operate at wavelength of $\lambda = 800\,\mathrm{nm} - 1\,\mu\mathrm{m}$, and targets are typically provided using gas jets ($n_e < n_c$)- for under dense laser plasma interaction) or solid targets ($n_e \gg n_c$), while the near critical density area remains a challenge. We approach the near critical density regime by applying a weak pre-pulse ($\approx 10^{16}\,\mathrm{W/cm^2}$) to the spherical target, that undergoes an expansion in the 3 spatial dimensions and thus reducing the integrated area density along the laser axis. The pre-expanded target is then illuminated with a strong focused laser pulse at the best possible temporal laser contrast. As the laser pointing and the particle position are liable to residual fluctuations, multiple shots were taken and best shots selected afterwards.
The thesis is structured as follows:
Chapter 2 introduces the relevant theoretical basis and parameters relevant to this work. It briefly describes the interaction of a laser pulse with a plasma and introduces the most relevant acceleration mechanisms. **Chapter 3** describes the experimental methods. This includes improvements made to the target such as automation and increased reliability of the target replacement process. It also describes the evaluation methods, ion diagnostics and introduces parameters that help in the data selection process. **Chapter 4** presents the experimental results and ion spectra, that have been the result of a six month campaign at the Jenaer Titanium:Sapphire 200 Terawatt Laser System (JETi 200) laser. **Chapter 5** presents accompanied simulations for a detailed understanding of the underlying processes and outlines a scaling of the process towards higher laser energies. **Chapter 6** summarizes the key findings and gives an outlook on upcoming experiments applying higher laser intensities at the Center for Advanced Laser Applications (CALA).

Chapter 2

Light and Matter

The basics of laser matter interaction can be understood in a very simplistic picture. A high intensity laser is focused to a small spot on a target, which typically either is gaseous, liquid or solid. When the laser exceeds a certain threshold intensity, various processes are ionizing the matter and a plasma is formed. A general definition of a plasma according to [48] reads as: *"A plasma is a quasineutral gas of charged and neutral particles which exhibits collective behavior"*. In the plasma state, the strong laser field preferably interacts with the electrons, due to their about 2000 times higher charge to mass ratio as compared to any type of ion. This interaction can break the charge neutrality and in the case of a plasma with high particle density a large electric dipole field of the order of MeV/µm builds up, accelerating the ions initially at rest to high energies. The following section describes the interaction of a laser pulse with matter in a plasma state, the heating mechanism of electrons and finally the processes that accelerate particles to high energies. The following introduction follows [48–50], despite not explicitly stated otherwise.

2.1. Basics about Plasma

A basic characteristic of a plasma is its quasi-neutrality. From a distant point of view the medium seems neutral. The quasi-neutrality can be violated locally. The contrary would mean, that on all scale lengths (even the shortest ones), positive and negative charges would have to sit on top of each other. The scale length, where quasi-neutrality can be violated in a plasma, that is in an equilibrium state

is known as the Debye length. The Debye length also is known as the scale length, on which perturbations in the medium are shielded. Inserting a perturbation into the plasma, e.g. a positive test charge, negative charges will rearrange around this perturbation and create a negative shell around that charge, such that no net charge is visible from the outside. In a case, where the negative charges would have no thermal energy, this effect would perfectly shield the test charge. In a realistic scenario the finite temperature of the negative charges, prohibits a perfect shielding and a net charge can leak out. The Debye length is defined as the length, where the field of the test charge drops to $1/e$ and can be derived as

$$\lambda_D = \sqrt{\frac{\epsilon_0 k_B T_e}{e^2 n_e}}, \tag{2.1}$$

where ϵ_0 is the vacuum permittivity, k_B is the Boltzmann constant, T_e the electron temperature e is the electric charge and n_e is the electron density of the plasma.
In the case of an external distortion, e.g. a laser field, plasma electrons are displaced relative to the uniform ion background. The ion background pulls on the electrons to restore their initial position. Due to their inertia the electrons over shoot and start oscillating around the ions, which do not have sufficient time to react on the electron motion on such short time scales due to their higher mass. The oscillation frequency is known as the plasma frequency

$$\omega_p = \sqrt{\frac{n_e e^2}{\epsilon_0 m_e}}, \tag{2.2}$$

which can also be interpreted as the frequency up to which the plasma can counteract external perturbations. This means that oscillations faster than ω_p can not be compensated by the plasma and a laser pulse with a angular frequency $\omega_L > \omega_p$ can propagate. Contrary, a laser pulse with $\omega_L < \omega_p$ it is reflected at the plasma surface, and the laser pulse can only penetrate up to the skin depth. Thus the point, where $\omega_L = \omega_p$ defines a tipping point, and Eq. (2.2) can be rearranged to define what is known as the critical density

$$n_c = \frac{m_e \epsilon_0 \omega_L^2}{e^2}. \tag{2.3}$$

A plasma which prohibits laser propagation is called an overcritical or overdense plasma, where the case that allows propagation is called underdense or undercritical plasma. The limiting case can also be easily seen by the expression for the refractive index [49] of a (collisionless) plasma

$$\mathrm{n}(\omega_L) = \sqrt{1 - \frac{\omega_p}{\omega_L}}. \tag{2.4}$$

Here one sees that the plasma frequency acts as a cut-off frequency, where the refractive index becomes purely imaginary and prohibits propagation of a wave in the medium. The scale length up to which the field of evanescent wave decays to $1/e$, is the skin depth,

$$\delta_s = \frac{c}{(\omega_p^2 - \omega_L^2)^{1/2}}, \tag{2.5}$$

for an overcritical plasma.

2.2. Intense light field

It is most intuitive to start this discussion from the wave equation for the electric field, which can be derived from Maxwell's equations, where no charge or current is in the region of interest. Maxwell's equation can be recapped using standard textbooks like [51, p. 380 ff]. This yields the two separate equations for the electric- $\vec{E}$ and magnetic $\vec{B}$ field, the so called wave-equations

$$\left(\nabla^2 - \mu_0\epsilon_0\frac{\partial^2}{\partial t^2}\right)\vec{E} = 0 \tag{2.6}$$

$$\left(\nabla^2 - \mu_0\epsilon_0\frac{\partial^2}{\partial t^2}\right)\vec{B} = 0. \tag{2.7}$$

The derivation of the wave equation from Maxwell's equation implies that the speed of light can be calculated from the magnetic and electric permittivity μ_0 and ϵ_0, with $c = (\mu_0\epsilon_0)^{-1/2}$. The simplest solution to the wave equation is given

by a plane wave propagating along the z direction

$$\vec{E}(z,t) = \vec{E}(\vec{r},t)\cos(k_0 z - \omega_L t + \phi_0) \tag{2.8}$$

$$\vec{B}(z,t) = \vec{B}(\vec{r},t)\cos(k_0 z - \omega_L t + \phi_0), \tag{2.9}$$

with the dispersion relation $\omega_L = k_0 c$ and k_0 as the wavenumber and ω_L as the laser frequency. For a plane wave, $\vec{E}(\vec{r},t) = \vec{E}_0$. Faraday's law, $\nabla \times \vec{E} = -\partial\vec{B}/\partial t$ implies that $\vec{B}$ and $\vec{E}$ are perpendicular, yielding the relation

$$B_0 = \frac{k_0}{\omega_L} E_0 = \frac{1}{c} E_0, \tag{2.10}$$

where $B_0 = |\vec{B}_0|$ and $E_0 = |\vec{E}_0|$ are the field amplitudes for linear polarized waves, considered and used throughout this thesis. Finally, from the time average of the pointing vector $\langle\vec{S}\rangle = \langle\mu_0^{-1}(\vec{E}\times\vec{B})\rangle$ over one period, we find the intensity of an electromagnetic wave with linear polarization

$$I_0 = \langle|\vec{S}|\rangle = \frac{1}{2} c\epsilon_0 E_0^2, \tag{2.11}$$

which is the average power per unit area being transported by an electromagnetic wave. Here we can see that the intensity is proportional to the square of the electric (or magnetic) field amplitude. As light also carries momentum $\langle\vec{p}\rangle = c^{-2}\langle\vec{S}\rangle$, we can calculate the radiation pressure as the pressure per unit area that a wave exerts on a perfectly absorbing surface as $P = I/c$. Note that for a perfectly reflecting surface the momentum transfer is twice the initial momentum of the electromagnetic wave, as the wave switches direction. The radiation pressure on the surface then also is twice the pressure of a perfectly absorbing surface. For a Gaussian pulse, the field distribution in focus is

$$\vec{E}(\vec{r},t) = \vec{E}_0 \mathrm{e}^{-t^2/(\sigma_{Et}^2)} \cdot \mathrm{e}^{-x^2/(\sigma_{Ex}^2)} \cdot \mathrm{e}^{-y^2/(\sigma_{Ey}^2)}, \tag{2.12}$$

where σ_{Et}, σ_{Ex} and σ_{Ey} are the pulse length and beam waists along the spatial axes of the electric field. From Eq. (2.11) and Eq. (2.12), we find, that these parameters of the electric field relate to the intensity as $\sigma_I = \sigma_E/\sqrt{2}$ [1], plugging Eq. (2.12) into

[1] For the three quantities this means $\sigma_{It} = \sigma_{Et}/\sqrt{2}$, $\sigma_{Ix} = \sigma_{Ex}/\sqrt{2}$, $\sigma_{Iy} = \sigma_{Ey}/\sqrt{2}$

Eq. (2.11), yields the intensity distribution,

$$I(x,y,t) = I_0 \cdot \mathrm{e}^{-t^2/\sigma_I t^2} \cdot \mathrm{e}^{-x^2/\sigma_{Ix}^2} \cdot \mathrm{e}^{-y^2/\sigma_{Iy}^2}. \tag{2.13}$$

The laser pulse energy is the integral of Eq. (2.13) over space and time, $E = \iiint I(x,y,t)\,dxdydt$. In an experimental setup, the pulse length and spatial extent of the laser beam are measured as Full Width at Half Maximum (FWHM) of the intensity. The FWHM quantities relate to the standard deviation of the Gaussian pulse as $\sigma_{\mathrm{FWHM}} = \sqrt{4\ln(2)\sigma_I^2}$.[2] Evaluating the integral and adding the integration constant, ($N = \sqrt{1/\pi\sigma_I^2} = \sqrt{4\ln(2)/\pi\sigma_{FWHM}^2}$), we find

$$I_0(d_x, d_y, \tau_L) = \left(\frac{4\ln(2)}{\pi}\right)^{3/2} \frac{E}{\tau_L d_x d_y} \approx 0.83 \cdot \frac{E}{\tau_L d_x d_y}, \tag{2.14}$$

for the experimentally available parameters. Besides dedicated experiments [52], the intensity is mostly not directly measurable on a full power laser shot. In most setups the spatial and temporal shape of a pulse is measured independently and pre-characterized. The energy is also measured in an independent measurement but can sometimes be estimated on shot, by monitoring the leakage through a beam-line mirror. The three quantities are then combined to estimated the peak intensity available in an experiment. A special care has to be taken, when comparing experiments with simulations. The pulse length and focus diameter in simulations are often related to the electric field, whereas in the experiment they are normally referred to the intensity distribution. Therefore beam parameters in the experiment relate to the electric field parameters as $\sigma_E = \sigma_{\mathrm{FWHM}}/\sqrt{8\ln(2)}$.
In the next section the dimensionless laser amplitude a_0 will be introduced, which marks a threshold intensity for relativistic electron motion. The laser intensity can also be expressed in terms of $a_0 = eE_0/m_e c\omega_L$ as,

$$I \approxeq \frac{1.37 \cdot 10^{18}\mathrm{W/cm^2}}{\lambda^2[\mu\mathrm{m}]} a_0^2 = I_1 \cdot a_0^2. \tag{2.15}$$

[2] For the pulse length this gives $\tau_L = \sqrt{4\ln(2)\sigma_{It}^2}$, and for the spatial dimensions, $d_x = \sqrt{4\ln(2)\sigma_{Ix}^2}$, and $d_y = \sqrt{4\ln(2)\sigma_{Iy}^2}$

I_1 marks the mentioned threshold intensity. Using a_0 with Eq. (2.10) and Eq. (2.11), we can estimate the field amplitudes of the electric and magnetic fields to

$$E_0 \approxeq \sqrt{\frac{2I_1}{c\epsilon_0}} a_0 = 3.2 \cdot \frac{a_0}{\lambda^2[\mu\mathrm{m}]} \times 10^{12}\,\mathrm{V/m} \tag{2.16}$$

$$B_0 \approxeq 1.07 \cdot \frac{a_0}{\lambda^2[\mu\mathrm{m}]} \times 10^{4}\,\mathrm{T} \tag{2.17}$$

2.3. Single electron in an intense light fields

Neglecting photon emission from the accelerated electron, the equation of motion of a charged particle is given by the Lorentz force,

$$\vec{F} = \frac{d\vec{p}}{dt} = -e \cdot \left(\vec{E} + \vec{v} \times \vec{B}\right) = \vec{F}_\perp + \vec{F}_\parallel, \tag{2.18}$$

where $\vec{p} = \gamma m_e \vec{v}$ is the relativistic electron momentum, with the Lorentz factor $\gamma = (1 - v^2/c^2)^{-1/2}$. The Lorentz force has two components, where the first term yields an acceleration perpendicular to the laser propagation direction, where (neglecting relativistc effects),

$$v_\perp = \frac{e}{m_e \omega_L} \vec{E}(t) = \frac{eE_0}{m_e \omega_L} \cdot \sin(\omega_L t) \tag{2.19}$$

$$v_{\perp(\max)} = \frac{eE_0}{m_e \omega_L}. \tag{2.20}$$

From Eq. (2.10) follows, that the force along the laser propagation direction is $\vec{F}_\parallel = -ev_\perp E_0/c$. Thus for velocities much smaller than the speed of light, this term is negligible as compared to the acceleration along the magnetic field. The relation $\vec{F}_\parallel / \vec{F}_\perp$ can define the dimensionless laser amplitude

$$a_0 \equiv \frac{eE_0}{m_e c \omega_L} = \sqrt{\frac{I}{I_1}}. \tag{2.21}$$

For $a_0 \gtrsim 1$ relativistic effects become relevant. Another way to view this quantity can be by comparing the kinetic energy gain per cycle to the electrons rest mass. As soon as these parameters become comparable, we speak of a relativistic laser

plasma interaction. Using Eq. (2.21), we can also express the Lorentz factor in terms of a_0 in the first order approximation, [53]

$$\gamma = \sqrt{1 + a_0^2/2} \tag{2.22}$$

Present day laser systems reach focused intensities up to $10^{22}\,\mathrm{W/cm^2}$, [11, 54] using a Titanium Sapphire (Ti:Sa) laser, with $\lambda = 0.8\,\mu\mathrm{m}$, which is far beyond the relativistic intensity threshold I_1 for electrons. In contrast, the intensities and fields are not high enough to reach the relativistic regime for protons. In order to estimate that threshold, the electron mass in Eq. (2.21) has to be replaced by the proton mass, which yields a $I_{1p} \approx 5 \times 10^{24}\,\mathrm{W/cm^2} \times 1/\lambda^2[\mu\mathrm{m}]$. Consequently protons can not directly be accelerated by the laser fields, but ions rather couple to the laser field via slowly varying dipole fields induced by charge separation field due to the higher mobility of the electrons.
As the particle mass is not a constant anymore in the relativistic regime, we have to modify Eq. (2.2), Eq. (2.3) and Eq. (2.4) to

$$\omega_p = \sqrt{\frac{n_e e^2}{\epsilon_0 \gamma m_e}} \tag{2.23}$$

$$n_c = \frac{\gamma m_e \epsilon_0 \omega_L^2}{e^2} \tag{2.24}$$

The intensity dependency of the critical density and refractive index leads to interesting phenomena like relativistic induced transparency or relativistic self-focusing of a pulse in an undercritical plasma, which can be used to enhance ion acceleration performance, e.g. [55].
A real laser pulse is not a plane electromagnetic wave and the equation of motion of an electron is then not analytically solvable. But the pulse can be split into a slowly varying envelope in space and time and a fast oscillating component. Slowly varying in this context means that the temporal envelope varies much slower than $2\pi/\omega_L$, i.e the pulse consists of multiple cylces and also the spatial envelope varies much slower than λ, i.e. the pulse is not tightly focused. Under the additional assumption that the electric field over one laser cycle averages to zero, while the envelope function has a non zero average, the ponderomotive

force is the slowly varying, time averaged force term, [49, p. 15] and is given by

$$\vec{F} = -\frac{e^2}{2m_e\omega_L^2}\vec{\nabla}\langle\vec{E}(t)^2\rangle = -\vec{\nabla}\Phi \tag{2.25}$$

$$\Phi = \frac{e^2}{2m_e\omega_L^2}\langle\vec{E}(t)^2\rangle = \frac{m_e c^2}{4}a_0^2. \tag{2.26}$$

As Eq. (2.26) does not obey the Poisson equation, $\nabla^2\Phi = 0$, it is often referred to a pseudopotential, which mathematically can be treated like a regular potential. An interesting consequence of the ponderomotive potential and its resulting force, $\vec{F} = -\vec{\nabla}\Phi$, is that electrons (or also ions) will be expelled from the area, where the electric field is highest towards areas of a weaker field. This can be understood by considering an electron at rest on the central axis of an incoming beam. In the first half-cycle the electron is accelerated transversely. In a pulse with finite transverse extent, the electric field at the turning point, driving the test electron back to its original position, is weaker than the on-axis field. The electron is left with a net offset after one cycle.

2.4. Laser energy absorption

The dominant absorption mechanisms are widely dependent on the intensity of the laser pulse. In the low, sub-relativistic intensity regime, $I < 10^{16}\,\mathrm{W/cm^2}$, [56, p. 20] the absorption is dominated by collision processes between ions and electrons, which is also known as inverse Bremsstrahlung, [49, p. 66]. This absorption is dominating prior to the main pulse for, e.g., prepulses or high ASE levels and can lead to unintended plasma pre-expansion due to the limited temporal contrast of current laser systems, see Section 3.2.2. In the scope of this thesis we intentionally introduced a pre-pulse to yield a controlled plasma pre-expansion.
In the rising edge of the laser pulse, the intensity quickly surpasses the relativistic intensity threshold and non-collisional absorption becomes the dominating process, as the reduced Coulomb cross section decreases with the square of the electron energy and suppresses collisional heating. The dominant processes are Resonant absorption, Brunel heating, and $\vec{j}\times\vec{B}$ heating. For the discussion of these absorption processes, we assume that the heating and ionization process happens

fast, such that hydrodynamic expansion does not play a significant role. Further we are only considering a plasma with near or overcritical density, which means that the laser can only penetrate up to the skin depth of thickness δ_s, Eq. (2.5). The brief description follows [49, 57].

2.4.1. Resonant Absorption

Resonant absorption occurs in an inhomogeneous plasma, where the density is nearly uniform over a oscillation period of the laser. It is most efficient at the critical density surface, where $\omega_L = \omega_p$. Here a plasma wave, which is a charge density perturbation, can be excited, coupling laser energy into the plasma. In order to drive the perturbation, a prerequisite is that the driving electric field must have a component reaching into the bulk of the target. This requires p-polarization as well as an oblique angle of incidence.

2.4.2. Brunel Heating

In contrast to resonant absorption Brunel Heating requires a strong density gradient, i.e. a sharp vacuum plasma boundary [58]. For a strong density fluctuation a local plasma frequency is not defined and wave propagation is not possible. As in the case of resonant absorption, an electric field component reaching into the target is necessary, which requires a p-polarized laser with oblique incidence. Electrons at the plasma surface are dragged out of the plasma into vacuum by the first half cycle of the laser and then accelerated towards the plasma in the second half-cycle of the laser. After re-entering the plasma they escape the laser field into deeper plasma layers due to their inertia, and where the laser can not penetrate deeper as the scale length into the over critical plasma. Electrons entering the bulk can not be reached anymore and hence extract energy from the laser.

2.4.3. $\vec{j} \times \vec{B}$ Heating

In the high relativistic regime the mechanism called $\vec{j} \times \vec{B}$ heating becomes relevant. Here the driving force is not the electric field, but the longitudinal $\vec{j} \times \vec{B}$ term (collective $\vec{v} \times \vec{B}$). As this process does not require a component of the electric field

to reach into the bulk of the target, we do not require an oblique incidence or p-polarization. Assuming an elliptically polarized laser, with ellipticity $0 < \epsilon < 1$ ($\epsilon = 0$ is linear polarized, $\epsilon = 1$ is circular polarized) yields the driving fore on the electrons, by considering only the $-e\vec{v} \times \vec{B}$ term, which is the ponderomotive force term in Eq. (3.10)

$$F_x = F_0 \cdot \mathrm{e}^{-2x/\delta_s} \cdot (1 + \frac{1-\epsilon^2}{1+\epsilon^2} \cos(2\omega_L t)), \tag{2.27}$$

where $F_0 = (2m_e c^2)/(\omega_L/\omega_p)a_0^2$. The cycle average over Eq. (2.27) yields the polarization independent ponderomotive force. This yields two interesting findings, compared to the previous heating mechanisms. First the driving force is oscillating with $2\omega_L$ and scales with a_0^2 rather than a_0. Finally one sees a fundamental difference between linear and circular polarized pulses. In the case of circular polarization the fast oscillating term in Eq. (2.27) vanishes. The generation of hot, fast electrons is therefore suppressed in the case of circular polarized pulses. Thus linear polarization is favorable for processes that rely on a high electron temperature (e.g. TNSA) and circular polarization is favorable for schemes that favor a collective push of the target. This process was shown via a 2D simulations by [59]. If one thinks of an electron feeling the ponderomotive potential, the energy gain of an average or representative electron in this potential can be associated with an effective temperature, that scales as [53]

$$k_b T_e \approx (\sqrt{1+a_0^2} - 1) m_e c^2 \tag{2.28}$$

2.5. Ion acceleration schemes

As mentioned, electrons mediate the field for ion acceleration, that is they transfer energy to the ions via slowly varying rectified fields that arise due to charge separation. The section here should give a short overview on the most prominent and most widely investigated acceleration mechanism, the TNSA. From this point we focus the on Hole Boring (HB) regime, which is of particular interest for this thesis.

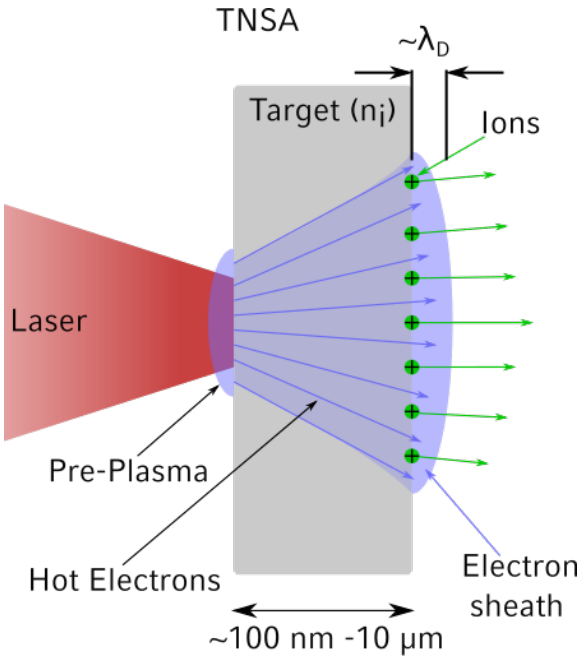

Fig. 2.1. *| Schematics for TNSA acceleration from a foil.*

2.5.1. Target Normal Sheath Acceleration (TNSA)

TNSA is among the most studied acceleration mechanisms, after ions with multi-MeV energies have been demonstrated in 2000, [15]. In the standard case of TNSA an intense laser pulse, exceeding $10^{18}\,\mathrm{W/cm^2}$ interacts with a solid thin foil. The interaction with a preformed plasma on the laser facing side is a source of hot electrons, with a temperature depending on the laser intensity, which is typically associated with the temperature gained by the ponderomotive potential Eq. (2.28). The hot electron cloud penetrates the target bulk and escapes into vacuum on the unperturbed, non irradiated side. A small fraction of the electrons circulates back and forth, repeatedly reflected at the plasma-vacuum boundary and forms a sheath field over a (hot electron) Debye length. The induced electric fields on the rear side are of the order of terravolts per meter and quickly ionize atoms and accelerate the resulting ions normal to the initially unperturbed target surface. The emission of the ions thus depends on the local structure of the surface. This scheme is illustrated in Fig. 2.1 (a) [60]. For sufficiently thick targets (> 100 nm) the heating zone of the laser and the acceleration zone are spatially separated.

The maximum field on the target rear surface is estimated as

$$E_{sheath} = \sqrt{\frac{2T_e^2}{e_N e^2 \lambda_D^2}}, \tag{2.29}$$

where e_N is the Euler number. In most models the acceleration time is a free parameter, where it was found that $t_{acc} \approx 1.3\tau_0$, where τ_0 is the laser pulse length, as a crude and empirical approximation [14]. Analytical models for the TNSA mechanism have been e.g. proposed by [61] or [62], giving analytical estimates for the maximum proton energy and spectral shape.
While the conversion efficiency and the maximum proton energy increase with thinner foils, the lower limit to the foil thickness is actually dictated by the laser contrast [63]. If a pre-pulse alters the target rear side, the sharp ion density gradient washes out and the maximum sheath field can not be reached. On the other hand if the target thickness becomes comparable to the relativistically corrected skin depth of the laser pulse ($\approx \gamma \cdot 10\,\text{nm}$, for typical solid targets), other processes can become relevant, such as contributions from radiation pressure acceleration (RPA) [64, 65], or the breakout-after-burner [17, 66].
As the lateral extent of the electron sheath impacts the ion acceleration, it has also been found that confining electrons laterally by reducing the lateral dimension enhances ion particle energies [67]. A limit of reducing all dimensions is either a flying foil or a spherical target.

2.5.2. Coulomb Explosion

One extreme case of spherical "expansion" is given by expelling the sphere of all electrons. Having a uniformly charged sphere of radius r_T of a single ion species, the energy distribution of the Coulomb explosion can be calcualted analytically. The shere of target density n_0 has the charge $Q = 4/3\pi r_T^3 n_0 q$, where $q = Z \cdot e$ is the charge the particle species. The electric field can be derived applying Gauß's law. For $r > r_T$, the electric field is given by the field of a point charge, whereas for $r < r_T$ only the charge Q_{encl} enclosed in a sphere with radius r contributes to

the electric field,

$$\mathcal{E}(r) = \frac{Q_{encl}}{4\pi\epsilon_0}\frac{1}{r^2} \tag{2.30}$$

The charge within the sphere of uniform charge distribution is given by

$$Q_{encl}(r) = \int dV n(r) q = \frac{Q}{r_T^3} \cdot r^3, \tag{2.31}$$

considering a step like initial distribution of $n(r)$, with $n(r) = n_0$ for $r < r_T$ and $n(r) = 0$ for $r > r_T$. Applying this on Eq. (2.30) yields the electric field,

$$\mathcal{E}(r) = \begin{cases} \frac{Q}{4\pi\epsilon_0}\frac{r}{r_T^3} = \frac{n_0 q}{3\epsilon_0} r & r < r_T \\ \frac{Q}{4\pi\epsilon_0}\frac{1}{r^2} = \frac{n_0 q r_T^3}{3\epsilon_0}\frac{1}{r^2} & r > r_T \end{cases} \tag{2.32}$$

The energy gained by a particle in the sphere, starting at a specific position r, is then given by the potential difference between infinity and the particles starting position, yielding

$$E(r) = q(\phi(\infty) - \phi(r)) = \frac{q^2 n_0}{3\epsilon_0} r^2 \tag{2.33}$$

Eq. (2.33) is only valid in the limit, where particles do not overtake each other. As no particles are located outside the sphere, one can see from Eq. (2.33) that the maximum energy is achieved for particles initially located at the boundary, $r = r_T$,

$$E_C = \frac{n_0 q^2}{3\epsilon_0} r_T^2 \tag{2.34}$$

Take into the infinitesimal particle number in a shell of the sphere, $dN = 4\pi n r^2 dr$, and using $dE/dr = {}^{q^2 n_0}/_{3\epsilon_0} r$ the particle number spectrum can be found as

$$\frac{dN}{dE} = \frac{dN}{dr} \cdot \frac{dr}{dE} = \frac{6\sqrt{3}\pi\epsilon_0^{3/2}}{q^3\sqrt{n_0}} \cdot \sqrt{E} \tag{2.35}$$

This yields the characteristic $\sqrt{E}$ scaling of the Coulomb explosion up to E_C. At this point there is a sharp boundary in the spectrum given by the initially sharp

boundary of the sphere.

A few simple considerations can be drawn from Eq. (2.34). In an experiment the

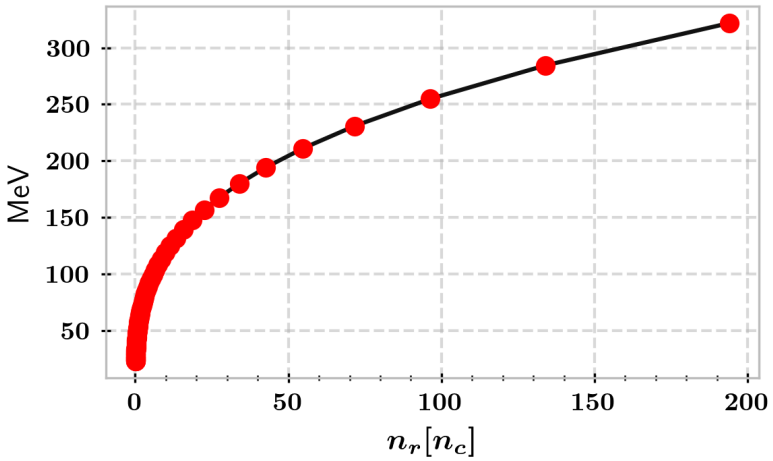

Fig. 2.2. *| Scaling of the maximum of a* 1 µm *proton sphere energy by Coulomb explosion, while keeping the total charge constant.*

density can be varied by means of expansion of the sphere before the peak intensity is reached. This mode leaves the total charge in the sphere unchanged, but increases the target radius. Accordingly, assuming a homogeneous density distribution (and hence steep plasma-vacuum boundary), $n_r = n_0 \cdot r_0^3/r^3$. Applying this relation to Eq. (2.34), one finds

$$E_c(n_r) = \frac{n_r q^2}{3\epsilon_0}\left(\frac{n_0}{n_r}\right)^{2/3} \cdot r_0^2 = \frac{n_0^{2/3} q^2 r_0^2}{3\epsilon_0} \cdot n_r^{1/3}. \tag{2.36}$$

Thus expanding the target, and decreasing the average density n_r results in a lower achievable maximum energy. Fig. 2.2 shows the maximum attainable particle energy from a homogeneous sphere. We can see that the maximum energy decreases, due to Coulomb explosion being highest for smallest spheres with highest density.

The considerations above assume that the laser energy is sufficient to remove all electrons from the sphere, which typically is not the case for the laser system used in this thesis. In a scenario of solid spheres, the target size and shape can be modified by pre-expansion. In general, the density profile then will be radially decaying. As soon as a non homogeneous radial distribution is applied (e.g. radial

Gaussian), the strongest accelerating field lies within the target, and particles from deeper in the volume see a stronger acceleration field as particles on the surface. Therefore ions can over take each other and the dynamics can hardly be solved analytically. In a multi species target a pronounced proton yield at specific kinetic energies can result (e.g. [68]).

2.5.3. Radiation Pressure acceleration - light sail (RPA)

Radiation pressure acceleration in the context of relativistically intense laser-plasma ion acceleration was first proposed theoretically in 2004 by Esirkepov et. al. [64]. The proposal required a laser with a peak power of $1.37 \times 10^{23}\,\mathrm{W/cm^2}$ and a sharp (non-Gaussian) laser front. Both conditions are hard to achieve experimentally. For efficient Radiation Pressure Acceleration (RPA) electron heating, i.e. random electron motion, should be suppressed. Circularly polarized lasers avoid the 2ω beating of the ponderomotive force, and hence help in relaxing the requirements. RPA effects have been observed in experiment [65] and theory [69] at lower intensities.
In the first phase, the high intensity laser pulse expels electrons from the target, while the protons react slowly on the force. For a sufficiently large charge separation field, the electric force excerpted by ions balances the ponderomotive push of the laser and then the ions are dragged along. Ideally, the laser gets reflected at the moving electron light sail. As all components of the target are co-moving at the same velocity in the ideal case, electrons and ions could be confined to a narrow energy band.
In an ideal scenario all laser energy can be converted into particle energy [14]. Requiring the push of the laser being balanced by the electric pressure in the target, yields a charge separation field at the order of the maximum laser electric field,

$$a_0 \sim \pi\sigma = \pi\frac{n_e l}{n_c \lambda_0} \tag{2.37}$$

with σ as the areal density and l as the foil thickness [14, 70, 71]. With the balance condition fulfilled, the maximum particle energy $E_{max} \propto I$.
Similar considerations can be made for spherical targets, [72]. The pressure imbalance is caused by the light pressure exerted on the sphere and the electric pres-

sure caused by displacing all electrons out ouf the sphere, $\epsilon_0 \mathcal{E}^2 \leq 2I/c$, where the maximum electric field, $\mathcal{E}$, is given by the Coulomb field on the surface of a fully charged sphere, Eq. (2.30). Despite some pre-factors this yields a similar condition

$$a_0 \sim \frac{2\pi}{3} \frac{n_e r_T}{n_c \lambda_0}, \tag{2.38}$$

for the normalized laser amplitude as for foils, where r_T now is the target radius. Putting the condition in simple words: If the target is too thin, the ponderomotive force is much stronger than the Coulomb force excerpted by the ions. The electrons are extracted and the remaining ion cloud explodes, see Section 2.5.2. If the target is too thick, the foil is too "heavy" for an efficient charge separation field or the laser can not act coherently on all electrons.
For extended foil targets, an additional requirement is that the laser focus has to be sufficiently large, to ensure that transverse forces remain insignificant. This obstacle can be overcome, by matching an isolated target to the focus diameter, which has for example been studied by [67], who theoretically investigated a sub-focus sized, foil like pellet. Additionally one can think of exploiting the balance condition Eq. (2.37). The easiest accessible parameter to reach a RPA-like regime experimentally is the target thickness l. The areal density, however, could be changed only in a very limited way, by e.g. foam targets, which are targets with reduced density as compared to solid density foils. For spherical targets, we can exploit a pre-expansion from a solid density sphere, to dynamically change the interaction density. For example, consider a planar foil, which expands into one dominant direction before the actual interaction with the laser. The expansion along the laser axis does not change Eq. (2.37), because $n_e * l \approx$ const. for all expansion times. A similar condition can be derived for a spherical target, but when the sphere expands, $n_e * r_T \propto 1/r_T^2$ enables at least one additional degree of freedom in the target parameter space.

2.5.4. Radiation Pressure acceleration - Hole Boring (HB)

For relatively thick targets ($\gg$ skin depth), a light sail mode of the radiation pressure process can not be achieved. The target, however, will deform due to the laser pressure, and the resulting dynamics is described as Hole Boring (HB) by

[53]. HB assumes a quasi-stationary laser piston model [73]. In a simple picture the laser pressure piles up electrons and a sharp electron density spike appears, from which the laser is reflected. A charge separation field between the electrons and ions will be initiated, which can accelerate the ions. Assuming a uniform plasma, and a constant intensity I, a quasi constant HB- velocity v_{HB} can be considered. In the co-moving frame of the reflection front, the laser pressure on the laser-plasma surface can be estimated as [74, 75]

$$P_L = \alpha \frac{2I}{c} \frac{1 - v_{HB}/c}{1 + v_{HB}/c}, \tag{2.39}$$

where $\alpha = 1$ for a circularly polarized lasers and $\alpha = 1/2$ for a linearly polarized laser. Here $2I$ represents perfect reflection and the fraction represents the Doppler shift of reflected radiation. In the boosted frame, ions at rest are approaching the laser-plasma surface at a speed of $-v_{HB}$ and are finally reflected form the front. Assuming elastic reflection, the laser pressure is balanced by the pressure of the ions,

$$P_i = 2\gamma_b^2 v_{HB}^2 \sum_i m_i n_i, \tag{2.40}$$

where $\gamma = (1 - v_{HB}^2/c^2)^{-1/2}$ and m_i and n_i are the masses and density of the ion species.
Using conservation of momentum ($P_i = P_L$), one obtains

$$(B-1)\frac{v_{HB}}{c} - 2B\frac{v_{HB}}{c} + B = 0, \tag{2.41}$$

where

$$B = \alpha \frac{I}{\rho c^3} = \alpha \frac{a_0^2 m_e n_c}{\sum_i m_i n_i} \tag{2.42}$$

is the dimensionless piston parameter, where ρ is the target density. Eq. (2.41) can be rearranged to find the hole boring velocity as

$$\frac{v_{HB}}{c} = \frac{\sqrt{B}}{1 + \sqrt{B}} \tag{2.43}$$

Eq. (2.43) and Eq. (2.42) show that v_{HB} increases with decreasing plasma density. On the other hand, for a reflection front to be initiated, the plasma has to stay relativistic overcritical, hence $n_e > (1 + \alpha a_0^2)^{1/2} n_c$.

Chapter 3

Methods

3.1. A Paul Trap for isolated targets

The Paul trap used in for these experiments has been the eager result of many people and was the basis for two previous PhD theses, [68, 72]. In the course of this work, the system has been upgraded to fulfill the conditions for laser systems with higher repetition rates, which includes the automation of the target trapping and positioning process. This section gives a brief introduction into the fundamental parameters of a linear Paul trap, the state of the system as in [41] and describes the improvements made to the setup. The theoretical description is mainly based on [76, 77].

3.1.1. Design

A three dimensional confinement of a charged particle requires a potential minimum superimposed upon each other along all three spatial dimensions. However according to Earnshaw's theorem [78], this can not be achieved by electrostatic fields. Instead a time-dependent electric field generates a ponderomotive pseudo potential that enables levitation. A realization of a system of that kind is a linear Paul trap, which is driven by time-dependent harmonic oscillations,

$$\Phi(x, y, t) = \frac{V \cdot \cos(\Omega t)}{r_0^2}(x^2 - y^2), \tag{3.1}$$

where V is the AC voltage amplitude applied to the trap electrodes, Ω is the

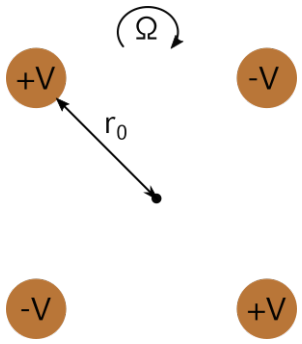

Fig. 3.1. *| Schematic drawing of the trap geometry, indicating the quadrupole electrodes and the trap center.*

angular drive frequency and r_0 is the distance between the trap center and to electrode's surface, see Fig. 3.1. Potentials of these form are ideally generated by hyperbolic formed electrodes, that follow the equipotential lines and extend infinitely along the third dimension. Depending on the voltage amplitude and the drive frequency the resulting net force can either lead to confinement in the trap center or to convergence outwards, leading to particle loss. The stability area of a particle with mass M and charge Q can be found by solving the equations of motion, with $M\frac{d^2\vec{x}}{dt^2} = -Q\vec{\nabla}\Phi(\vec{s})$, which results in a set of three differential equations in the form of the homogeneous Matthieu equations,

$$\frac{d^2x}{dt^2} + 2q\cos(2\tau)\,x = 0 \tag{3.2}$$

$$\frac{d^2y}{dt^2} - 2q\cos(2\tau)\,y = 0 \tag{3.3}$$

$$\frac{d^2z}{dt^2} = 0, \tag{3.4}$$

with $\tau = \Omega/2\,t$ and the dimensionless parameter

$$q = 4\frac{Q}{M}\frac{V}{r_0^2\Omega^2}. \tag{3.5}$$

Stable solutions to the Matthieu equations remain limited and constitute solutions that allow trapping, while unstable solutions are growing in time, leading to particle loss after short time, [76]. The classification between stable and unstable solutions is based on the value of q, where $0 < q < 0.908$ constitutes stable solutions.

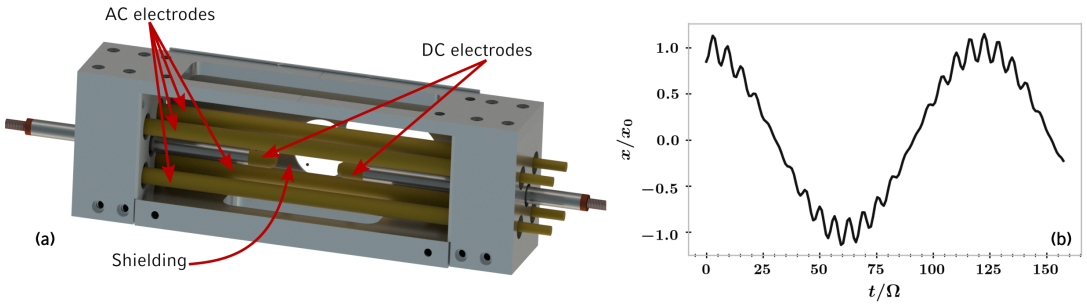

Fig. 3.2. *| (a) CAD Model of the Paul trap. Additional microscope shielding in the background. (b) Trajectory of a test particle, with* $\Omega = 2\pi \cdot 1500\,Hz$, $q = 0.3$ *and an initial position* $x = x_0$, *and an initial velocity of* $dx/dt = 0$. *It shows the superposition of a fast oscillation with the trap frequency and the slow motion with the secular frequency* ω_{sec}

An example of a stable solution is given in Fig. 3.2 (b). In the limit of the adiabatic approximation, i.e. the particle does not exchange energy with the fast oscillating background field, the particle motion is the superposition of two oscillations. The slow motion is known as the secular or macromotion, with frequency

$$\omega_{sec} = \frac{Q}{M}\frac{\sqrt{2}V}{\Omega r_0^2}. \tag{3.6}$$

The fast motion is known as the micromotion with the driving frequency Ω. In the adiabatic approximation the macromotion can be separated by time averaging over the fast oscillating component, and be treated as a harmonic oscillator with frequency ω_{sec} and a potential depth

$$U(x) = \frac{1}{4}qV\frac{r^2}{r_0^2}, \tag{3.7}$$

where $r = \sqrt{x^2 + y^2}$ is the distance from the trap center along the direction of the hyperbolic electrodes. It is noteworthy that this potential does not fulfill the Laplace equation and is referred to as a pseudo-potential, but it is used in the environment of particle traps to estimate the effective forces acting on the particle.

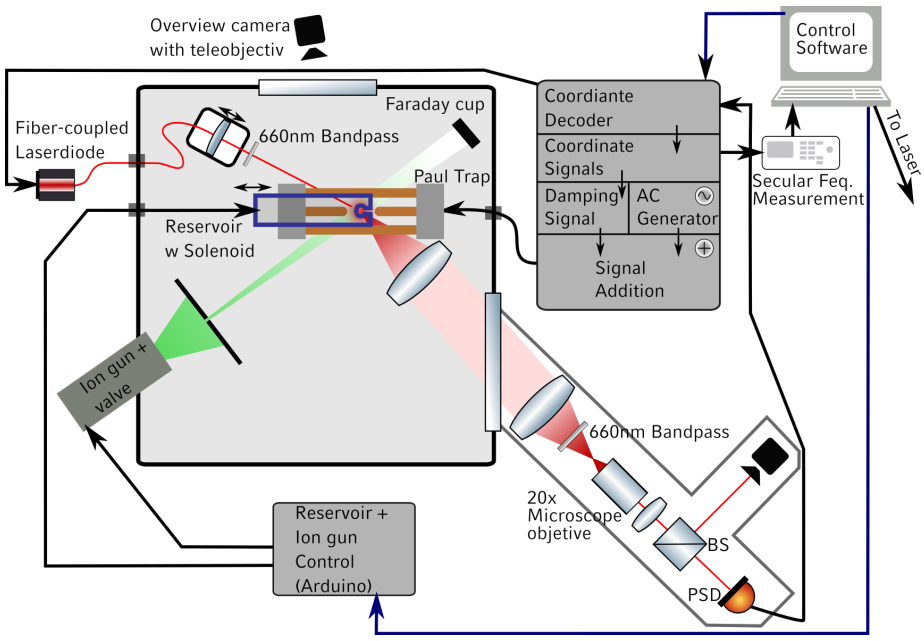

Fig. 3.3. *| Schematic drawing of the most important Paul trap components. Specific arrangement of the components is subject to change depending on the specific requirements at a high power laser system.*

3.1.2. Experimental Realization, Improvements and trapping sequence

The starting point of the experimental realization is described in [41]. The system is specifically designed to facilitate the needs for experiments at a high power laser. This specifically requires a trap operation and particle positioning at pressures below 10^{-6} mbar. The Paul trap is shown in Fig. 3.2 (a). It consists of four cylindrical rods as AC electrodes, placed 10 mm apart, with a rod diameter of 5 mm, yielding an $r_0 = 8.1$ mm. With these specifications we deviate from the ideal hyperbolic shape of the electrodes as well as from the ideal configuration for round rods [79], introducing higher potential terms, where the next contributing order is the 12-pole, which also becomes to zero in the trap center. It has been shown that this can introduce unstable regions even in the region of stable trapping [80]. On the other hand introducing buffer gas can increase the area of stability. We circumvent this issue by tuning the trap frequency and trap voltage, when we experience an instability and are moving the parameters away from these resonances. The choice of this geometry has the benefit to provide sufficient optical

access to the trap center. The rods are 100 mm long and housed in a precision manufactured glass ceramic. The endcaps used to be made of a 3 mm thick copper slab on the central trap axis and are placed 10 mm to 20 mm apart from each other. With copper being a soft material and the slabs freely hanging for length of multiple centimeters, the endcaps have bent over time, such that the endcap tips did not align perfectly on the central quadruple axis. The misalignment yielded that the potential minima for the three axis did not fall to the same point in space, and accurate positioning decreased. We replaced the endcaps by more rigid stainless steel pipes with a gold coated copper tip.
Each electrode, four AC rods and two DC rods, are connected to their own voltage supply. The AC supplies feature frequencies $\Omega/2\pi$ up to 5 kHz at trap voltages V up to 3 kV. The DC endcap supplies deliver voltages up to 400 V. All electrodes are gold coated to prohibit degrading of electrical properties due to oxidation.
A reservoir of particles is placed above the trap center, which is filled with a few milligram of the target material. The targets are commercially available monodisperse spherical particles provided by Microparticles GmbH [81]. The reservoir has been motorized to enable positioning above the trap center and moving the reservoir out into a safe position after particle trapping, enabling access to the view port from the top. The reservoir follows the working principle of a salt shaker hit by a soil gun. Particles are released through mechanical vibrations of a solenoid, with an iron core. The solenoid is supplied with a 24 V pulse, that is up to 50 ms long and pulls back the iron core. Upon release, the core hits the reservoir container, and particles are falling into the trap through a 500 µm hole. The hit strength is adapted by changing the solenoid's pulse length. For pulse length $>$ 50 ms the core is fully pulled into the solenoid, and triggers a double hit, which is sometimes useful to open a clogged salt shaker.
The particles are charged by an ion beam, crossing the free fall path of the particles. Charges are accumulating on the particle's surface and the trap potential that the particle feels, increases. The iongun is built by Tectra GmbH, [82], delivering ions with up to 5 keV. We typically use room air as a source for the ion beam. A single lens can be installed in front of the ion gun, to increase the ion beam flux density in the trap center. The single lens can be supplied with voltages up to 5 kV and is designed to allow re-collimation of the ion beam rather than guaranteeing good imaging properties. The ion gun is supplied with a motorized

valve that allows gas flow control. For operating the iongun, the flow through the iongun is adjusted to maximize the ion current at otherwise constant ion gun settings. The typical operating pressure varies with the size of the vacuum chamber and the connected pumping power. During the operation of the iongun, the background pressure typically increases to $10^{-5} - 10^{-4}$ mbar. The ion current is constantly monitored by a Faraday cup with an active area of 2 mm . The ion gun and reservoir are operated through the same Arduino Uno, [83] controller, which runs at a clock speed of 16 MHz. Before particle release, the iongun runs for 5-10 s until the ion current stabilizes and is switched off a predefined time after activation of the solenoid. The capacitors in iongun's power supply limit the switch time of the ion current to $\sim$ 0.5 s. The minimum charging time should exceed 1 s and should be controlled with a maximum precision of 0.5 s. After trapping the chamber pressure is increased to 10^{-3} mbar to reduce the particle amplitude by buffer gas cooling. Closing the valve restores the initial background pressure within a few 10 s. With a proper choice of trap voltage, trap frequency, charging time and ion current, trapping of a single particle can be achieved most of the time. In the cases, where more than one particle is trapped, either reducing the endcap voltage, or adjusting the trap parameters closer to the unstable region, removes additional particles by Coulomb repulsion. Levitation of a single particle can be confirmed via the overview camera and the camera in the optical damping arm, see Fig. 3.3. In a final step the endcap voltages are increased to ensure sufficient confinement along the z axis and the trap parameters are modified to move away from potential resonances that would not allow reliable particle cooling and positioning.

The particle is illuminated with a 660 nm fiber coupled laser diode, with a maximum output power of 30 mW. The illumination wavelength was chosen to be off-harmonic to the typical wavelength of high-power laser systems, which allows to filter the stray light from the full-power shot. On the vacuum side a 50 mm lens loosely focuses the laser to a focal spot of 1 mm FWHM in the trap center. The lens is positioned on a motorized stage, and sent over a tip-tilt motorized mirror to in-situ align the focal spot to the particle. This maximizes the stray light from the particle. Stray light is collected by two 3″, 150 mm focal length lens creating a 1:1 image outside vacuum, that is then imaged via a 20x microscope and a beam splitter onto a camera, monitoring the particle until shortly before the shot, and

the position-sensing diode (PSD). The PSD tracks the particle's center of mass motion, providing a phase shifted feedback signal to damp the particle motion, see Fig. 3.3.
All devices were integrated in a python based software suite, that also has a connection to Tango Controls [84] for inter-device communication with cameras, motorized stages and, e.g., slow raspberry pi based shutters. For high power lasers systems that are equipped with a Tango-Controls system this also allows communication with the laser system, to e.g. request a shot number. A key feature of the software is the ability to save and load particle parameter sets, and enable scripting of the trapping and particle positioning process. In an ideal scenario trapping and positioning of a particle could be achieved within 90s, repeatedly. Generally the control of all parameters is not good enough to allow proper trapping and positioning under all circumstances. After the automated trapping, manual steps are necessary to confirm levitation of a single particle and to properly damp and position a particle in the laser focus. Positioning in the laser focus is ensured by moving the trap on a *xyz*-stage.

3.1.3. Surface charging of isolates spheres

Controlling particle charging precisely is a key to reproducible levitation of the particles. The time-dependent surface potential of a micro-particle a collimated ion beam, is described by [85],

$$\Phi(t) = \begin{cases} \Phi_\infty + (\Phi_0 - \Phi_\infty) \cdot \mathrm{e}^{-t/\tau} & q\Phi_0 < q\Phi_\infty \\ \Phi_0 & q\Phi_0 \geq q\Phi_\infty, \end{cases} \tag{3.8}$$

where Φ_0 is the surface potential at $t = 0$, Φ_∞=$\lim_{t\to\infty} \Phi(t) = E_0/q$ is the surface potential in the equilibrium state, and

$$\tau = 4\epsilon_0 \frac{E_0}{q} \frac{1}{R\, j\, \tilde{\alpha}} \tag{3.9}$$

is the time constant of the charging, with E_0 as the kinetic energy of the ion beam and $\tilde{\alpha}$ as a coefficient of static friction, which we assume to be 1. Using typical parameters for the ion energy, $E_0 \simeq 3\,\mathrm{keV}$, the current density $j \simeq 5\,\frac{\mathrm{nA}}{\mathrm{mm}^2}$ and a

1 µm sphere, ($R = 0.5\,\mu m$), $\tau \simeq 42\,s$.
The particles are falling into the trap from a height of approx. 5 cm, and are only charged in the time they spend between the two rods while falling through the trap. Using the acceleration in the gravitational field, and the geometry of the trap, the particle spends about 100 ms between the upper and lower electrodes of the Paul-trap. Within this time the charge-to-mass ratio of the particle has to increase to a level that the pseudo potential overcomes gravity and stops the particle's free fall motion. On the other hand the maximum charging time is limited by the stability condition, requiring $q < 0.908$. Thus particle charging is always a trade off between charging fast enough and at the same time too hard to exit the trapping window. Applying a trapping frequency of $\Omega = 2\pi \cdot 1100\,Hz$ and a trapping voltage of $V = 1100\,Hz$ we get a maximum charging time of 1.1 s. From these considerations, we find, that the initial charging has to happen fast, and within the rising edge of the exponential function, resulting in high fluctuation of the particle's charge to mass ratio with charging time jitter. This limits the reproducibility of the charging process.

Even though this calculation neglects the complicated interplay of the ion beam with the trap potentials, the transverse profile of the ion beam and its energy bandwidth, this estimate suggests that especially for heavier particle species a multi-step charging process will probably increase the reproducibility further. The multi-step process would consist of a setting that allows fast initial charging and a consecutive step with reduced ion-energy to reach an equilibrium state with charging times of many seconds, such that a desired charge to mass ratio can be reached.

3.1.4. Operation at High-Power lasers

Operation of the trap at a high power laser system exposes additional challenges on the target system. The first and key challenge is to avoid any changes in DC potential in the vicinity of the Paul trap. Strong potentials in the vicinity of the trap are known to result in a defocusing effect, [86], eventually prohibiting stable positioning. A picture of the installation at the JETi 200 is shown in Fig. 3.4. Most parts are covered in aluminum foil, to avoid the built up of surface charges on dielectric materials, that are in the line of sight of the ion gun beam. To further

limit the ion beam to the trap center, we placed a screen at a distance of approx. 10 cm, with a 10 mm aperture in front of the ion gun.
Besides strong potentials, grounded moving parts close to the trap center alter the electric fields of the AC electrodes, eventually shifting the trap center. We move two components between levitation and the full power shot. The reservoir is placed 30 mm above the trap center, while loading a particle in the trap. Moving it to its out position, moves the particle in the trap by about 3 µm. To avoid complications of aligning the particle, one should make sure to move the reservoir out before the fine alignment to overlap the particle with the laser focus.
The focus diagnostic, which is about 20 mm away from the trap center, can only be moved out after the fine alignment. Moving the microscope has a comparable effect on the particle position as moving the reservoir. Such a movement interferes with a precise positioning in the laser focus. The motion could be suppressed by placing an aluminum screen between the focusing optics and the trap electrodes. The screen has openings to allow optical access for the microscope objective and all other diagnostics. We simulated the effect in SIMION [87] and tested in experiments that the shielding was finally sufficient to suppress the particle motion, when the microscope objective was moved into its parking position.
Additionally, all optical sensitive parts such as the illumination laser and the damping arm have to be protected from the laser light. We secure both components with high quality band pass filters, (FBH660-10, Thorlabs), with 10 nm spectral bandwidth. Especially the illumination laser can not be shuttered as the light pressure exhibited on the sphere was found to be comparable to the force acting on the particle near the potential minimum, thus pushing it into a different equilibrium, compared to when the laser was switched off.

3.1.5. Particle Position Measurement

The most important practical parameter for the operation of the target system in a high-power laser experiment is the damping quality, which is defined by the remaining motion of the particle. This measurement was performed already for 10 µm spheres by [41], we repeated this measurement for a 1 µm sphere here. We measured the residual motion using a 10× magnification at the LION target chamber of the ATLAS 3000 laser, which allowed to resolve the particle motion.

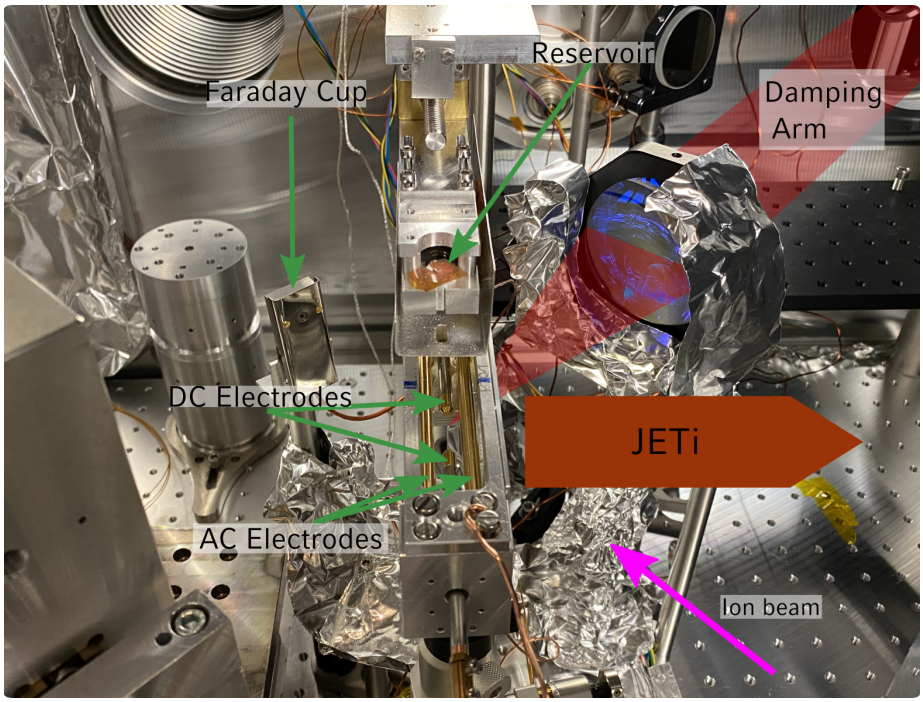

Fig. 3.4. *| Improved Paul trap Setup at JETi 200 Laser. The end-caps are equipped with a thicker, more rigid rod. Above the Paul trap the motorized reservoir is placed. The ion gun is mounted to the vacuum chamber and the ion beam comes from the bottom right.*

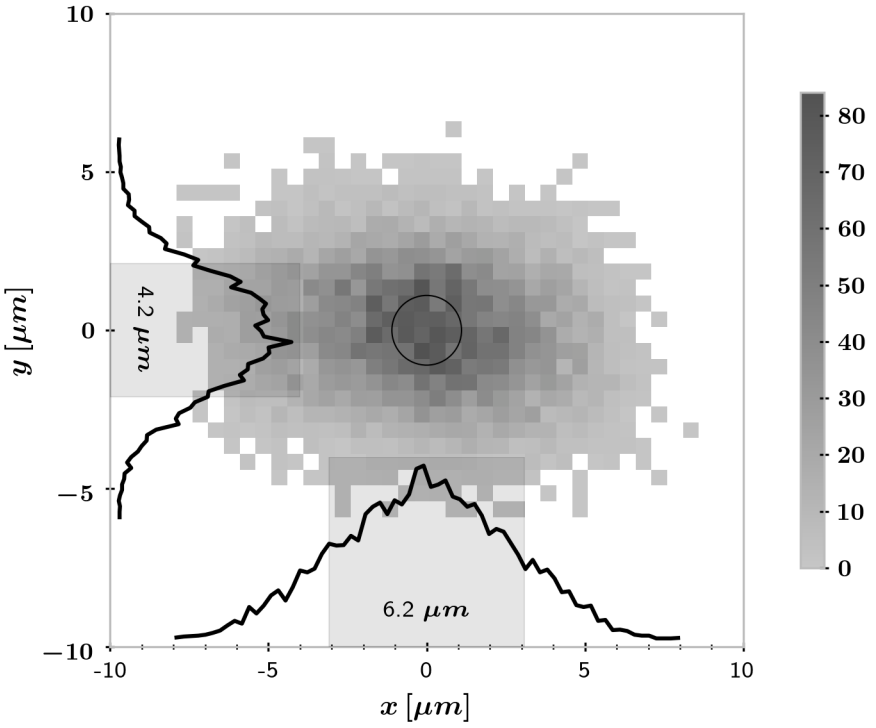

Fig. 3.5. *| Position distribution of a trapped* 1 µm *polystyrene sphere, imaged with* 10× *magnification. The exposure of* 10 µs *for each frame at* 300 *Hz, was chosen, short enough to record a single point. The hit probability with a* 2 µm *laser-focus would be* 10%. *In particular the residual motion is of the same order as the typical laser-pointing jitter, which reduces the hit probability further to* ≈ 5%.

We trapped a 1 µm polystyrene sphere at 1300 V and 1673 Hz, and 42 V DC endcap voltage. We recorded 10001 frames at an exposure time of 10 µs and a frame rate of 300 fps. The exposure time is much shorter than the oscillation period of the macro- and micromotion, thus we expect image blurring by the particle motion to be negligible. From each image we determine the particle's center of mass position and plot the x and y component as a two dimensional histogram in Fig. 3.5. The FWHM of the confined particle is 4.2 µm in the vertical and 6.2 µm in the horizontal direction. The circle refers to a 2 µm FWHM focal spot diameter of a high-power laser pulse, e.g. used in this thesis. From this we can expect a hit probability (defined as hitting the center of the particle with at least half the maximum intensity) of 10%, not taking additional focus jitter into account. If the focus position varies in addition, for example by ±2 µm, the hit probability reduces to

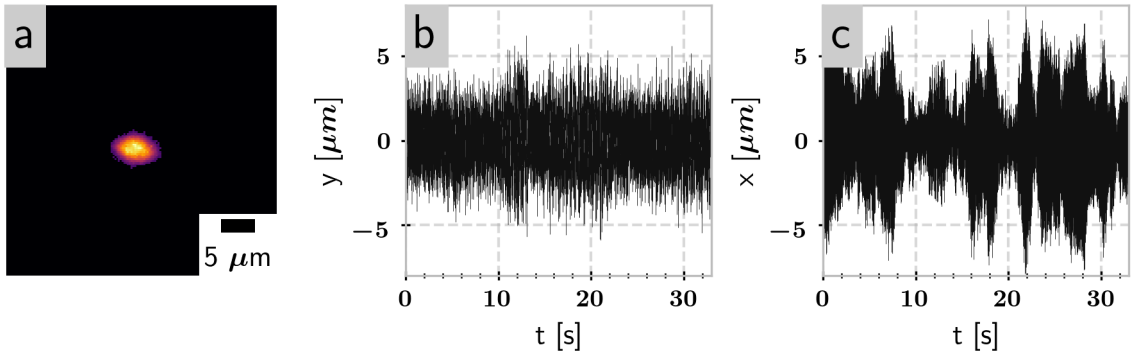

Fig. 3.6. *(a) Image of the particle in the focus microscope for the measurement. Vertical (b) and Horizontal (c) residual motion of the particle. Along the horizontal direction a beating is visible.*

5%.

The center-of-mass tracking for each frame is the most straight forward method, especially as the imaging system is not capable to resolve the 1 µm particle, Fig. 3.6 a. While the image of the particle extends over almost 5 µm, center-of-mass tracking is still capable to resolve a shift in the particle position.

In this measurement it is noticeable that the horizontal motion amplitude is is 50% larger than the vertical amplitude. The time-series of the horizontal motion in Fig. 3.6 c shows a beating of the particle along this axis, while along the vertical axis the amplitude of the residual motion is almost constant. The origin of this beating in this setup is not quite clear, but it could be further reduced by fine tuning the endcap parameters with respect to the trap parameters. The measurement was also done during a working day, where on the one hand the laboratory was frequented by personnel, and on the other hand street traffic was found to influence the stability. We typically perform full power laser shots in evening hours, where daily life is not so much impacting the positioning accuracy.

The multitude of parameters one needs to control, reveals the challenge of operating this target system. Typically we can achieve a similar damping performance along all spatial axes.

The first implementation of the updated Paul trap was at the Zinth's extremely useful superlaser (ZEUS) for plasma pre-expansion studies at moderate intensities of 10^{16} W/cm^2 [88], where the system has shown to enable more than 30 shots on target, within a 6h campaign. This is about the number of shots as for example at

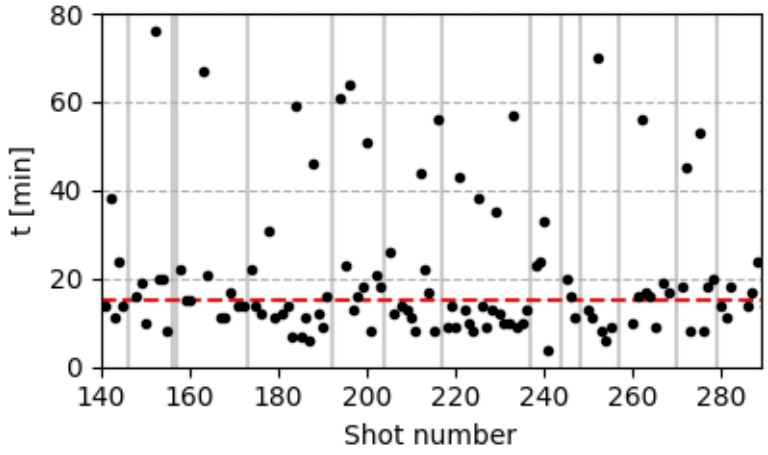

Fig. 3.7. *| Repetion rate of laser shots on successfully trapped spheres at Jeti. The vertical lines indicate different experiment days. The red line indicates the median time between consecutive shots. The median shot frequency was 1 shot every 15 min.*

a 6 weeks campaign at the TPW, [42] or double the shots as at the 6 weeks PHELIX campaign [43]. In the campaign presented in this thesis, at the JETi 200 laser we performed more than 200 shots on spherical target, while the repetition rate was mainly limited by ensuring particle and focus overlap on the minute scale and by detector replacement on the scale of hours. We evaluated the shot frequency at the JETi 200 campaign as the time difference between two shots, correcting for delays due to detector replacement. Within the 4 shots that could be fit on a single detector, we achieved a median shot frequency of 1 shot every 15 minutes, see Fig. 3.7.

3.2. High power lasers

3.2.1. The JETi 200 laser

The JETi 200 laser is a commercial, double CPA, 200 TW system fabricated by Amplitude Laser Group. It uses Ti:Sa as an amplifier material and delivers up to 6.2 J before the compressor, of which about 25% reach the target chamber for the actual experiment, see Section 3.4.2. The amplifier stages consist of typical multi-pass and regenerative amplifiers, that allow maintaining a spectral bandwidth sup-

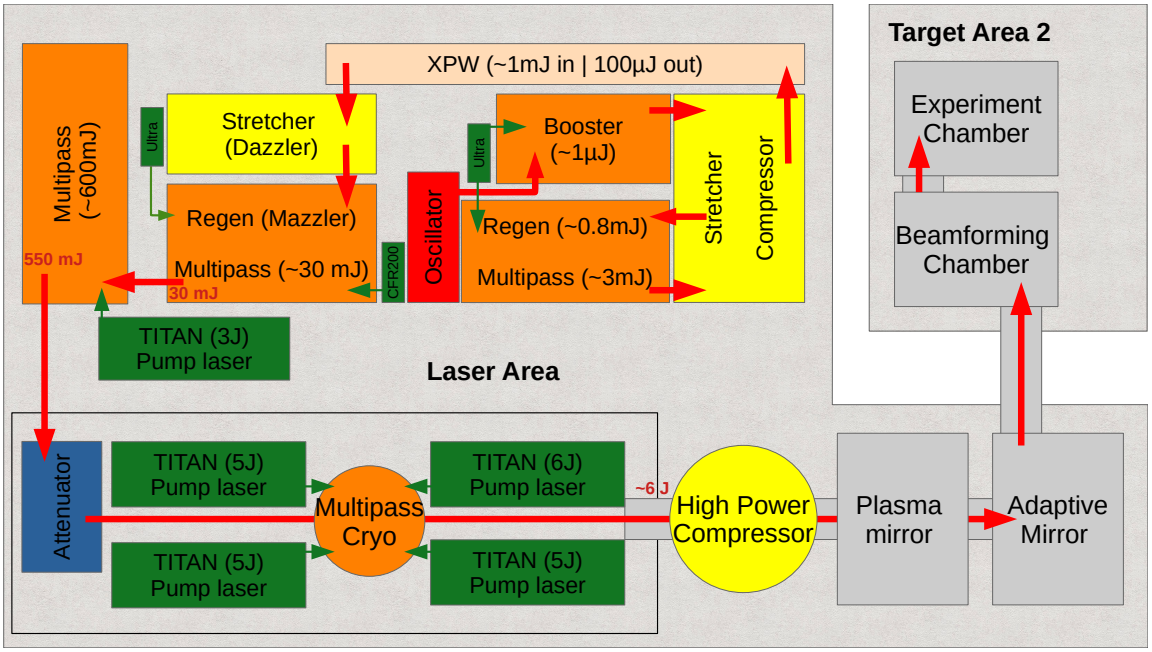

Fig. 3.8. *| Schematic layout of the most important laser components of the JETi 200 laser. Green boxes are pump lasers, orange boxes are amplifiers, yellow boxes show pulse stretchers and compressors. After the main amplifier, the gray boxes indicate a vacuum beamline.*

porting a pulse duration of 20 fs. In our experiment we operated at 32 fs. This theoretically enables peak powers greater than 10^{21} W/cm^2, using a fast focusing Off-axis Parabolic Mirror (OAP). The first amplifier stage contains a Cross-polarized wave (XPW) crystal for additional temporal pulse cleaning. As this component has to be aligned very precisely, the laser chain prior to this component was not changed after start up of the system. In the consecutive amplifiers, pump lasers have been switched on and off or detuned for alignment purposes, while operating the experiments, in particular to adapt the laser energy to specific alignment needs. The main amplifier (Multipass Cryo) crystal is cooled to $-170\,^{\circ}$C by a cryogenic pump. The cryogenic pump coupled severe vibrations onto the table of the main amplifier and was thus switched off for alignment purposes and full power shots, see Section 3.4.9. The laser has a beam attenutor situated before the main amplifier. After compression, the beam line has two components to improve the temporal laser profile (Plasma mirror, Section 3.2.3) and the spatial laser profile (Adaptive Mirror, Section 3.4.4). The laser system is connected to two radiation

shielded target areas, the experiments presented here were carried out in Target Area 2. Fig. 3.8 shows the layout of the JETi 200 infrastructure.

3.2.2. Temporal Laser Profile - Contrast

The laser temporal contrast is peak intensity divided by light intensity at other times, in particular light arriving prior to the main pulse. The laser contrast is usually considered on different time scales. A few ns before the arrival of the main pulse, Amplified Spontaneous Emission (ASE) originating from the amplifier crystals dominates. The relation between peak intensity and the ASE level is referred to as the ASE contrast.
For state of the art laser systems like the JETi 200 with a proper focusing optics, intensities exceeding 10^{21} W/cm^2 can be reached. Modification of a solid target due to fs pulses, typically occurs above 10^{13} W/cm^2 and for ns pulses at 10^{10} W/cm^2 for plastics. This defines the required contrast ratio. In this example a laser contrast of 10^8 would be a minimum requirement to leave the target unperturbed until the arrival of the peak pulse. From this crude estimate it is also evident, that with higher peak intensities the demands on laser contrast increase accordingly. Even though the best laser ion acceleration must not necessarily result from the best laser contrast, the best contrast possible is desired to gain control over the target parameters.
There are different techniques available to measure a laser's contrast curve. On nanosecond time scales prepulses can be measured by a fast photodiode. On the picosecond timescale, a third-order autocorrelator is used. These devices are commercially available, we used a SEQUOIA™ manufactured by Amplitude Laser Group. The actual pulse length on a femtosecond time scale was measured using a commercial WIZZLER™ by FastLite, which is based on self-referenced spectral interferometry (SRIS) [89].
Fig. 3.9 shows the autocorrelation curve of the JETi 200 laser scaled to the maximum intensity that we achieved in experiments. It has an ASE level of $\approx 10^{11}$, but multiple prepulses are visible, and hence were expected to dominate premature destruction of the target. Major effort is dedicated to identifying and eliminating these prepulses. As the laser chain consists of many different optical components, among which are transmissive optics (amplifier crystals, windows, polarizers or

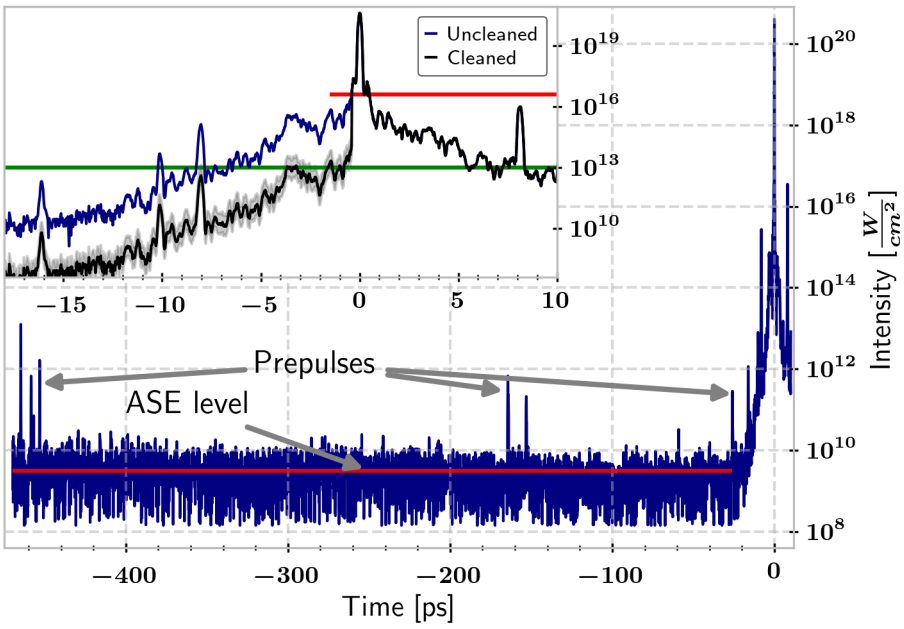

Fig. 3.9. *| Third order autocorrelator curve of the JETi 200-laser, measured with a SEQUOIA from Amplitude Laser Group. The intensity is scaled to the maximum intensity in the experiment. The red line represents the ASE level, and the green line the rising edge on the picosecond level. Several prepulses from the amplifiers are visible.*
Inset: Shows a zoom in to the central region around the main pulse, which was measured with higher temporal resolution. The red line shows the onsetpoint of the plasma mirror. The blue line is the measured curve without plasma mirror, and the black line illustrates the improved contrast, where the shaded area indicates uncertainties due to accumulated debris on the substrate. The green line indicates the damage threshold of plastics at 10^{13} *W/cm*^{2}*. Data credit to Alexander Sävert.*

Pockels cells), there are also many sources from which these pulses can originate. In the curve shown here, the pulses at −163 ps and −465 ps have the potential to ionize a target before the actual laser peak arrives, if no additional pulse cleaning techniques were applied.

At −18 ps the foot of the main pulse, which is referred to as the coherent pedestal, rises above the ASE level. From this point we can focus on the blue curve in the inset of Fig. 3.9. The damage threshold of plastic is reached latest 10 ps prior to the peak of the pulse, at this point in time the target turns into a plasma, it starts absorbing significant amounts of energy and expands. In the specific case of a laser pulse with a total beam energy of 1.6 J (25% of the 6.2 J quoted before), the integral over the curve up to −18 ps contains 0.07 µJ, and until −0.3 ps contains

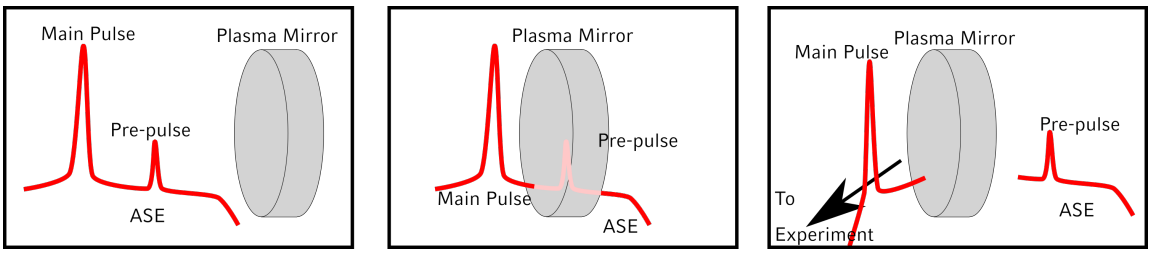

Fig. 3.10. *| The compressed pulse, including pre-pulses and ASE propagates towards the plasma mirror. ASE and pre-pulses pass through the mirror and the main pulse quickly ignites a plasma. The highly reflective plasma redirects the main pulse towards the experiment.*

460 µJ, which is enough to cause significant expansion, such that the density of an initially solid density sphere would significantly reduce before the main pulse interaction. For avoiding this uncontrollable pre-expansion we therefore applied a plasma mirror to suppress light preceding the main pulse.

3.2.3. Contrast Cleaning - Plasma Mirror

A plasma mirror is a widely used tool in the laser-plasma community to enhance the temporal laser contrast. It functions as a fast shutter, that separates the main pulse from the pre-pulses. This mechanism was for example demonstrated by [90] and has been widely studied for different setups since then, [91–94]. After the laser pulse has been compressed, it is focused on an optically flat surface. As long as the intensity is below $\sim 10^{13}\,\mathrm{W/cm^2}$, the light will transmit through the (typically AR-coated) surface. When the threshold for plasma generation is exceeded the surface transforms into a highly reflective mirror, see Fig. 3.10. The mirror position in the converging beam is chosen such that the peak intensity is well below $10^{17}\,\mathrm{W/cm^2}$, as for higher intensities on the mirror the reflected beam loses energy and collects wavefront deformation that reduce its focusability, [92]. For our temporal shape the plasma is formed roughly 2 ps before the peak of the main pulse. This switching point is in accordance with measurements by [95]. The reflecting surface stays intact for several picoseconds, before the plasma has expanded so far, that its scale length becomes comparable to the wavelength of the incident light and post pulses are efficiently absorbed or distorted. Due to this

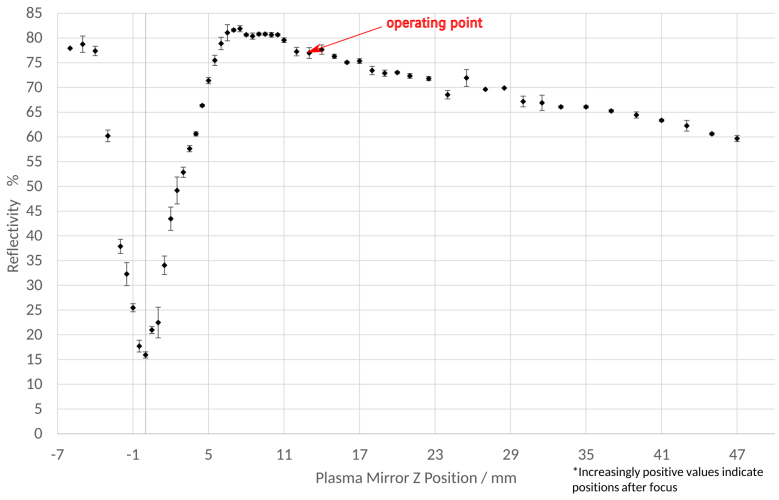

Fig. 3.11. *| Reflectivity curve of the plasma mirror. At a position of zero the focus of the parabola is on the silicate substrate's surface. Increasing distances result in reduced intensities on the substrate. Our experiments were performed at a position $z = 12$. Image Courtesy: Private Communication Alexander Sävert.*

short lifetime, a plasma mirror also serves as a protective element to secure the laser chain of back-reflected light from the target. A single plasma mirror, as used for the experiments in this thesis, can enhance the temporal laser contrast by two to three orders of magnitude. The plasma mirror used here was permanently installed in the laser beam-line as a bypass. By moving a mirror into the beam-line, the beam can be sent on a detour across a focusing parabola, the plasma mirror substrate and re-collimating parabola, before the second movable mirror guides the pulse back onto its original path along the beam-line. The parabolas had a focal length of 1.5 m and the plasma mirror is an Anti Reflection (AR)-coated silicate substrate, which was moved to a fresh position after each shot. The plasma mirror was adjusted to a position, where its nominal reflectivity was expected to be about 75%. This position was found, by measuring the mirrors reflectivity as a function of the longitudinal focus position on the plasma mirror, see Fig. 3.11. We decided for a position in which the peak intensity is slightly lower than optimal to ensure reliable rather than maximum performance. The substrate could accommodate a few 100 shots, before replacement. We observed that the reflectivity of the AR-coating increased on some parts of the mirror over time. The magnitude of this effect on contrast was not explicitly measured and also varied locally on the

substrate, but can be crudely estimated to have resulted in a factor of four to five higher pre-pulse level in the worst case. This would shift the plasma generation point in the target from $-2\,\mathrm{ps}$ to $-4\,\mathrm{ps}$ or $-8\,\mathrm{ps}$.

3.3. Diagnostics

3.3.1. Particle Spectrometer

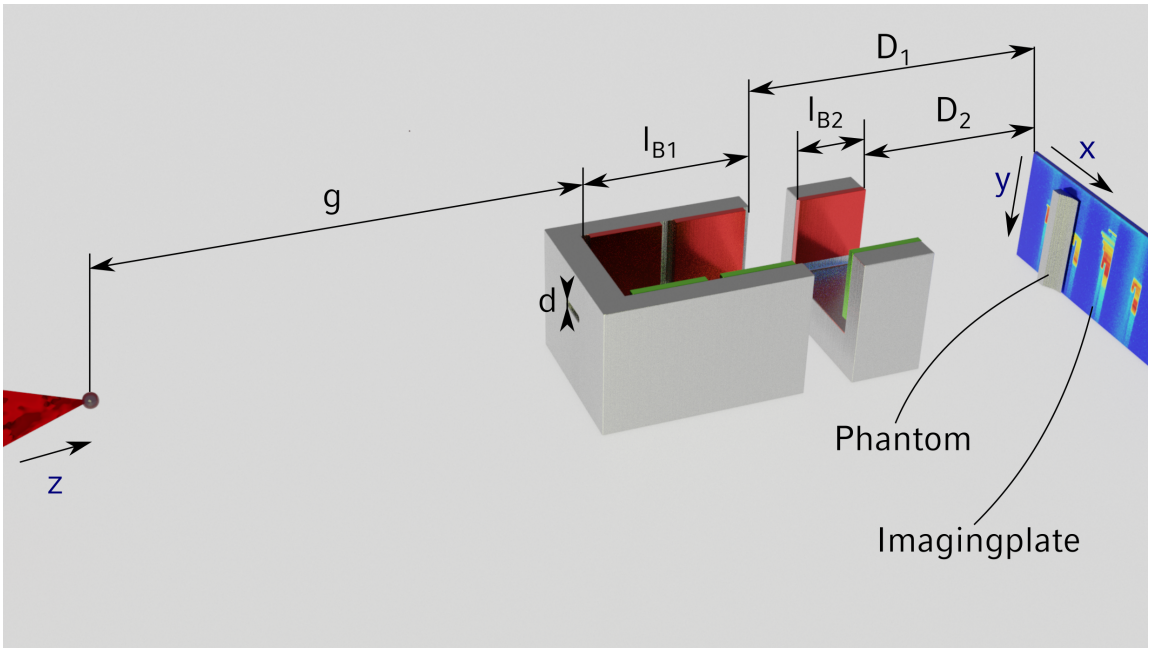

Fig. 3.12. *| Render of the particle spectrometer. Target Chamber Center (TCC) is on the left side, where the Laser interacts with the particle. The magnets of the spectrometer are mounted to two magnet yokes. Each magnet has a magnetization of the order of 1.4T and they are placed 140 mm apart.*

Determining the ion energy distribution relies on dispersing a small solid angle of the emitted beam (we use a horizontal slit with dimensions 0.4 mm or 1 mm) in a known magnetic field and detecting the ions thereafter on a two dimensional screen. We employ this Ion Wide Angle Spectrometer (iWASP), [96] in a mode that allows intrinsic calibration on the basis of the recorded data, without the need for cumbersome field measurements and particle tracking analysis. An iWASP

consists of two main components, a dipole magnet and 2-dimensional pixelated detector. A charged particle transversing a magnetic field $\vec{B}$ is deflected perpendicular to the magnetic field lines, and the particle motion by the Lorentz-force, [97]:

$$\vec{F} = q(\vec{v} \times \vec{B}). \tag{3.10}$$

Here $q = Z \cdot e$ is the particle charge, with Z as the particle charge number and e as the elementary charge and $\vec{v}$ is the particle velocity. Assuming a particle that is solely moving along the z-axis with a non-relativistic momentum $p = mv$ and a magnetic yoke of length l_B with a magnetic field B only along the x-axis, will deflected the particle downwards by $y = qB/2p \cdot l_B^2$ in the small angle approximation. After an additional drift D the particle hits the two dimensional detector. The total deflection in this case is

$$y(p) = \frac{qB}{p} \cdot l_B(\frac{l_B}{2} + D), \tag{3.11}$$

where the the kinetic energy $E_{\text{kin}} = p^2/2m$. Fig. 3.12 shows the setup of the magnet yokes. The magnets had a size of 100×100 mm with a magnetization of approx. 1.4 T. The magnets were mounted to two magnet yokes, where the first yoke was equipped with two magnet pairs and the second yoke had a single pair. The magnets were placed at a distance of 140 mm, yielding a magnetic field of approx. 0.1 T on the central axis.

The slit in the front plate of the magnet cuts out a fan beam from the initially divergent particle beams' opening cone. We used two configurations with a slit width of either 0.4 mm (shotnumber < 170) and 1 mm (shotnumber ≥ 170). As the slit is also thick (thicker than its opening), the dominant momentum for particles in the magnet is along the z axis. Without loss of generality, one can assume $p = p_z$ in Eq. (3.11). The double magnet setup as shown in Fig. 3.12, when assuming small deflection angles, yields a total deflection

$$y = \frac{q}{p} \cdot \left(B_1 l_{B1}(\frac{l_{B1}}{2} + D_1) + B_2 l_{B2}(\frac{l_{B2}}{2} + D_2) \right). \tag{3.12}$$

Aluminium Phantom

In principle, one could use the dimension along the slit for obtaining information about the angular distribution of the energy spectrum, that is to measure $dN/(dEd\Omega)(E,\phi)$. The shielding in front the Image Plates, BAS-TR (IP) allowed a horizontal opening at the slit position of 30 mm. As the slit was 520 mm away from the target, this covers an angle of $\delta\phi = 0.05$ rad, which is much smaller than the typically expected angle of divergence of the ion cone. Therefore, we use the 2 nd dimension (in the non-dispersion direction of the magnet) for calibration of the dispersion of the setup. For this purpose an aluminum phantom is applied as calibration tool to every shot. It consists of stairs with increasing

Table 3.1. *| Thicknesses of the Aluminum phantom in front of the Imaging Plate (second column). The Imaging plate was covered by* 50 µm *aluminum (shot < 191) or* 65 µm *for shots > 191, which was the setting for most shots. Exemplary the corresponding thicknesses and cut-off energies are given for the* 65 µm *setting. A thinner foil reduces the cutoff energies slightly. Cutoff energies are calculated using SRIM [98]*

ID	**Phantom** [mm]	**Thickness Filter** [mm]	**Energy (p^+)** [MeV]	**Energy (C^{6+})** [MeV/u]
0	0.0	0.065	2.6	4.7
1	0.1	0.165	4.6	8.5
2	0.2	0.265	6.1	11.3
3	0.5	0.565	9.4	17.5
4	0.9	0.965	12.8	23.7
5	1.6	1.695	17.7	32.5
6	2.2	2.255	20.8	38.1
7	3.2	3.265	25.6	46.9
8	5.0	5.065	32.8	60.0
9	7.3	7.345	40.3	73.9
10	9.0	9.015	45.3	83.0
11	10.8	10.865	50.3	92.2
12	12.8	12.865	55.3	101.4

aluminum thickness along the horizontal axis. The thicknesses of the phantom are listed in Table 3.1, along with the kinetic energies required for protons to penetrate this thickness [98]. Additionally the detector is covered in an aluminum foil with thickness 65 µm that is taken into account for the estimates. The thickness of this foil was changed during the experimental campaign from 50 µm (shotnum-

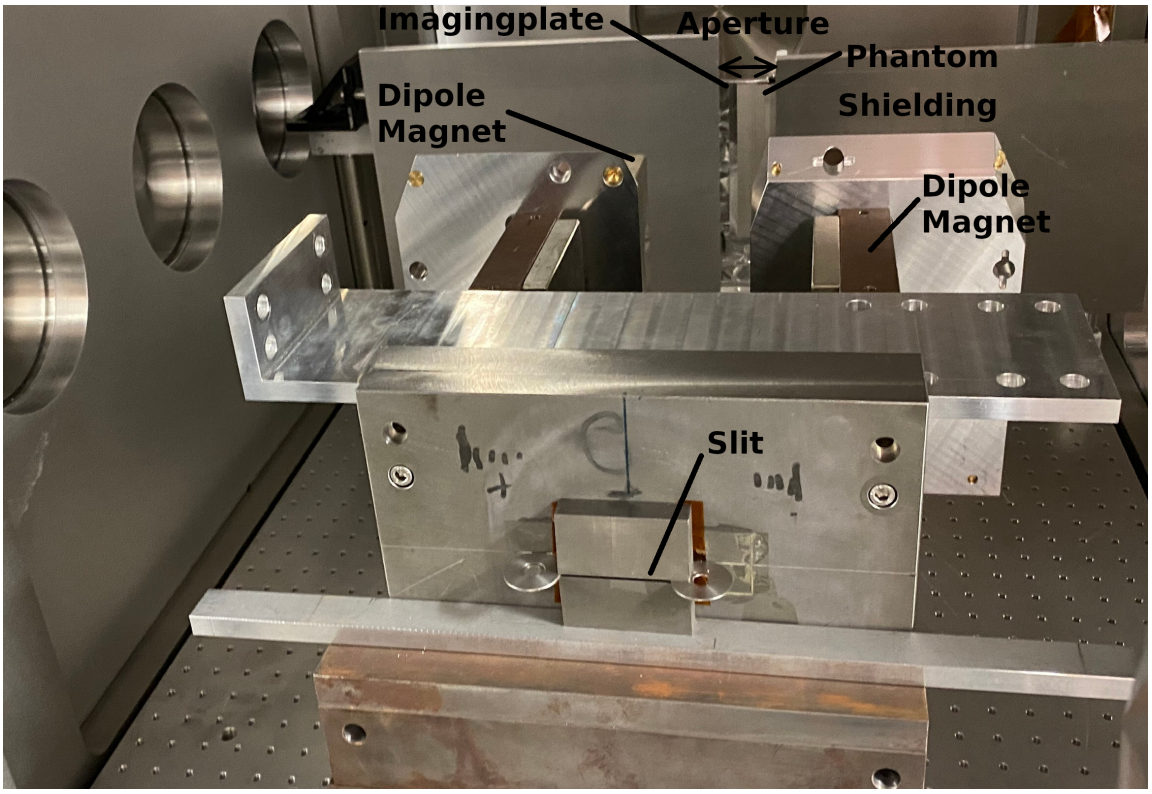

Fig. 3.13. *| Picture of the magnetic spectrometer along the laser axis. The front plate is covered by a two tungsten plates, separated by* 1 mm.*The second magnet is mostly hidden by the two aluminum plates between the two magnet yokes. In the image background the thickness filter (phantom) is visible. The non illuminated parts of the IP, are covered by 15 mm thick aluminum plates.*

ber < 192) to 65 µm (shotnumber > 192). Most of the evaluated data was acquired with 65 µm. As only particles in excess of a certain energy can reach the detector, lower energetic particles are not creating a signal on the detector and a low energy cut-off line is visible in the recorded 2D image. These lines are used to relate the vertical (y)-deflection to the particle's kinetic energy at discrete points. The phantom was designed to create such a cut-off line approximately every 5 MeV, so that the remaining points of the spectrometer dispersion function $y(E)$ could be linearly interpolated. The calibration therefore required only one good shot (i.e. a few real shots) with broad energy distribution. Fig. 3.13 shows a picture of the spectrometer in the experimental chamber. In this image the front plate was equipped with a 1 mm slit from two tungsten blocks.

Table 3.2. *| Configuration of the iWASP spectrometer*

Parameter	Distance [cm]
l_{B1}	24.0
l_{B2}	10.0
D_1	44.5
D_2	29.0

3.3.2. Energy retrieval

To associate the points x,y on the detector to energy values, Eq. (3.12) is insufficient because of the inhomogeneous magnetic field, in particular along the slit (x-direction). [99] explored a power series expansion for the axis of symmetry (horizontal coordinate along the slit), to model the magnetic field as,

$$B(x) = a \cdot (x - x_0)^4 + b \cdot (x - x_0)^2 + c. \tag{3.13}$$

Here a is the contribution of the quadruple term, b is the contribution of the quadratic term, c is a parameter of the order of the magnetic field in units of Tesla and x_0 is the horizontal offset of the magnetic field central axis in units of cm on which Eq. (3.12) defines the deflection in y. Combining with Eq. (3.13) yields the fitting function, that relates all positions (xy) on the detector to the particle's momentum:

$$p(x,y) = \frac{q}{m_0 c} \cdot \left[l_{B1} \cdot (\frac{l_{B1}}{2} + D_1) + l_{B2} \cdot (\frac{l_{B2}}{2} + D_2) \right] \cdot \frac{B(x)}{y - y_0} \tag{3.14}$$

The additional parameter y_0 accounts for the vertical offset of the projected slit position on the 2D detector in cm. Experimentally, (x_0, y_0) is coarsely defined by a laser sent via the main laser focal point through the slit in the dipole magnet's front plate onto the detector. The parameters a, b, c, x_0, y_0 are parameters that are fitted based on the energy cut-off positions. The remaining free parameters in Eq. (3.14) are given by the geometrical setup in the experiment and listed in Table 3.2. In practice we used two representative spectrograms (i.e. detector images) in which the cut-off lines were visible and used 9 pairs of $x(E)$, $y(E)$ to fit equi-energy lines to the proton picture. For the low energetic cutoff-lines up to ID = 1,2 and 3

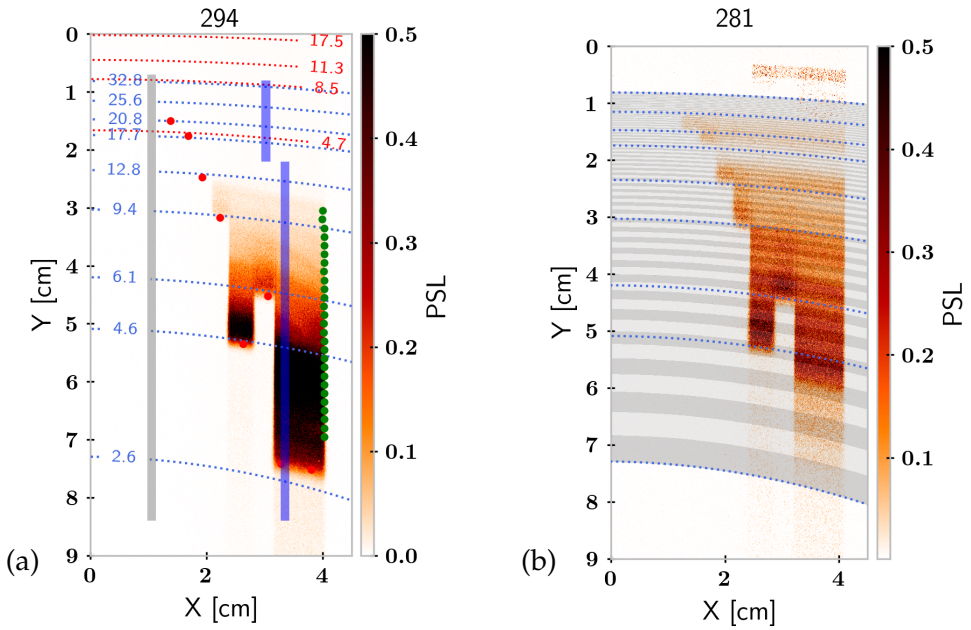

Fig. 3.14. *(a) IP image of the foil shot 294. Green and red dots are fitted using the half-maximum method. The green dots give the horizontal orientation of the spectrum, and red dots are used as support points for the energy grid fitting routine. Red dots are the xy-positions of a proton with known energy due to the aluminum phantom. Blue dashed lines denote lines of equivalent energies for protons, whereas red dashed lines denote lines of equivalent energies for C^{6+} in units of [MeV/u]. The blue boxes denote the areas, where the spectrum is extracted. The gray box is used to extract a background level for each energy bin. (b) image of shot 284, with overlayed energy bins of $dE = 0.3\,\mathrm{MeV}$.*

(see Table 3.1) we used a 100 nm foil shot (294) and for the higher energetic cutoff-positions we chose a pre-expanded 1 µm shot (281). These covered the positions with $ID = 4$, 5 and 6. Each cutoff point corresponds to a specific momentum p with the coordinates, (x, y, p), which were fed into the fitting routine. The result is referred to as the energy grid, consisting of calculated equi-energy lines that can be overlaid onto the detector image as shown for the two reference shots in Fig. 3.14. The equi-energy bins in Fig. 3.14 indicate the decreasing resolution of the iWASP detector with increasing particle energy. The energy resolution of the spectrometer is dictated by the point projection of the slit width d on the detector.

In our case

$$\frac{\Delta E}{E} \approx \frac{d}{y} \approx 0.13 \tag{3.15}$$

3.3.3. Detector replacement

We used an IP of a DIN A 4 size, which could fit up to 4 shots and had to be moved to a new position after each shot. This was done by a motorized stage. After four shots the detector had to be replaced. The replacement was accomplished by a double door system to avoid venting the whole vacuum chamber for this exchange. The replacement system was held in place by permanent magnets, to ensure reproducible positioning. It later turned out that the accuracy of ± 1 mm, required manual post processing to overlay the energy grid properly for every shot.
On each shot we applied a half-maximum edge detection algorithm along the vertical and horizontal axis. The edge introduced by the shielding in front of the IP served as a measure to align each shot horizontally (green dots in Fig. 3.14 a). We applied an edge detection technique and tracked the point, where the signal reached half maximum along the horizontal axis. The image was then shifted such that the edge was aligned for every shot before data evaluation. For the vertical direction we also applied the edge detection along every cut-off line, which resulted in the red dots in Fig. 3.14 (a). The image was then moved and aligned by eye for each shot separately such that the cut-off positions in the shot align best with the cutoff positions in the energy grid.

3.3.4. Imaging Plates (IPs)

As a detector we used a BAS-TR type IPs, which were scanned using an Amersham™Typhoon™IP scanner. IPs are commonly used as a reusable detector for X-Ray imaging. But it has also been widely used in the laser plasma experiments as a detector for charged particles, e.g. [100–102]. IPs can store energy deposited by ionizing radiation in a meta stable state by creation of electron-hole pairs in the 50 µm thick active (BaFBr:Eu^{2+}) layer. The stored energy can be released and digitized by illumination of the detector with a red laser, 633 nm HeNe laser. The

released signal is proportional to the intensity of the illuminating light and the density of electron-hole pairs in the active layer. This effect is called (Photo Stimulated Luminescence (PSL)).
The BAS-TR type IP have no protective layer. This makes them applicable to low energetic ions, but they have to be treated with great care to prevent damage of the sensitive surface, which is directly exposed to the radiation. This layer is on top of a 250 µm thick polymeric support layer and a 160 µm thick magnetic layer [101, p. 74]. The stored energy is read out from the IP by exciting the meta stable state. When the meta stable state is excited to the conduction band, it decays to the ground state while emitting a 387 nm photon. The emitted photons are amplified and recorded by a photo multiplier tube. IP have a tremendous dynamic range of more than 5 orders of magnitude, exceeding the dynamic range of the scanner system, which allows for multiple read out of the detector. The cumulative signal of emitted photons is proportional to the deposited energy by the ionizing radiation. The IP scanner stores the data in a logarithmic compressed format, the quantum level (QL). Imaging plates may be reused after being erased by illumination with a homogeneous light source.
The IPs were scanned with a spatial resolution of 50 µm. The sensitivity of the scanner was $S = 4000$, the latitude or level $L = 5$ and a bit depth of $G = 16$. Using the formula provided for the quantum level (QL), which is stored in the '*.img'-file, the PSL value for each pixel is calculated as, [103]:

$$PSL = \left(\frac{R}{100}\right)^2 \times \left(\frac{4000}{S}\right) \times 10^{L\times\left(\frac{QL}{2^G-1}-\frac{1}{2}\right)} \tag{3.16}$$

IP Scanner cross calibration

This PSL value correlates to the energy deposited in the pseudo pixel and can be associated to a number of particles, given the mean energy loss per particle is known. From a physical point of view the signal level is proportional to the energy loss of a particle, when passing the detector. Additionally, the sensitivity of the IP in combination with the used scanner has to be calibrated. As there is a variety of Imaging Plate scanners on the market, this measurement has been done for most of the older scanner types. The manufacturer pre-calibrates the system such that among one item type the sensitivity is the same. Calibration results can

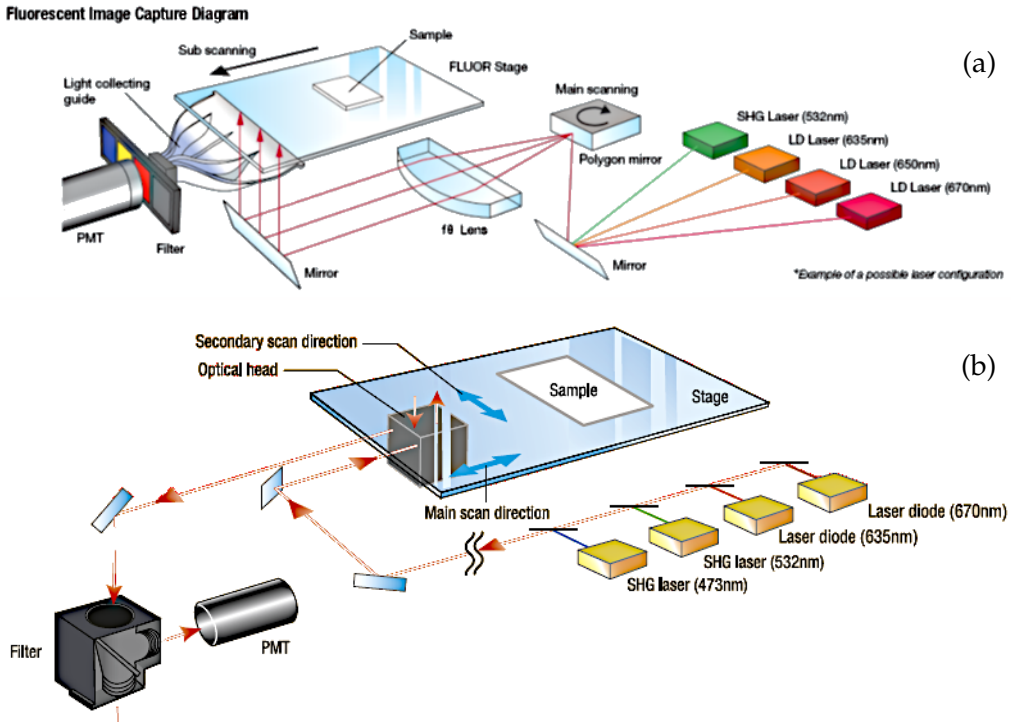

Fig. 3.15. *| (a) FLA7000: Scanning principle. A cylindrical lens creates a scanning line, that is moved across the sample. The signal along the lines is leached. (b) FLA5000: Scanning principle. The sample is scanned via a pencil beam scanning, where only one pixel is excited for digitization. Image adapted from: © Copyright Cytiva – Reproduced by permission of the owner.*

thus be transferred from one system to the other. There are two main scanning concepts for imaging plates, see Fig. 3.15. The FLA 7000 series scans the samples line by line, the FLA 5000 series scans the sample pixel wise. Hence, the FLA 7000 requires much shorter scanning times, but is accompanied by leaching along the scanning line, altering the recorded signal. New, high precision systems use an improved setup following the same working principle as the FLA 5000 scanner. The new Amersham™Typhoon™IP scanner, used in this thesis, uses the same pixel scanning principle, as the FLA 5000 scanner, that was characterized by in a previous thesis work [100]. We expect the new scanner to have a similar functional response to the signal stored in the sample, but due to significant changes in the sensitivity, the new sensor has an offset to the old scanner.

Therefore, the linear offset was measured by a calibrated C-14 β-source from raytest Isotopenmessgeräte GmbH (serial nb. 0496 CV/008) with an activity of

22 kBq. Imaging plates were illuminated for 5 min with the test source and scanned right after that with both the FLA 5000 and the Amersham™Typhoon™IP scanner. The results are shown in Fig. 3.16 (c). It was found that the Amersham™Typhoon™IP scanner delivers a lower PSL level, with the same dose deposited in active layer of the IP. This means that the calibration curve of $\#/PSL/dE(E)$, as found by [100] and described in Section 3.3.5, has to be down scaled by a factor of $\alpha = 1/1.68 = 0.6$, as detailed in Fig. 3.16 (b).

Bleaching of IPs

IPs suffer from signal loss, especially in the first minutes after irradiation. There are two main decay channels for the meta stable state. The fast decay over the first tens of minutes and the second, slower decay lasting several days. Fading of the signal is usually measured by exposing the IP to ionizing radiation from radioactive sources, which require an integration time of the same order as the first, fast decay process. These measurements are capable of resolving the slow decay, but can not estimate the fast decay, which is always relevant for laser plasma experiments with the exposure times in the order of ps, which is quasi instantaneous. The decay was measured by [104]. In real experimental conditions the detector is usually placed in vacuum and the signal level is not related to $t = 0$, but rather to $t = 30$ min, which is a typical timescale to get access to the vacuum chamber. Alejo et. al. [104] found a heuristic correction correlation of the form

$$PSL_{30} = \left(\frac{30}{t}\right)^{-0.161}, \tag{3.17}$$

where t is the time between irradiation and scanning in minutes. In our experiments we accumulated four shots on a single IP, before it was replaced and scanned. The time delay between irradiation and scanning varied from 20 min for the last shot on the detector up to more than 100 min for the first shots and the scan time was approx. 20 min, which is shown in Fig. 3.16 (a).
The PSL values were corrected for the variations in delayed readout using Eq. (3.17), although the overall contribution of this effect to particle number uncertainties is around 20%. The main uncertainties arise from the energy dependent calibration of PSL to particle numbers. Due to the statistical nature of energy loss in thin sen-

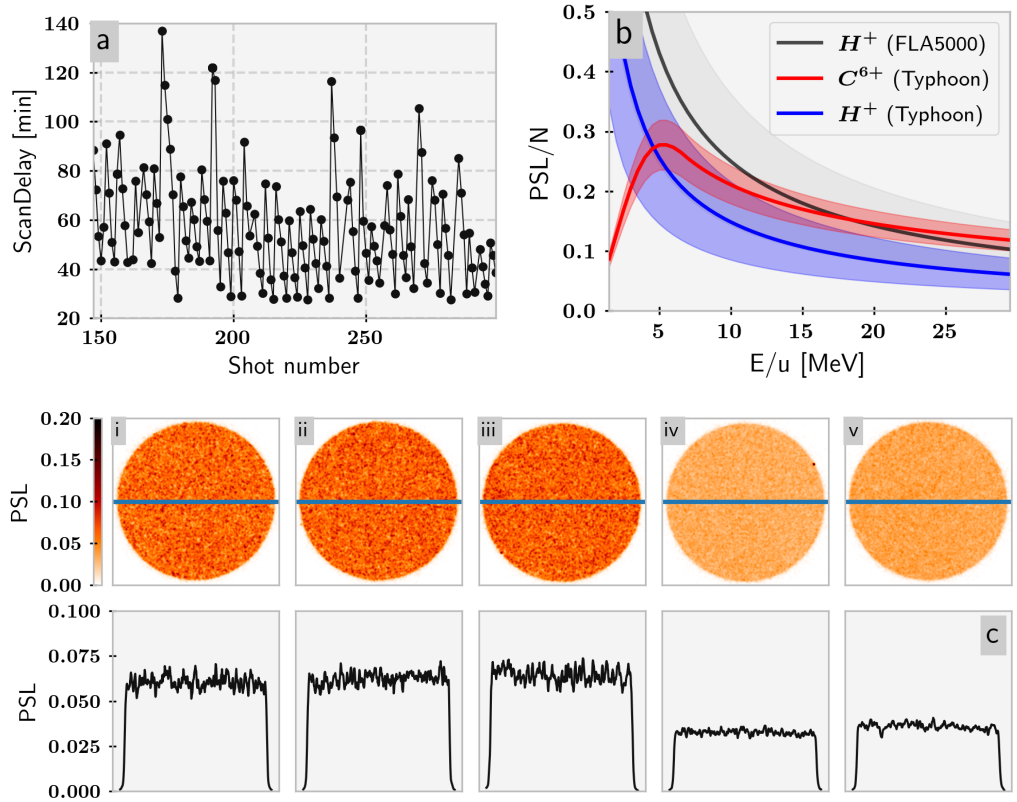

Fig. 3.16. *(a) 4 shots are accumulated on a single IP. The delay between illumination and scanning is therefore unique for each shot. The delays here are relative to the finishing time of the scan. Each scan took approx.* 20 min. *(b) Calibration of the PSL to particle numbers. The black curve shows the calibration of the FLA 5000 scanner as estimated by [100]. Using the calibration factor to the Typhoon scanner yields the blue curve. The red curve is the calibration of PSL to* C^{6+} *as determined by [103] for the FLA 5000 scanner, already corrected for the Typhoon scanner. (c) (i-iii) PSL-level after* 5 min *of illumination and scanned with FLA 5000. (iv-v) PSL-level after* 5 min *of illumination and scanned with Amersham™ Typhoon™ IP. The bottom line shows vertical line outs, as an average over 100 lines. The conversion factor is 1.68.*

sitive layers. In the data presented here, the signal fading adds an uncertainty up to 20% to the particle number, which we corrected for in the data. However, this 20% uncertainty in the data is still far less than the uncertainty band given by the conversion from PSL to particle numbers, in Fig. 3.16 (b).

3.3.5. Proton and Carbon Particle Numbers

Before converting the PSL signal to proton numbers, we subtract a background signal level from the PSL count. The Bethe-Bloch [105] formula can be written in the form

$$\frac{PSL}{\#p}(E) = \frac{A}{E}\ln(B \cdot E), \tag{3.18}$$

with $A = \alpha \cdot 0.5 \pm 0.2$ and $B = 15 \pm 3$ [100] and $\alpha = 0.6$ being the correction for the new scanner generation. E represents the proton energy at the respective detector position $x(E), y(E)$ minus the energy lost upon penetrating the phantom at this position in MeV. The energy loss in the phantom is calculated with SRIM [98].
The calibration for carbon ions, however, is more complicated, in particular for energies of a few MeV/u, because their Bragg peak lies within the sensitive layer. Doria et. al. [103] calibrated the energy loss in the IP for different charge states and fitted an empirical functional dependency. For the low energetic particles they fitted a fourth order polynomial and power-law function for high energetic carbon ions:

$$\frac{PSL}{\#C^{6+}}(E) = \begin{cases} (d + c \cdot E + b \cdot E^2 + a \cdot E^3) \cdot E & 0 \leq E \leq 73.6\,\text{MeV} \\ 4.55 \cdot E^{-0.533} & E > 73.6\,\text{MeV}, \end{cases} \tag{3.19}$$

with $a = 4.6 \times 10^{-8}$, $b = -8.9 \times 10^{-6}$, $c = 4.46 \times 10^{-4}$, $d = 2.51 \times 10^{-3}$. The uncertainty in the calibration is given as an relative error of $\pm 15\%$, after correcting for the signal fading within the first minutes.´

3.3.6. Spectrum retrieval

The differential energy spectrum was calculated from a vertical stripe with a width of 30 px (1.5 mm) along the thinnest aluminum filter, covered by 65 µm aluminum, see blue boxes Fig. 3.14 (a). As the proton signal overlapped with the carbon signal for proton energies above 18 MeV, the evaluation stripe was moved to the third thinnest filtered phantom for proton energies > 15 MeV, so that overlap between carbon ions for proton up to 30 MeV was prevented (which is a proton energy that we did not reach in this experiment). The spectrum was retrieved by moving the slit projection of 36 px ($\equiv$ 1.8 mm) along the vertical direction of the energy grid and the IP image. The particle number is given as the sum over the pixel values in the bin, and the particle energy is the average value within that bin. The evaluation box equals an solid angle of $\sim 2.08 \times 10^{-6}$ sr for an slit opening of 1 mm.
The same evaluation was done along a second stripe in an area that was covered by 15 mm aluminum and thus without proton signal, to obtain the noise level of the detector (grey bin in Fig. 3.14 a). The noise level was subtracted from the signal bins before the PSL value was converted to particle numbers. We only considered values with particle numbers $>7 \cdot 10^6$ for the evaluation and dropped lower values. Fig. 3.17 a, b show an example of the spectrum retrieval from the PSL values. It uses the two shots, that were used for the grid calculation. The data includes the raw signal in the data stripe, the noise signal in the reference stripe and the difference between the two. The resulting proton spectrum after converting to particle numbers is shown in Fig. 3.17 c, d.

3.4. Experimental design

The experiment was the first one carried out in target area 2 of the JETi 200. The target area facilitates two experimental chambers, referred to as the beamforming chamber and the experimental chamber. The beamforming chamber was used to create a pre-pulse and the experimental chamber hosts the actual target system and diagnostics. Fig. 3.18 shows the experimental setup. The pre-pulse was picked at the central beam height of 30 cm in the outer area of the beam by a 1 inch mirror. Thereafter the beam diameter was reduced to 6 mm and guided over a de-

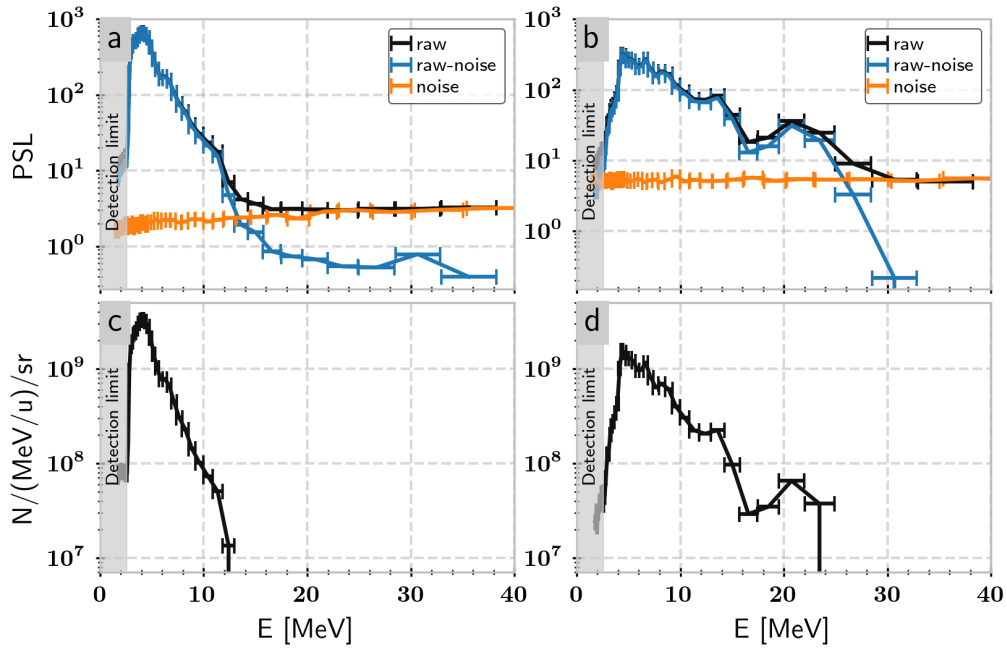

Fig. 3.17. *| (a, b) Show the PSL counts in the evaluation bins for shots 294 and shot 281, respectively. The noise level was subtracted from the raw proton psl counts. Conversion of PSL to particle numbers applying Eq. (3.18) yielded the proton spectra (c, d)*

lay stage, which allowed tuning the relative delay between pre- and main-pulse from -1800 ps to 100 ps. Using a motorized mirror the pre-pulse was coupled back by a mirror in the shadow of the pic-off mirror, so that it co-propagated with the main pulse and is focused by the main OAP mirror.

The pre-pulse was planned for a peak intensity of $10^{16}\,\mathrm{W/cm^2}$ corresponding to $a_0 < 0.1$, assuming that the main pulse had a flat top beam profile with 120 mm in diameter and a pulse energy of 2 J. The peak intensity was chosen to be in accordance to the previous pump-probe expansion studies of a 1 µm spheres at the ZEUS laser [88]. As will be explained in Section 3.4.5 the peak intensity was lower than estimated, because the beam energy in the chamber was < 2 J and the main pulse did not have a flat top profile. The re-coupling mirror was used to perfectly overlap the pre-pulse and the main pulse in the focus. The overlap was checked and adjusted, whenever the delay stage was moved to a different delay setting. The focus diagnostics consisted of a 20-times Mitutoyo objective with a 200 mm lens and a AlliedVison Manta G-419 NIR camera positioned on air, see Fig. 3.21 (b). As the main pulse had a significantly tighter focus and more energy,

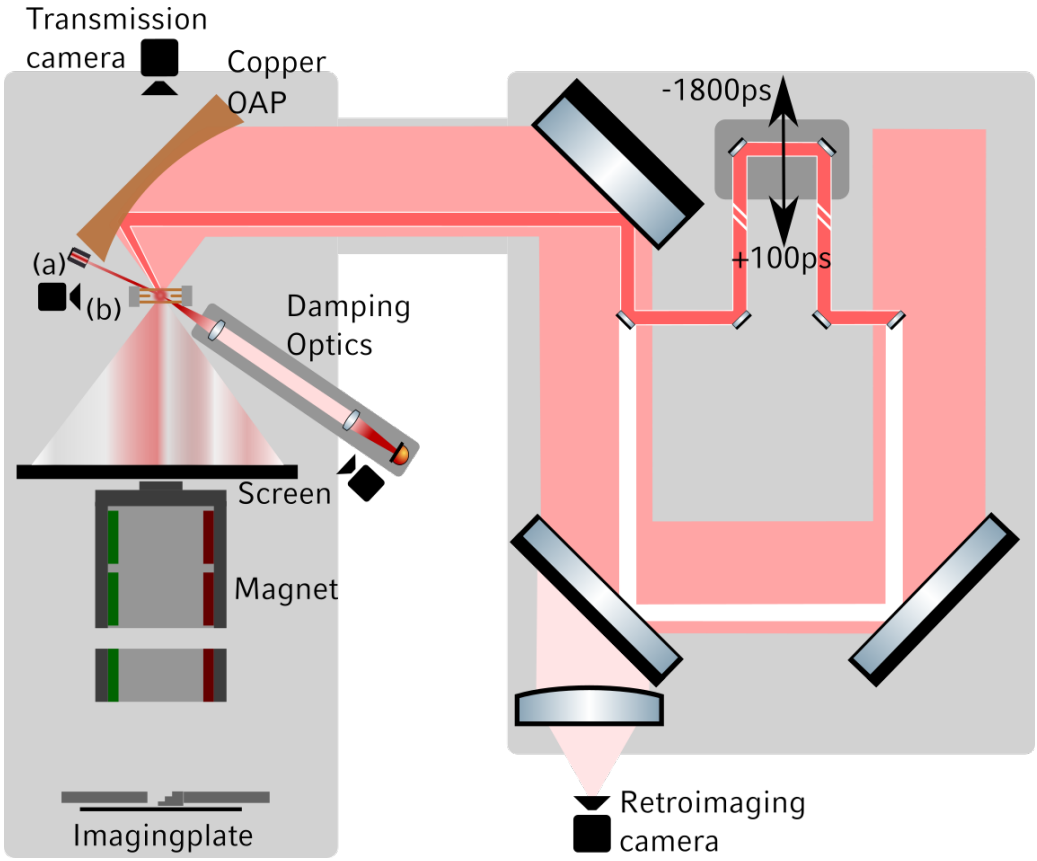

Fig. 3.18. *| A small portion of the beam is picked, and sent on a detour to adjust the delay between pre- and main pulse. A delay stage was used to tune the pre-pulse delay between* −1800 ps *and* 100 ps*. Cameras monitored the interaction, in particular backscatter light (retroimaging camera) and transmitted light captured on the screen (transmission camera). An iWASP, consisting of a wide gap magnetic field and imaging plates as detectors served for ion spectrometry.*

a ND filter was moved in and out of the collimated part of the focus diagnostics to ensure proper illumination of the chip for both configurations.
The point t_0 is defined as the delay line position, when both pulses reach TCC simultaneously. This zero-delay was estimated by probing the air plasma of an attenuated main pulse with the pre-pulse. The pre-pulse delay was tuned relative to the main pulse until the onset of the air-plasma was visible in the transmitted beam profile of the probe. We defined t_0 as step count of the delay stage, where no air-plasma was visible, but was closest to the onset. The onset could be found with a precision of 50 steps. Thus this method enables an timing accuracy of ± 1 ps.
The JETi 200 laser provided a 32 fs pulse at a central wavelength of 800 nm. We used a 90° copper OAP with a focal length of 180 mm, which resulted in f/1.5 focusing at a beam diameter of 120 mm, and a f/30 focusing optics for the pre-pulse. The focus distribution was optimized by applying an adaptive optics mirror.
Downstream the laser focus in a distance of 525 mm, an anodized aluminum plate was imaged by a camera and served as a scatter screen for the transmitted laser light. Additionally to this transmission camera, 3 more cameras were in place. One was looking from 60° to the laser axis in forward direction, with a large field of view to gain an overview of the target. The second camera monitored the back scattered light, which was collimated by the copper parabola, transmitted through a turning mirror and focused on a camera outside of vacuum by a 4 m lens. This camera ensured proper transverse positioning of the target until the actual full power shot. A third camera recorded scattered light in the vertical direction above TCC, and was used as a hit quality monitor of the full power shot.
The iWASP was placed under 0° directly behind the transmission screen.
We used spherical Polystyrene (C_8H_8) (PS) spheres with a diameter of 1 µm , 2 µm and 7 µm as targets. Table 3.3 lists the according number of particles contained in the targets with the exact particle diameters. The majority of shots was performed on 1 µm spheres. In total, 83 shots on spherical and 10 shots on foil targets are included in the presented work.

3.4.1. Pre-Pulse Estimate

The main purpose of the experiments was reaching the critical density via pre-expansion triggered by a short, intense pre-pulse. On one hand, the intensity

Table 3.3. *| Target parameters for polystyrene spheres. Sphere diameters were specified by Microparticles GmbH.* 1 µm *particles were from two batches with slightly different diameters. Shots with shotnumber* > 278 *had a diameter of* 1.01 µm

Diameter	n_e	N_e	N_p, $N_{C^{6+}}$
7.06 µm	$3.4 \cdot 10^{23}$	$6.26 \cdot 10^{13}$	$5.59 \cdot 10^{12}$
1.96 µm	$3.4 \cdot 10^{23}$	$1.34 \cdot 10^{12}$	$1.910 \cdot 10^{11}$
0.96 µm–1.01 µm	$3.4 \cdot 10^{23}$	$1.58–1.83 \cdot 10^{11}$	$2.25–2.52 \cdot 10^{10}$

must be sufficiently high to safely ignite the pre-plasma even under experimental limitations (which we indeed encountered), i.e. much higher than $10^{14}\,\mathrm{W/cm^2}$. On the other hand, the pulse should not trigger relativistic motion, so that pre-expansion happens in a regime that is well understood, i.e. $I_{pp} < 10^{16}\,\mathrm{W/cm^2}$. We targeted $10^{16}\,\mathrm{W/cm^2}$, based on 2 J of laser energy in a 120 mm flat top main pulse. Assume that the derived pre-pulse will eventually initiate hydrodynamic expansion [106] at the ion speed of sound, $c_s = \sqrt{Zk_BT_e/m_i}$, where Z is the ion charge, k_b is the Boltzmann constant and T_e is the electron temperature and a conversion efficiency into hot electrons of $n \sim 0.1$ [107] for an initially solid sphere. The electron energy $k_BT_e = E_e$ is estimated as the absorbed energy, that has passed through the geometrical overlap between the pre-pulse and the target. For fully ionised polysterene targets, with $n_0 = 195\,n_c$, the target radius has to increase by a factor of ~ 6 to reduce the initial density to n_c. We expect an absorbed energy of $E_e \approx 0.1\,\mu\mathrm{J}$, and a sound speed of $c_s \approx 0.02\,\mu\mathrm{m/ps}$, for carbons and hence an expansion time of approximately 130 ps. This estimate is in line with pump-probe experiment results of the 1 µm spheres [88], where we observed a radial Gaussian density distribution, for expansion times exceeding 100 ps. As this estimate is rather crude, in particular because of many unknown parameters (in particular the absorption and ionisation dynamics), we experimentally investigated delays between -1200 and 0 ps.

3.4.2. Energy measurement and beamline transmission calibration

We measured the transmission through the compressor, beam-line and plasma mirror relative to the energy before compression using a Gentech energy meter. As this measurement could only be performed with the experimental chamber

vented, we could only use an attenuated pulse for the measurement, with 760 mJ pulse energy before compression. The measurement results are shown in Table 3.4. With the vented experimental chamber the pulse had to pass an additional sapphire window, with a transmission of $\tau \approx 93\,\%$ at 800 nm at each surface. Without the plasma mirror, the energy in the chamber was measured with 317 mJ, and 364 mJ, if corrected for the sapphire window. This yields an overall transmission of the compressor and the beamline of $t_{noPM} = 48 \pm 1\%$.
With plasma mirror a pulse energy in the chamber of 150 mJ was measured, amounting to 174 ± 1 mJ if corrected for the sapphire window. Compared to a full power shot, the reduced energy in this measurement means that the plasma mirror setup had a transmission of 47%, but was of course not operated in its ideal condition. Reducing the beam energy is equivalent to a reduced intensity, which could also be achieved by moving the plasma mirror substrate along the axis of the focusing OAP, as in Fig. 3.11. We have adjusted the focusing OAP position to yield a reflectivity of about 75% of the pulse, which is slightly below the peak for maximum reflectance. In accordance with reflectivity curves from literature, e.g. [93], we find that an order of magnitude less intensity on the substrate reduces the reflectivity by $\sim 15\%$. Correcting the measured energy for the increased reflectance of a full power shot, the effective energy in the chamber is $t_{wPM} = 198 \pm 4$ mJ. From this we estimate a total transmission through compressor, plasma mirror and beamline of $t_{wPM} = 26 \pm 3\,\%$, meaning that the plasma mirror setup (including focusing optics and additional mirrors), has a transmission of 52%. This is significantly lower than the forward estimate of 75%. One reason is that we had a significant clipping in the beam path through the plasma mirror setup, which yielded a loss of pulse energy. Additionally we observed that the plasma mirror introduced a gradient on the initially nearly flat top beam profile. Both effects hint at imperfect operation conditions, which could not be resolved in due time.
The nearfield of the laser was monitored after a leakage of a mirror between compressor and plasma mirror. This allowed judgement of significant relative changes from shot to shot.
We measured the pulse energy before the start of the experiment and then relied on the calibrated integral of the profile recorded on the transmission camera (recorded without a target) as a monitor of the laser energy over long time scales. This allowed identifying significant drifts on a day to day basis. The calibration

Table 3.4. *| Six shots with 760 mJ ±2% before compression were applied into the chamber. Measured energies with and without plasma mirror.*

Energy with PM	Energy without PM
150 mJ	312 mJ
145 mJ	321 mJ
155 mJ	317 mJ

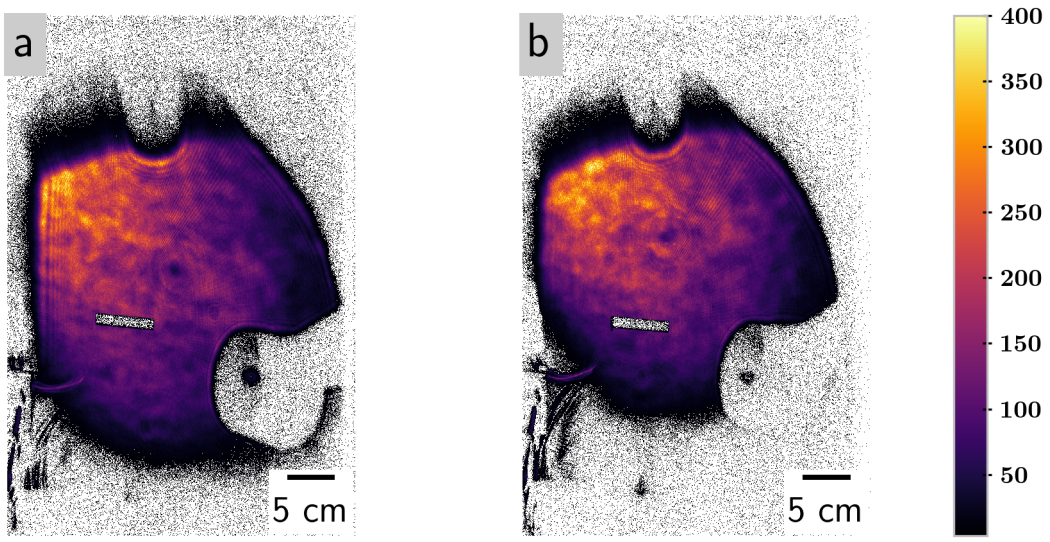

Fig. 3.19. *| Background subtracted empty shots at the beginning (a) and towards the end (b) of the campaign. The beam drift led to reduced energy in the main beam as well as the in the pre-pulse.*

was done after shot 113, which is the standard shot to which the other empty shots without target are related to and proofed to be very useful in post experiment analysis, as we identified pulse energy drifts over rather long time scales.

3.4.3. Pulse Energy Drift

The integrated pulse energy was subject to fluctuations. On a shot to shot basis the energy before the compressor varied between 6.1 J and 6.5 J, yielding an average energy of 6.2 J and a relative fluctuation of 6%. The losses through the beam-line were dependent on the alignment and the beam profile varied slightly from day to day. Especially towards the end of the campaign after a three weeks pause,

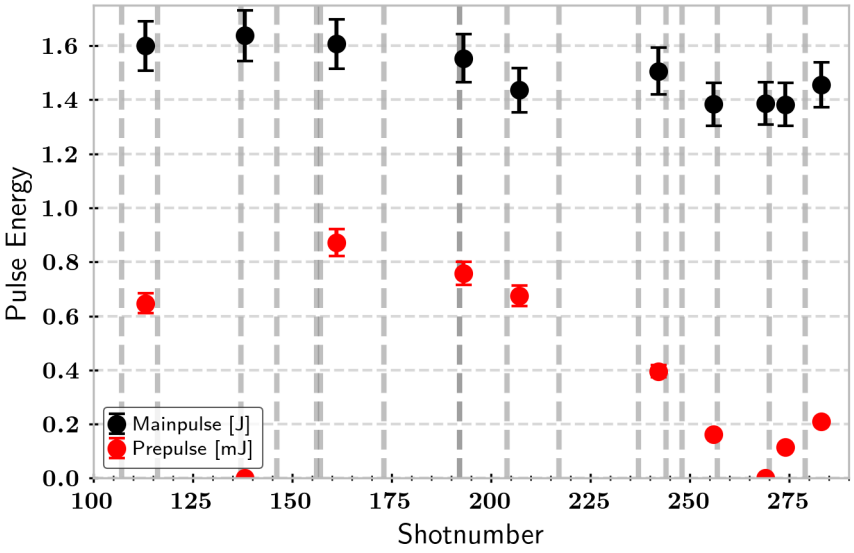

Fig. 3.20. *| Pulse energy on target. Energies are extracted from empty shots, i.e. full power shots without target. The transmission of the known reference shot 113 is used as a calibration for the integrated signal of the other empty shots. The measurement uncertainty is defined by energy fluctuations and uncertainties in the beam line- and plasma mirror transmission. Vertical lines correspond to different experiment days.*

the beam shifted to the upper left due to unforeseen changes in operation. The shift is illustrated in Fig. 3.19, showing an exemplary beam profile recorded on the transmission screen at the beginning and the end of the campaign. Integrating the signal of the two images shows that the pulse towards the end of the campaign contains about 10 % less energy than in the beginning, see Fig. 3.19(a). This effect is even stronger for the pre-pulse, which is picked at the rim of the beam profile. Its pulse energy is reduced to about 20% of its initial energy. For the reference shot 113, we estimate the pulse energy in the chamber to $(1.6 \pm 6\%)$ J, and a pre-pulse energy of $(640 \pm 6\%)$ µJ. Towards the end of the campaign, shotnumber $>$ 200, the main pulse energy dropped to $(1.4 \pm 6\%)$ J and the pre-pulse energy to 200 µJ. Fig. 3.20 shows the result of the evaluation of all empty shots throughout the campaign. This analysis allows assigning laser pulse energy to certain periods throughout the experimental campaign. As we will see later, this is a decisive clue, in particular for understanding the results obtained with large pre-pulse delays at different phases of the experiment.

3.4.4. Focus optimization

Adaptive optic mirrors have become a standard in high power laser chains with extended beams to enhance the focus quality. They are used to correct for wavefront aberrations that originate from mechanical manufacturing uncertainties. In our case especially the milled copper OAP is of comparably low optical quality and the milling rings are actually visible on the OAP surface. As these aberrations are static and do not change during the laser operation, the adaptive optics is ideally suited to compensate for imperfections. The loop is normally applied once after the initial laser start up and warm up phase.
In a basis transformation the spatial phase of the laser (or wavefront) can be decomposed into Zernike modes. The lower modes represent tip, tilt and defocus, which can also easily be compensated by proper alignment of the optical components. The deformable mirror can compensate remaining lower mode imperfections, but is mostly required for higher modes. The number of compensated modes is to be defined by the operator, minding the increasing noise at higher mode numbers. The setup for the wavefront measurement is integrated into the focus diagnostics. Fig. 3.21 shows a picture and a schematic drawing of the setup of the wavefront measurement. A $20\times$ Mitutoyo objective with a 300 mm lens imaged a plane about 10 m downstream the laser focus on a SID4 sensor from Physics, a commercially available wavefront sensor, with higher resolution than a Shack-Hartmann sensor. The magnification was chosen in a way to cover most part of the wavefront sensor. The wavefront distortions are compensated by a deformable mirror that is placed in the beamline after the plasma mirror and operates under an angle of almost 0°. The deformable mirror has a membrane to which actuators are attached. They push and pull on the membrane to deform the mirror surface. A 30 min calibration routine relates the different actuators to the Zernike modes and the wavefront can be optimized in a closed loop setup in low power mode of the laser and with the full aperture beam. Elements that degrade the beam profile and the wavefront were removed for this optimization. When imaging the focal spot with all elements inserted, we therefore observed a slight degradation with respect to the optimized spot.

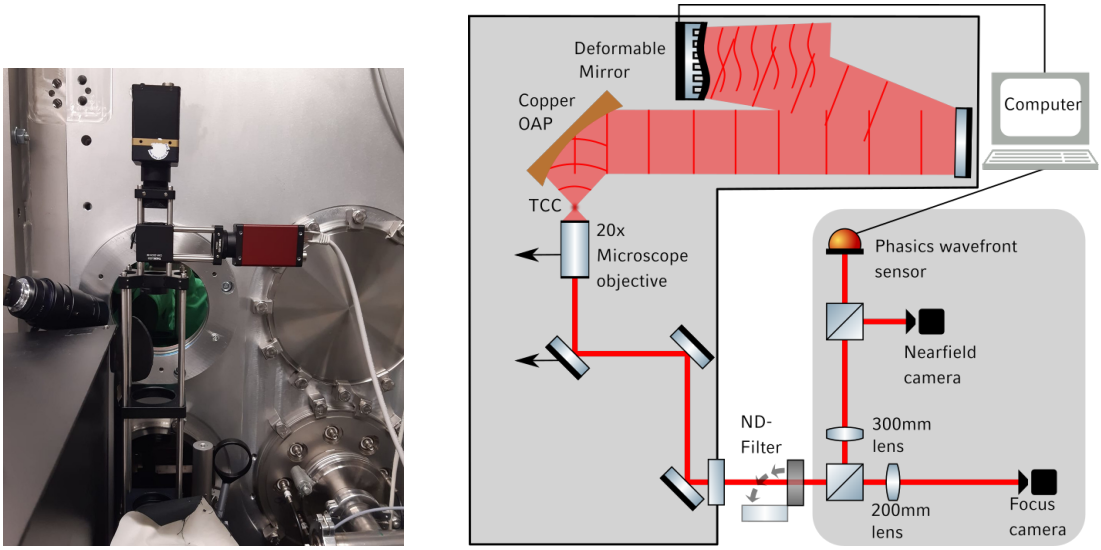

a. *Image of the AO-loop tower* **b.** *Scetch of the optical path*

Fig. 3.21. *| (a) A real life picture of the adaptive optics tower with the Phasics sensor and the nearfield camera. (b) Optical Setup for the focus diagnostics and the Adaptive optics loop. The focus camera is placed in the focus of the* 200 mm *lens. The Phasics sensor was moved along the optical axis such that the chip size of the sensor is at approx. 80% illuminated. From the geometry we estimate imaging a plane* 10 m *upstream in the laser chain, and the adaptive mirror is placed roughly 10 m downstream. The nearfield camera is positioned to image the plane in the OAP. The microscope objective was moved in a save position during full power shot.*

3.4.5. Spatial intensity distribution

The AO compensates phase distortions due to inhomogeneities with size >cm. The distribution of energy in the focal plane is therefore not as concentrated as one would expect from the Fourier transform of the laser near field profile. Smaller imperfections, and in particular micro-roughness scatters light in large angles and reduces the energy concentrated within the central spot.
The spatial shape of the laser focus is measured with a microscope setup, consisting of a 20 x microscope objective with a 200 mm lens and a Charge Coupled Device (CCD) camera (Allied Vision, Manta G-419 NIR). Fig. 3.21 (b) shows the microscope setup as implemented to image the focal plane of the laser pulse. The magnification of 19 was determined, by moving an isolated particle transverse to the laser beam, with a calibrated motorized stage.
For the focus measurement the laser pulse is attenuated until the central, high intensity part of the laser is not over exposed in the image. By reducing the attenuation, i.e. increasing the fluence on the camera, and over exposing the central part, the low energetic wings of the pulse become visible. Stacking multiple images with different attenuation levels on top of each other yields a High Dynamic Range (HDR) image of the energy distribution in focus. We generate the HDR images by starting from the low energy pedestal and replacing saturated pixels in that image with the upscaled pixel values from the next image with stronger filtering. The scaling factor is found by the sum over all saturated pixel in the saturated image and then finding the pixel value in the stronger filtered image, where the same number of pixels is above this value. The up-scaled upper image then replaces the values of saturated pixels to generate the HDR image.
An image of the energy distribution in focus normalized to the maximum is shown in Fig. 3.22. Equating the integral over this distribution with laser energy yields the peak fluence F_0, and considering a Gaussian temporal distribution with FWHM duration 32 fs results in a peak intensity of $2.8 \cdot 10^{20}\,\mathrm{W/cm^2}$ and a normalized laser amplitude of $a_0 = 13$, considerably lower than the ideal $a_0 \simeq 30$, which could theoretically be achieved with these laser parameters.

On a shot to shot basis this procedure could not be performed, as access to the radiation area would have been necessary. For a relative measurement between shots we used Low Dynamic Range (LDR) images, with the strongest filter set-

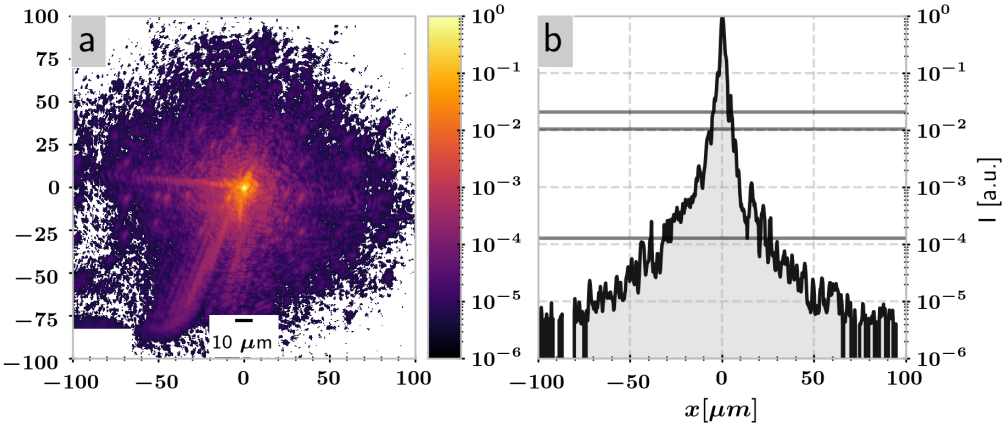

Fig. 3.22. *| HDR focus recorded at the end of the campaign. (a) Shows the normalized 2D intensity distribution with two apparent wings to the lower left. (b) shows a vertical lineout at 0. The horizontal lines denote stacking layers. The area above* 10^{18} *W/cm*^{2} *extends over* $\sim \pm 10 \mu m$

ting such that the central part is not over exposed. Literature reports that the LDR method is likely to over estimate the central intensity by up to a factor of 1.5 [72, 108]. Each image was recorded using a 12 bit camera. Unfortunately, the noise level of the camera reduced the dynamic range of the recorded images to maximum 10 bit, covering 3 orders of magnitude. Restricting the reconstructed HDR image from Fig. 3.22 to the same low dynamic range yields that the same calculation as described above, but on the basis of the LDR image, overestimates the peak intensity by a factor of 1.5, in line with [108]. The FWHM radius of the focus, however, is identical for the LDR and HDR focus evaluation. A summary of the laser parameters is given in Table 3.5

3.4.6. Focus drift

We experienced multiple drifts on various timescales during an experimental day, and therefore optimized the focus before every shot, by moving either one of the beamline mirrors or the parabola. We recorded a LDR focus image prior to every shot, which allowed to monitor the FWHM diameter and the peak intensity over the scope of the beamtime. We estimate the normalized laser amplitude for every shot based on a LDR evaluation method. The resulting peak intensity was down

Table 3.5. *| Summary of Laser parameters*

	HDR
P_0	$4.7 \cdot 10^{13}$ W
Strehl	0.15
I_0	$3.8 \cdot 10^{20}$ W/cm^2
Ideal Int	$2.6 \cdot 10^{21}$ W/cm^2
a_0	13.3
d_{FWHM}	2.1 µm
E_{FWHM}	19.70 %
E/e^2	36.12 %

scaled by a factor 1.5 to compensate for the energy contained in the wings of the laser focus that was evident from the HDR analysis. In a free running mode of the laser, we see a fluctuation of the FWHM area of the focus of up to 15%, which on its own yields a fluctuation in a_0 of $\Delta a_0 = \pm 1$. From the spread in normalized laser amplitudes in Fig. 3.23 we estimate an average $a_0 = 14$, with a typical standard deviation of 2, which is consistent with the focus evaluation in the of HDR images.

3.4.7. Main Beam Attenuation

For the measurements at JETi 200 we used two attenuation approaches. Two mirrors can move into the laser chain before the main amplifier and direct the beam on an additional detour via low reflective mirrors, reducing the beam energy by 3 orders of magnitude. This attenuator was used for the measurement of the temporal laser contrast, the coarse alignment of the target and the adaptive optics loop to optimize the laser focus.
For experiments with microspheres the lateral overlap with the focus is crucial. To ensure that the attenuated pulse and full energy pulse overlap perfectly, we used a different low energy mode of the laser for adjusting the focus position. The beam energy was reduced by switching off pump lasers in the front end amplifiers, such that the intensity on the plasma mirror was below the substrate's damage threshold and, due to its low reflectivity, yielded a similar energy reduction as the attenuator. This allowed overlapping the laser with the target, without

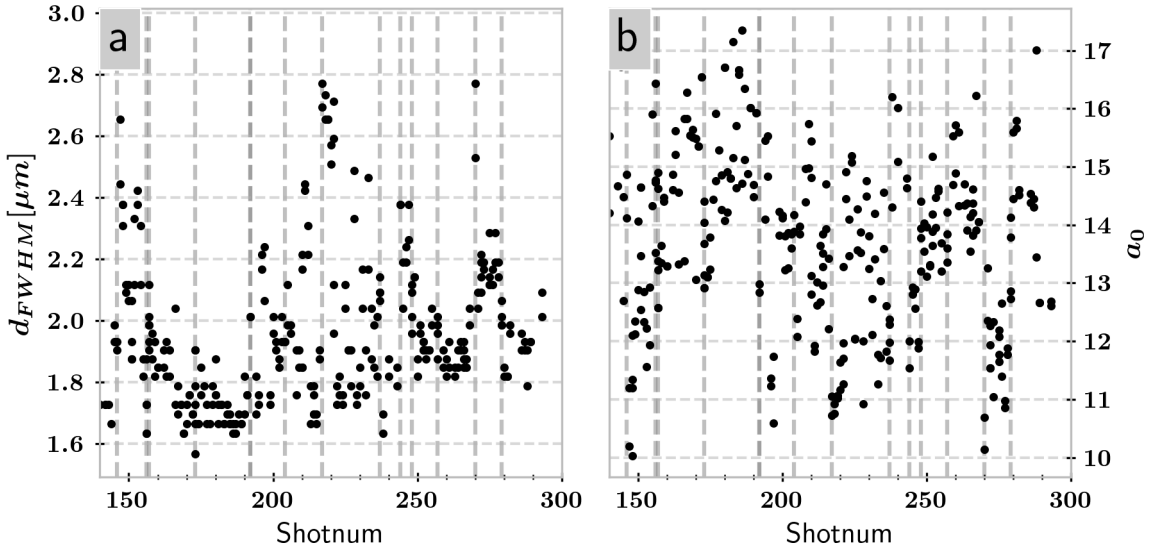

Fig. 3.23. *| Vertical lines denote different days. The shot to shot fluctuations represent the uncertainty in peak intensity estimation. (a) FWHM diameter of the focus spot. (b) Estimated peak intensity. The energy contained in A_{FWHM} was downscaled by 1.5 for the LDR focus evaluation applied.*

the necessity of moving parts in the laser chain.

3.4.8. Transmission Diagnostic

Monitoring the transmitted light has proven very useful in experiments with isolated micro targets. An anodized aluminum plate placed 525 mm downstream the laser focus served as a scatter screen for the transmitted light. The camera viewed this screen under an angle of 45° vertical and 0° horizontal with respect to the laser propagation direction (Fig. 3.24). The viewing angle was calibrated by the iWASP inlet slit on the transmission screen, which has a dimension of 600×10 mm. The images were scaled by $\sqrt{2}$ in the vertical direction as a compensation for the 45° angle. Fig. 3.25 shows several permanent features of the transmitted beam profile: the inlet slit for the iWASP, the shadow of the pic-off mirror and in this shadow the prepulse, clips introduced by the laser beam line and the plasma mirror. The images are recorded using a AlliedVison Manta G-419 NIR camera, with an analog bit depth of 12 bit. The camera was filtered such that the images were not overexposed and after post-processing a bit depth of approx. 9 bits remained. From

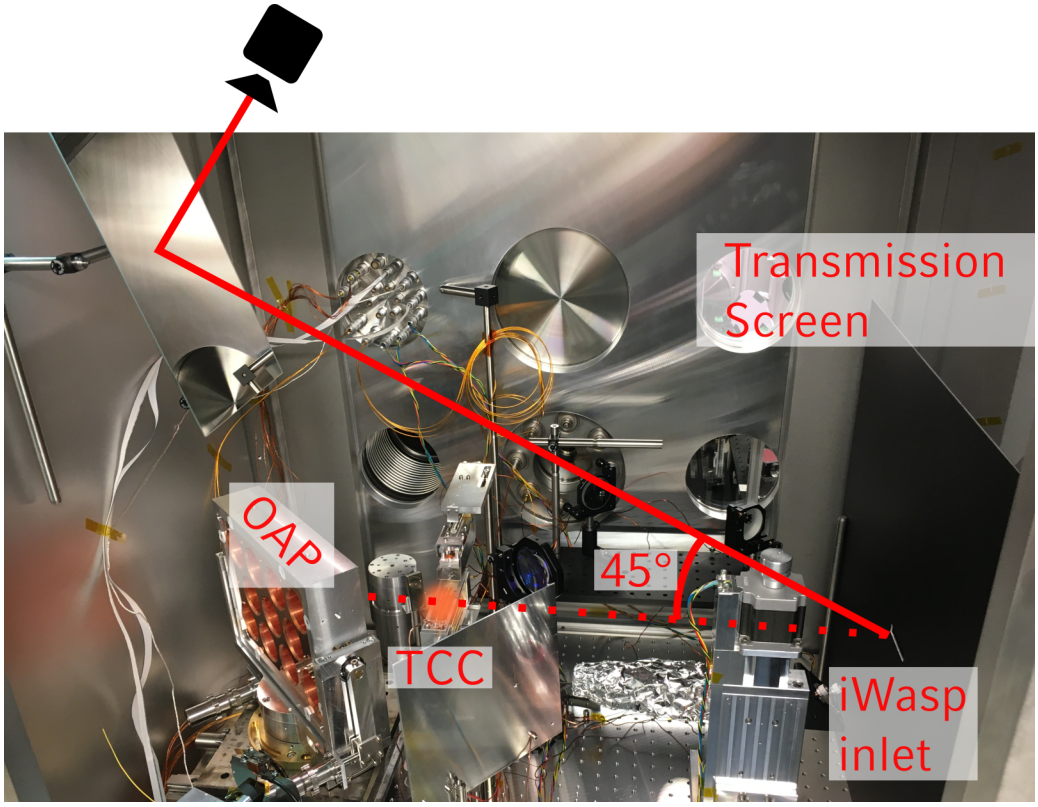

Fig. 3.24. *| Viewing angle of the transmission camera. Distance between TCC and transmission screen is 525 mm.*

each image a background image, which is the average of 20 dark images, was subtracted. After background subtraction, a dynamic threshold was applied on each image separately such that the integral over the background subtracted image[1] did not change.

We applied a mask on every image for separating the permanent features and the area outside the beam cone from the light within the beam cone, Fig. 3.26. Additionally the mask eliminates other stray-light outside the beam. The mask had to be adjusted for every shot separately to compensate for the slightly shifted beam pointing from day to day. The mask was overlapped by matching some of the prominent features such as clips in the beam. The overall shape of the mask was kept unchanged.

Fig. 3.26 shows two example beam profiles with a target (a) and without (b). The

[1]This image contains negative values. We search for the positive value, where the sum of all positive pixel counts smaller than this value is the sum of the negative pixel counts

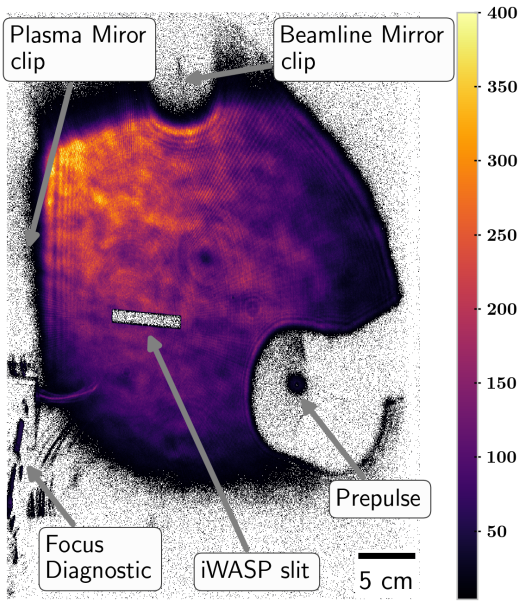

Fig. 3.25. *| The pulse had serveral features. Some of which were intended, as the hole in created by the pick-off mirrors for the pre-pulse. Others were a result of the target area not being fully commissioned (i.e. clips from the plasma mirror and the beamline or the uneven beamprofile).*

integral over the masked areas is a measure for the energy in the beam cone and interpreted as "unperturbed" light which interacted little with the target. For reference shots without target, the integral serves as a measure of the pulse energy, which we calibrated to the total pulse energy arriving in the chamber, as explained in Section 3.4.2. We have recorded multiple empty shots distributed over the course of the experiment, which allowed monitoring the laser performance on a day to day basis. For shots on target the intensity of the integral is reduced. The amount of transmitted light is estimated as the ratio of the integral over the masked area for the shot on target and a reference shot recorded in due time but at least on the same day,

$$T = \frac{\sum \text{count(on target)}}{\sum \text{count(empty)}}. \tag{3.20}$$

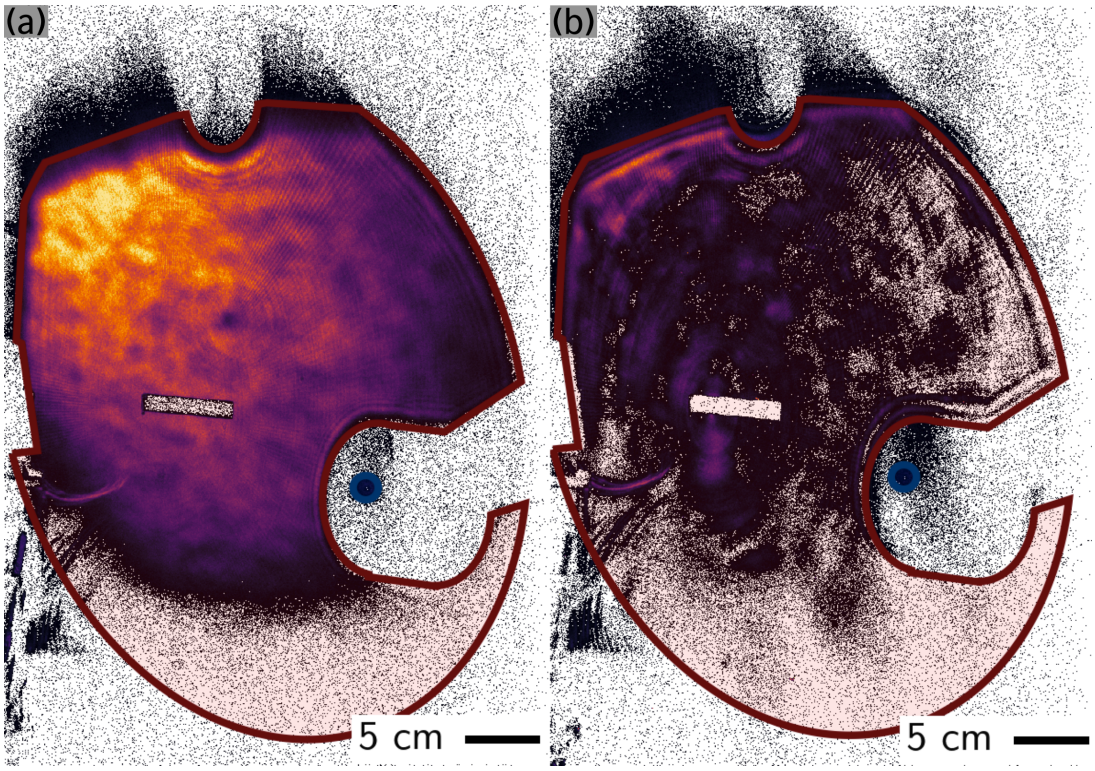

Fig. 3.26. *| Transmission image of an empty shot, 220 (a) and shot on target, 207 (b) including the masks for the prepulse (blue) and the main pulse (red). Colorscale is the same as in Fig. 3.25*

3.4.9. Laser Pointing and Hit-statistics

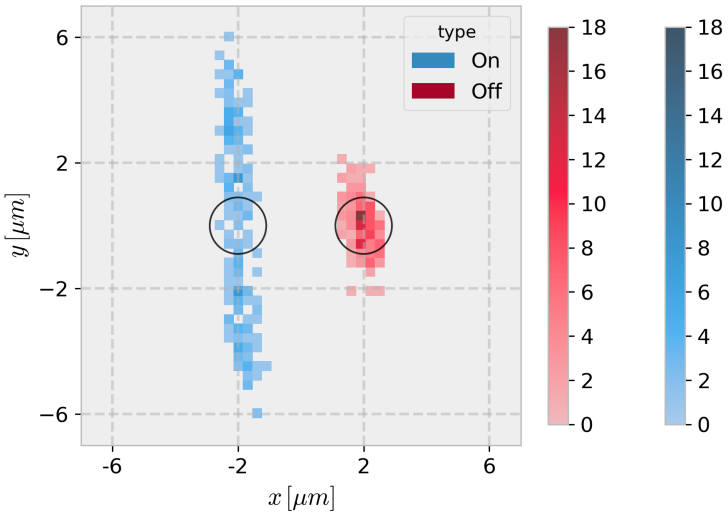

Fig. 3.27. *| Focus jitter of the JETi 200 with the cryogenic pump turned on (blue dots) and turned off (red dots), consisting of 200 shots each. The color map indicates count rates. The focus jitter of the JETi 200 laser is mainly along the vertical axis. Especially the cryogenic pump is a major source of vibrations. Black circles indicate the FWHM area of a* 2 µm *laser focus. The two measurements are shifted latterly by* 4 µm *for clear visibility.*

There are numerous sources for pointing variations such as building vibrations, vibrations of individual optics, construction sites or profile and phase distortions of the pump lasers in the laser chain. In the case of the JETi 200 laser the cryogenic pump, cooling the crystal of the main amplifier, was identified as a major source causing a periodic vertical motion of the laser focus, with an amplitude of up to ±6 µm, see Fig. 3.27. The probability to hit a non moving 1 µm sphere with at least 50% of the maximum intensity is about 12% in this situation.
The jitter was significantly reduced by turning off the cryogenic pump during alignment of the particle and the full power shot. This could only be done for a short period and had to be done with great care, as the crystal could suffer from irreversible damage when not sufficiently cooled during operation. In addition a big temperature gradient in the amplifier crystal results in wavefront distortions and can change the focusability of the laser pulse. After a decay time of 15 s un-

Table 3.6. *| Shot statistics and hit rates for spherical targets*

1 µm spheres	2 µm spheres	7 µm spheres	Foil shots	empty Shots
50/98 (51%)	20/24 (83%)	3/3 (100%)	10	8

til the cryogenic pump stood still, the amplitude of the spot motion reduced to ± 2 µm peak. The above defined hit probability increased from 12% to about 72%. Finally considering the residual motion of the particle, with amplitude of the order of ± 4 µm, we expected a probability of $\sim$ 10% for hitting with 50% of peak intensity. Of course the hit probability increases with larger sphere diameter, either by increasing the initial diameter of the sphere, or by pre-expanding the sphere.

We define a hit as a shot, where energetic protons with energies exceeding 2.6 MeV could be detected. This includes gracing shots as well as more central hits. This study contains a total of 125 shots on levitating spheres. 82 of these shots yielded ion data, in line with a hit rate over the whole campaign of 65%. Table 3.6 summarizes the shot statistic over the course of a many weeks campaign. We can see that the hit rate increases for larger spheres as expected. We also experienced an increased hit rate for pre-expanded 1 µm spheres as compared to non-expanded 1 µm spheres.

3.4.10. Equivalent Radius data-sorting

The focus and particle jitter and the observed drift of the pre-pulse energy resulted in a variety of pre-expansion conditions. Transmitted beam profile analysis (Section 3.4.8) served as a measure for ordering the experimental results.
We apply a simple model, assuming that the laser light is blocked in regions, where $n_e > n_c$ and transmitted otherwise. We consider this a good estimate, as the intensity rapidly decreases in regions away from the laser axis. We assume a spherically symmetric Gaussian density distribution and associate a blocking disk with radius r_c to each shot, that blocks the main pulse.
The transverse laser profile is approximated by a radial Gaussian distribution over 2.5 orders of magnitude, to relate the calculation of blocked energy to the integral over the recorded transmission images with a similar dynamic range. The focus diameter is $d_{FWHM} = (2 \pm 0.2)$ µm, which is the FWHM focus obtained from the

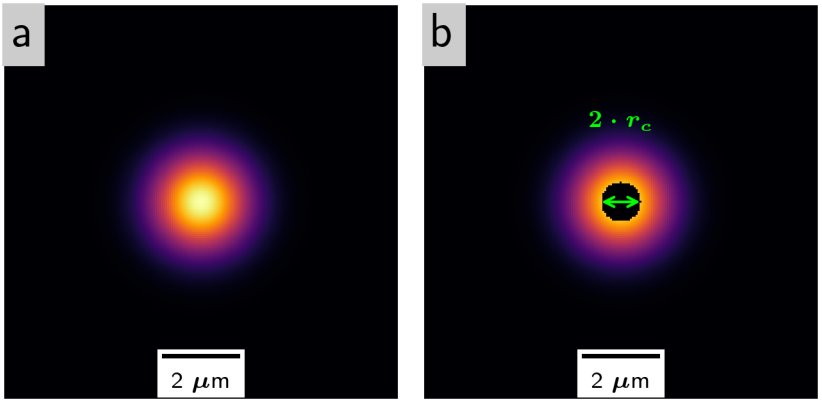

Fig. 3.28. *(a) Initial Gaussian beam, as the reference with a* $r_{FWHM} = 2\,\mu m$. *(b) Central part blocked by a* $1\,\mu m$ *sphere, amounting to a* $r_c = 0.5\,\mu m$, *corresponding to a transmission of* 85%.

HDR focus image. The target is modeled as simple disk over-laid on the laser focus, that is removing the central area, as shown in Fig. 3.28. The fraction of sum of Fig. 3.28 (b) and the sum of Fig. 3.28 (a), gives the ratio of transmitted light. For each shot the size of the central screen is varied such that the fraction equals the fraction of transmitted light in the experiment and the corresponding radius is allocated as r_c to the respective shot. Note, that this is not a unique definition because we assume that the respective shot was a central hit. If a shot has been a non cental hit, the actual blocking radius would be bigger than the one assigned by our method, as such a combination would lead to the same amount of transmitted light.

The disk radius can serve as a crude estimate for the initial target central density and the extent of plasma under the assumption of Gaussian density distribution with constant particle number defined by the initial sphere radius and particle density. Starting from a fully ionized solid density sphere with an electron density of $n_s = 195$, the target is redistributed to form a Gaussian distribution of the form

$$n_e = n_0 \cdot \mathrm{e}^{-(r/\sigma_r)^2}, \tag{3.21}$$

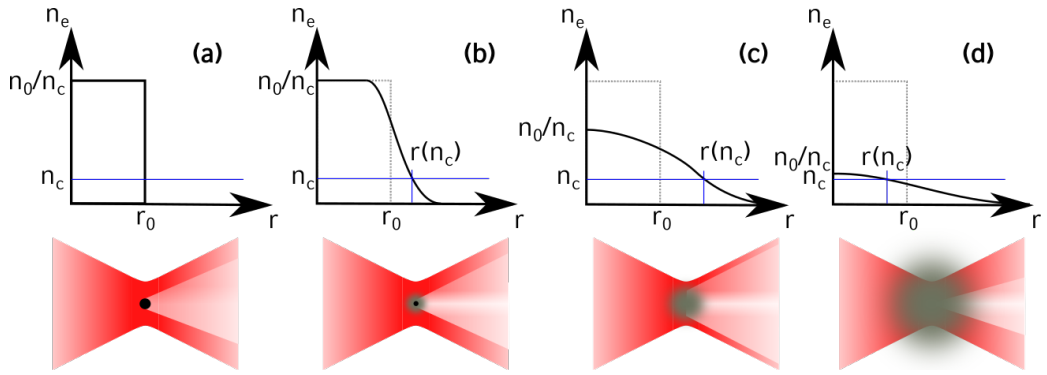

Fig. 3.29. *| Blocking radius of spheres with different pre-expansions at the main pulse arrival. A density above n_c are considered to completely block the light. For a solid density sphere (a) this is given by the target radius. For an expanding sphere, the vacuum target boundary fades, and the blocking radius moves outwards (b,c). For big pre-expansions, the target radius decreases until it finally reaches zero (d). The bottom row illustrates the impact on the transmitted light.*

where r is the radius of a spherically symmetric Gaussian distribution and n_0 is the central density. The plasma scale length is

$$\sigma_r = \left(\frac{4}{3} \cdot \frac{1}{\pi^{1/2}} \cdot \frac{n_0}{n_s} \right)^{1/3}, \tag{3.22}$$

defined by particle number conservation of the particles in the initial solid density sphere. Using Eq. (3.21) and Eq. (3.22), we can calculate the block radius r_c , where the density $n_e = n_c$,

$$r_c = \left(\frac{n_0}{n_s} \right)^{1/2} \cdot \sigma_r. \tag{3.23}$$

We refer to this quantity as ordering parameter r_c . Fig. 3.29 illustrates the situation. For a solid density sphere, the critical density is surpassed at the sharp vacuum target boundary. In this case r_c equals the initial target radius. For a slightly expanded target, the target-vacuum boundary is fading and r_c increases. We assume that the central core stays unperturbed at $195\, n_c$, in the early time of expansion when r_c increases. This is indicated by the horizontal line at $195\, n_c$ in Fig. 3.30, and the central density remains constant for all radii $r_c < 1.0\,\mu\text{m}$. Beyond that radius, the central density starts decreasing with increasing r_c , see Fig. 3.29 (c).

When the central density drops near the critical density, r_c decreases again, and goes to zero when $n_0 \leq n_c$, Fig. 3.29 (d). It is therefore clear that there exists a maximum critical radius r_c . For the initially 1 µm sphere this maximum radius is $r_c = 2.0\,\mu m$ and it is reached, when the central density is $n_0/n_c = 4.5$. Similar numbers can be found for the 2 µm sphere case.
In our example of the 1 µm sphere ($r_0 = 0.5\,\mu m$), the core density drops from $195\,n_c$ to $4.5\,n_c$, when the radius increases from $r_c = 1\,\mu m$ to $r_c = 2\,\mu m$, and this corresponds to a drop of the transmitted light from 51% to 8%. This interval, where $r_c/r_0 > 2$ is referred to as the reduced density interval. This is only true

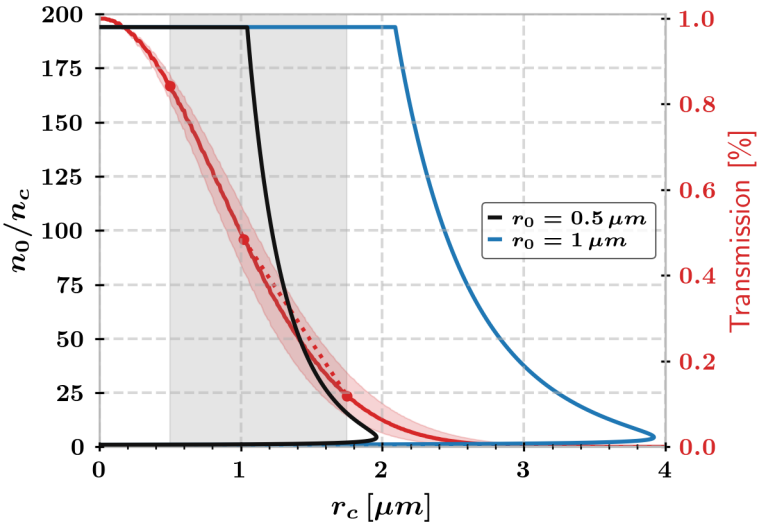

Fig. 3.30. *| Relation between the disk radius and the corresponding central density for a sphere with* 1 µm *and* 2 µm *in diameter. Additionally, the fraction of blocked light is shown. The gray area indicates the range of r_c covered in our experiment and the corresponding estimate of the density regime. The red dots indicate the transmission of a solid density sphere with $r_0 = 0.5\,\mu m$, the onset of central density reduction and the point of highest r_c in our experiment. In the region with reduced central density, the transmission is almost linear with the blocked light.*

for central hits though. In case of a grazing shot less light is blocked. These shots are therefore likely associated with a too small r_c . Also, the focus diameter over the beam-time varied by $2.0 \pm 0.2\,\mu m$ over the course of the study. The red shaded area in Fig. 3.30, reflects this uncertainty. The uncertainty grows in the steep region of the black curve. For example a transmission of 25% (75% blocked) gives an disk radius of $r_c = 1.4 \pm 0.14$. For the 1 µm sphere this results in a core den-

sity between $n_0/n_c = 49^{+31}_{-19}$, if located on the upper branch of the black curve in Fig. 3.30. The ordering parameter hence has some correlation with the central density, but only in this reduced density region and with large uncertainties.
In conclusion, the ordering parameter is a measure of light being blocked by the plasma, and hence marks an upper limit of energy that was involved in the laser plasma interaction. These aspects make r_c a valuable quantity for the classification of the results obtained under varying conditions, as we will see in the following chapter.

Chapter 4

Experiment results

4.1. Foil shots

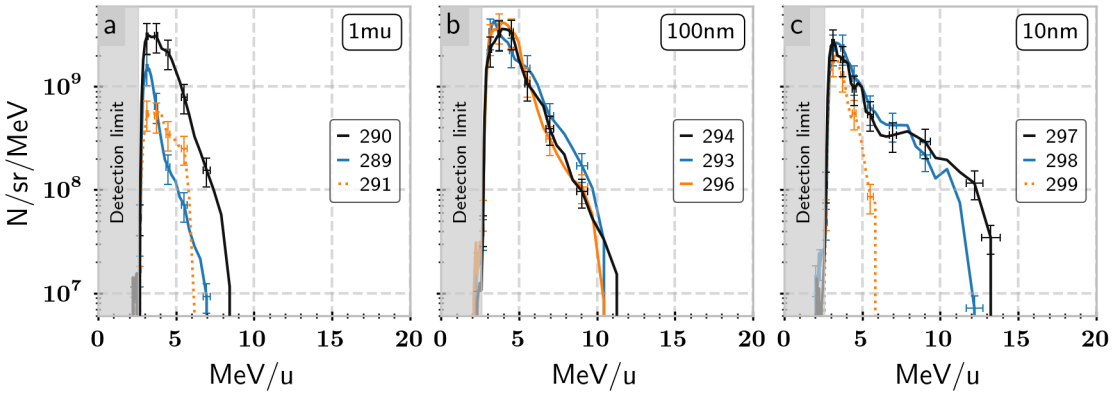

Fig. 4.1. *| Proton spectra of shots on foils. Shot 291 was performed with a* 1.8 ns *prepulse. Shot 299 was on a random position of the plasma mirror with potentially degraded performance. Black lines represent shots with the highest integrated beam energy.*

Here we report on plastic foil shots of thickness 1 µm, 100 nm and 10 nm as benchmark for laser-ion acceleration with the established setup. The laser pulse in these shots had a pulse duration of $\tau_{FWHM} = 32$ fs, and contained the energy of $E \simeq 1.4$ J. The FWHM focus diameter was 2 µm. In Section 3.4.5 we estimated that approx. 30% of the laser energy is contained in the laser focus, which yields a peak intensity of $3 \cdot 10^{20}\, W/cm^2$, corresponding to a normalized laser amplitude of $a_0 \simeq 12$. The foil shots produced the well known exponential decaying proton energy distributions. The maximum energy for protons increases from 8.4 ± 0.3 MeV

Table 4.1. *| Summary of basic spectrum parameters for the comparison foil shots.*

		E_{max} [MeV]	N [1/sr]
1 µm	289	7.0	$1.6 \cdot 10^9$
	290	8.4	$7.5 \cdot 10^9$
	291	6.2	$1.4 \cdot 10^9$
100 nm	293	10.4	$1.0 \cdot 10^{10}$
	294	11.3	$9.7 \cdot 10^9$
	296	12.3	$1.1 \cdot 10^{10}$
10 nm	298	12.2	$6.9 \cdot 10^9$
	297	13.2	$6.5 \cdot 10^9$
	299	5.8	$2.7 \cdot 10^9$

for 1 µm foils up to 13.2 ± 0.6 MeV for thinner, 10 nm and 100 nm foils, what equals 9.4 ± 1 MeV/J laser energy. Especially for the 10 nm foil shots, the high energy tail deviates from the exponential decaying shape as for the thicker foils. This effect is known for thin foils as an enhanced TNSA mechanism, attributed to relativistic induced transparency or break out after burner (BOA), [17, 109, 110], which leads to stronger volumetric heating of the target. We did not observe carbon ions for the foil shots. When introducing the pre-pulse at -1.8 ns the maximum cut-off energy from 1 µm foil thickness reduced to 6.2 ± 0.2 MeV (dashed orange spectrum in Fig. 4.1 (a)). No ions were observed for the 100 nm and the 10 nm foils, when using the pre-pulse. For the last shot on 10 nm we moved the plasma mirror substrate to a spot with increased reflectivity. The reduced laser contrast again resulted in a lower cut-off energy of 5.8 ± 0.2 MeV as well as in reduced particle numbers for this shot, (dashed orange spectrum in Fig. 4.1 (c)). Table 4.1 summarizes the most relevant parameters from these benchmark shots. The results show that the experiment design is adequate to enable proton acceleration from foils as thin as 10 nm and therefore proves that contrast improvement through the plasma mirror functioned as expected. In particular, the artificially introduced pre-pulse dominates the pre-expansion.

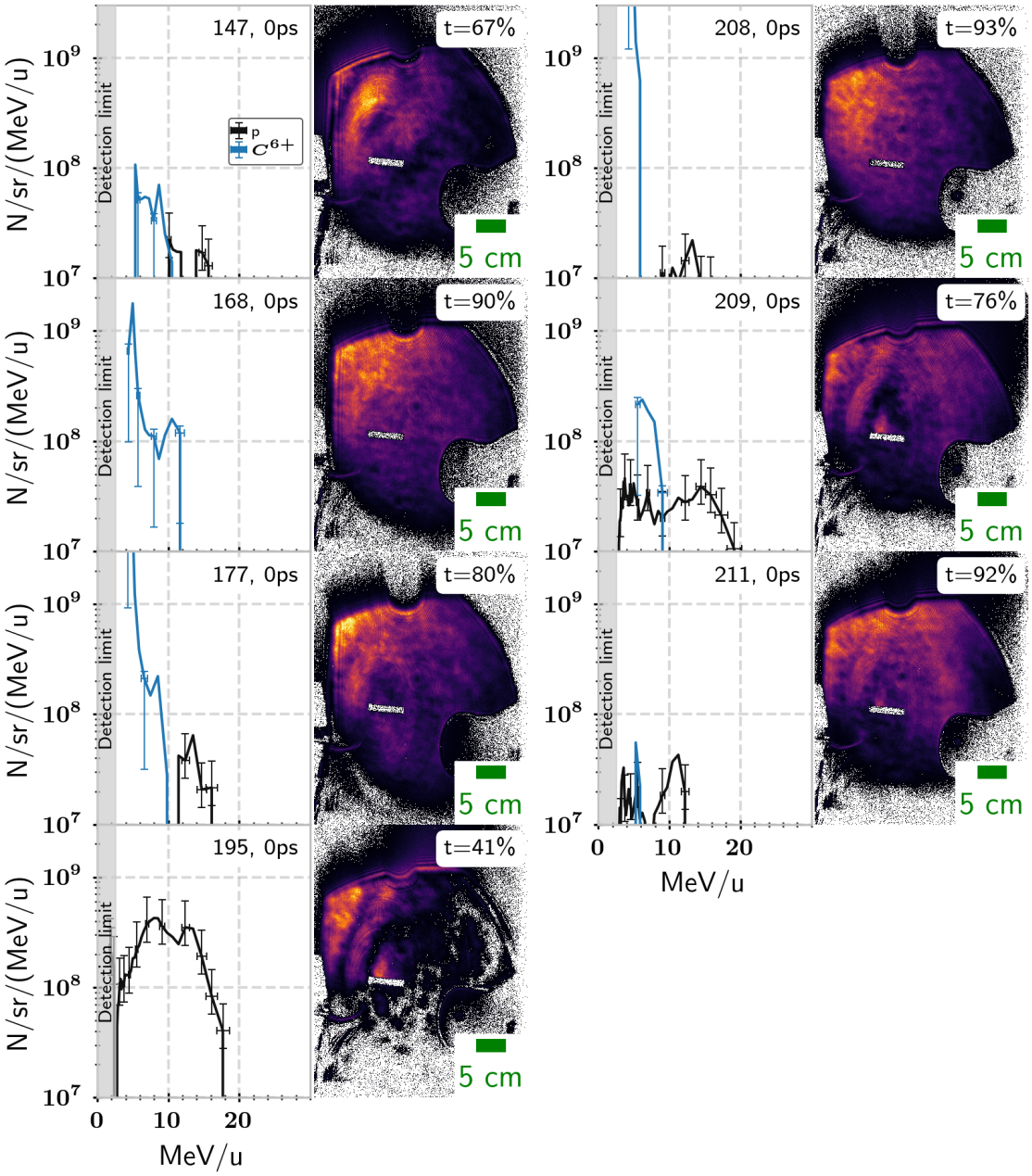

Fig. 4.2. *| Recorded ion spectra and the corresponding transmitted beam profiles for laser shots without a pre-pulse. Colormap in arbitary units.*

4.2. Spherical targets

We have recorded multiple shots per setting to compensate for fluctuations in positions of the laser focal spot and the target. For 1 µm non-expanded spheres we recorded data on five different experiment days, with slightly different laser performance. The spectra and transmitted beam profiles are shown in Fig. 4.2. The hit quality of a particle can be related to the transmission camera, where less transmitted light means a better hit than high transmission. The amount of transmitted light for these non-expanded shots varies from 41% (195) up to 93% (208) and the maximum proton energy varies from no protons being detected up to (19 ± 1) MeV energy. A similar observation is made for the maximum carbon energies, where we find the highest energies for shot 168 with (11 ± 0.7) MeV/u.
In this subset, we recorded one shot (168), where only carbon ions were detected. Four shots (177, 208, 209, 211) show comparable particle numbers, but different spectral distribution of protons. No obvious relation between e.g. maximum proton energy and the amount of transmitted light is observed.
Shot 195 stands out as it shows an order of magnitude higher proton numbers compared to the other shots, $4.1 \cdot 10^{10}\,\mathrm{sr}^{-1}$, as e.g. 209 with the second largest proton number, with $1.7 \cdot 10^{9}\,\mathrm{sr}^{-1}$, and the highest proton energy. Comparing the transmission of 41%, with the expected transmission for a 1 µm sphere from Fig. 3.30, which is of the order of 80%, shows that this shot blocks more light than one would naively expect from a 1 µm sphere. As we will see later, the reasons for the reduced transmission is likely due to significant expansion before the main pulse interaction, i.e the sphere was in fact pre-expanded unintentional by e.g. using a bad spot on the plasma mirror.
For each delay setting we select a representative best shot, as the one that yielded the highest proton energy. For non-expanded spheres this is shot 209. It produced a non-monotonic proton energy distribution, ranging from the detection limit of 2.6 MeV up to the energy of (19 ± 1) MeV. Carbon ions extent from the detection limit of 4.6 MeV/u up to (9 ± 0.4) MeV/u. The proton spectrum is slightly lowered in this energy range.
Fig. 4.3 presents example proton and carbon spectra as well as transmission images for two different delay settings of the prepulse. The left column corresponds to with a pre-pulse delay of -230 ps and a pre-pulse energy of 650 µJ, yielding a

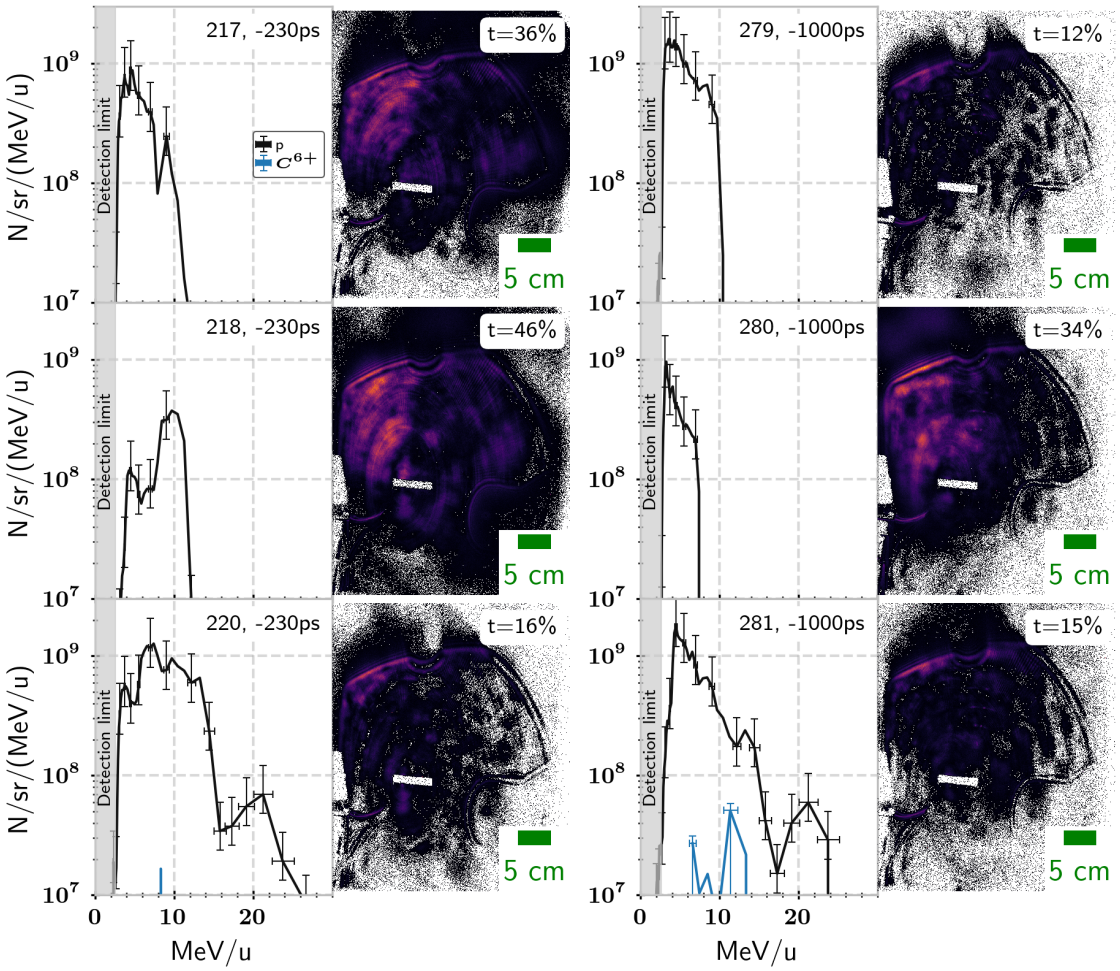

Fig. 4.3. *| Recorded ion spectra and the corresponding transmitted beam profiles for laser shots with a pre-pulse at* $-230\,\mathrm{ps}$ *and* $-1000\,\mathrm{ps}$*. Colorbar in arbitary units. The spectra in the bottom row are very similar, despite the very different delay setting.*

peak pre-pulse intensity of $5 \cdot 10^{15}\,\mathrm{W/cm^2}$. The right column represents shots with a delay of $-1000\,\mathrm{ps}$ recorded towards the end of the beam time, with a pre-pulse energy of $200\,\mu\mathrm{J}$ and a peak pre-pulse intensity of $1.6 \cdot 10^{15}\,\mathrm{W/cm^2}$. The similar ion spectra for different combinations of pre-pulse intensity and expansion time, leads to the assumption, that similar plasma conditions were present at the time of main pulse interaction. This means that the reduced pre-pulse intensity reduced the expansion speed such that a 4 times larger expansion time resulted in similar conditions. As for the previously mentioned non-expanded spheres also these shots show a large variation. For shots with a delay of -230 ps, the maximum proton energy varies between $13.2 \pm 0.6\,\mathrm{MeV}$ (shot 217) and $27 \pm 2\,\mathrm{MeV}$ (shot 220). Similar for -1000 ps shots, with a maximum proton energy of $7.4 \pm 0.3\,\mathrm{MeV}$ (shot 280) for the worst shot and $24 \pm 2\,\mathrm{MeV}$ (shot 281) for the best shot with that delay. For the shots with high proton energies the transmitted light is as low as 15%. In this set, shot 279 has a transmission comparable to shots 220 and 281, but only yields a maximum proton energy of $10.5 \pm 0.4\,\mathrm{MeV}$.

4.2.1. Non Expanded Targets

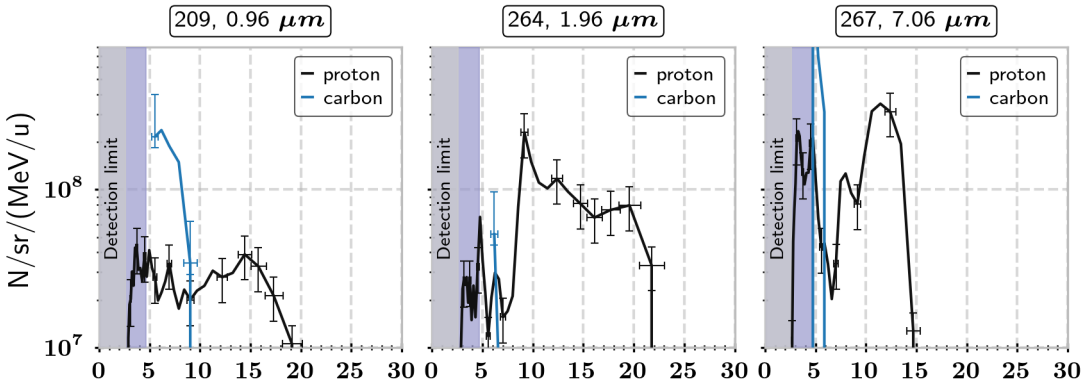

Fig. 4.4. *| Spherical target shots without a pre-pulse for* 1 µm *,* 2 µm *and* 7 µm *target diameters. The blue area marks the detection limit for the carbon ions.*

For non-expanded targets, the number of protons increases with target radius from $4.8 \cdot 10^8\,\mathrm{N/MeV/sr}$ for a 1 µm sphere to $1.5 \cdot 10^9\,\mathrm{N/MeV/sr}$ for a 2 µm up to $2.1 \cdot 10^9\,\mathrm{N/MeV/sr}$ protons for a 7 µm sphere. Even though the detected particle

number increases, the fraction of particles one would expect from isotropic expansion in 4π decreases with increasing particle radius. This equals a decrease in the amount of protons being accelerated forward, from 1.8×10^{-3} over 5.2×10^{-4} for a 2 µm sphere to 1.80×10^{-5} for a 7 µm sphere. The 1 µm shot has a non-decaying proton spectrum reaching up to almost 19.1 ± 1.1 MeV, with carbon ions up to 9.0 ± 0.7 MeV/u. The proton spectrum is mildly modulated, with a slight increase in particle numbers around 15 MeV.
The 2 µm shot extends up to 22 ± 2 MeV in proton energy. Below 8 MeV the proton numbers are lowered to a level of $2 \cdot 10^8$ N/MeV/sr, which is most likely due to co-propagating carbon ions, which reach a maximum energy of 7.9 ± 0.6 MeV/u. At 8 MeV a peak in the proton spectrum is present and after that the spectrum is almost flat towards the maximum cut-off energy. For the 2 µm spheres we have 4 shots on not expanded spheres, that show very comparable results.
For the 7 µm the maximum cut-off energy reaches up to 14.7 ± 0.7 MeV and the carbon ions have a maximum cut-off energy of 5.9 ± 0.4 MeV/u. At 6 MeV the proton number drops to a level of $2 \cdot 10^7$ N/MeV/sr. Around 12 MeV the proton number peaks at $3 \cdot 10^8$ N/MeV/sr. The ion bunch parameters are summarized in Table 4.2.

Table 4.2. *| Summary of parameters for non-expanded density spheres with different diameter. Selected best shots.*

		H^+		C^{6+}		
		E_{max} [MeV]	N [1/sr]	E_{max} [MeV]	N [1/sr]	Transmission
1 µm	209	19.1	$4.8 \cdot 10^8$	108	$6.8 \cdot 10^8$	85 %
2 µm	264	21.8	$1.5 \cdot 10^9$	94	$4.3 \cdot 10^7$	58 %
7 µm	267	14.7	$2.0 \cdot 10^9$	71	$1.8 \cdot 10^9$	30 %

4.2.2. Ordering parameter and Particle numbers

It is obvious that although we actively varied the parameters (in particular sphere diameter and pre-expansion), the experimental results (energy, ion yield) varied substantially from shot to shot, even without changing the parameters actively.

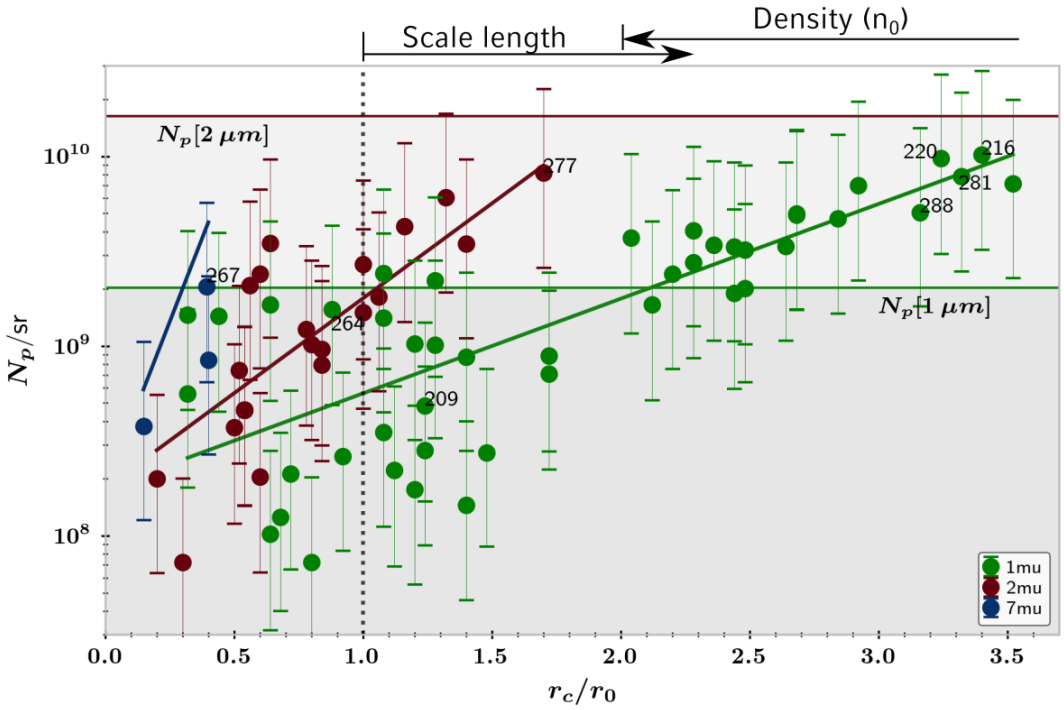

Fig. 4.5. *| Particle numbers versus the ordering parameter over initial sphere radius. Selected shots are marked. 267, 264 and 209 correspond to the best non-expanded shots for each sphere diameter. Additionally we marked shots that yielded the highest particle numbers for* 2 µm *and* 1 µm *spheres.*

The ordering parameter introduced in Section 3.4.10, assigns an effective blocking radius r_c to each shot based on the amount of light that surpassed the target and can be interpreted as the radius of a blocking disk, and hence a measure for the hit quality. A r_c smaller than the initial target radius indicates that the target has not been properly hit. It is also a measure for the pre-expansion of the target.
For each shot we extract the maximum proton energy, the integral over the differential proton spectrum per steradian, and the corresponding ordering parameter. We performed shots on spheres with a diameter of 1 µm (50 shots), 2 µm (20 shots) and 7 µm (3 shots, all without pre-pulse). Fig. 4.5 shows the particle number per steradian, against the normalized ordering parameter r_c/r_0, where r_0 is the initial target radius (0.5, 1.0 and 3.5 µm, respectively), for 1 µm , 2 µm and 7 µm spheres. $r_c/r_0 = 1$ corresponds to a non-expanded sphere, which is indicated by the vertical dashed line. In this graph, we expect $r_c/r_0 < 1$ to be grazing shots, and $r_c/r_0 > 1$ are shots, where the target was pre-expanded. Especially $r_c/r_0 > 2$

represents the reduced density area, as defined in Section 3.4.10. Thus assuming a Gaussian distribution, the central target density n_0 is larger for smaller r_c/r_0, as indicated by the arrow above the graph. The horizontal lines indicate the number of particles one would expect in a solid angle of 1 sr from an isotropic expansion in 4π for a 1 µm sphere ($N_p[1\,\mu m]$) and a 2 µm sphere ($N_p[2\,\mu m]$). For the 7 µm sphere the line is out of the range of this plot and the three shots recorded are well below that limit. We see, that the particle number increases exponentially with the ordering parameter r_c and this supports the validity of the choice. The data crudely follow an exponential scaling,

$$N_p = 10^{8.25} \cdot 10^{r_c} \frac{1}{sr}, \tag{4.1}$$

which is indicated by the blue, red and green solid lines for 7 µm , 2 µm and 1 µm spheres in Fig. 4.5. For the 2 µm spheres (red dots), we see that the data does not extend into the reduced density area of $r_c/r_0 > 2$. Between a non-expanded shot (264) and the shot with the greatest r_c/r_0 (277), the particle number in forward direction increases by a factor of approx. 5.
For the 1 µm spheres (green dots) we see an increased spread in the particle numbers for small r_c/r_0, where particle numbers vary from $7 \cdot 10^7$ /sr to $2.2 \cdot 10^9$ /sr, which is already comparable to isotropic expansion. The spread decreases with increasing r_c/r_0, especially for $r_c/r_0 > 2$. In this region the particle number exceeds the threshold for isotropic emission by a factor of 5 (shot 220 and 216). Comparing the particle number of shot 220 to the best shot without a pre-pulse (209), the particle number increased by a factor 19, indicating a directed beam in the forward direction for pre-expanded spheres.

4.2.3. 1 µm spheres

Fig. 4.6 (a) shows once more the particle numbers per sr for the 1 µm sphere results, Fig. 4.6 (b) shows the corresponding maximum proton energies, also plotted with respect to the normalized order parameter. In the area where $r_c/r_0 \lessapprox 2$ the maximum proton energies vary between (3.2 ± 0.1) MeV and (19.1 ± 1.1) MeV. Even though there seems to be a small gap between shots with $E_{max} < 10$ MeV,

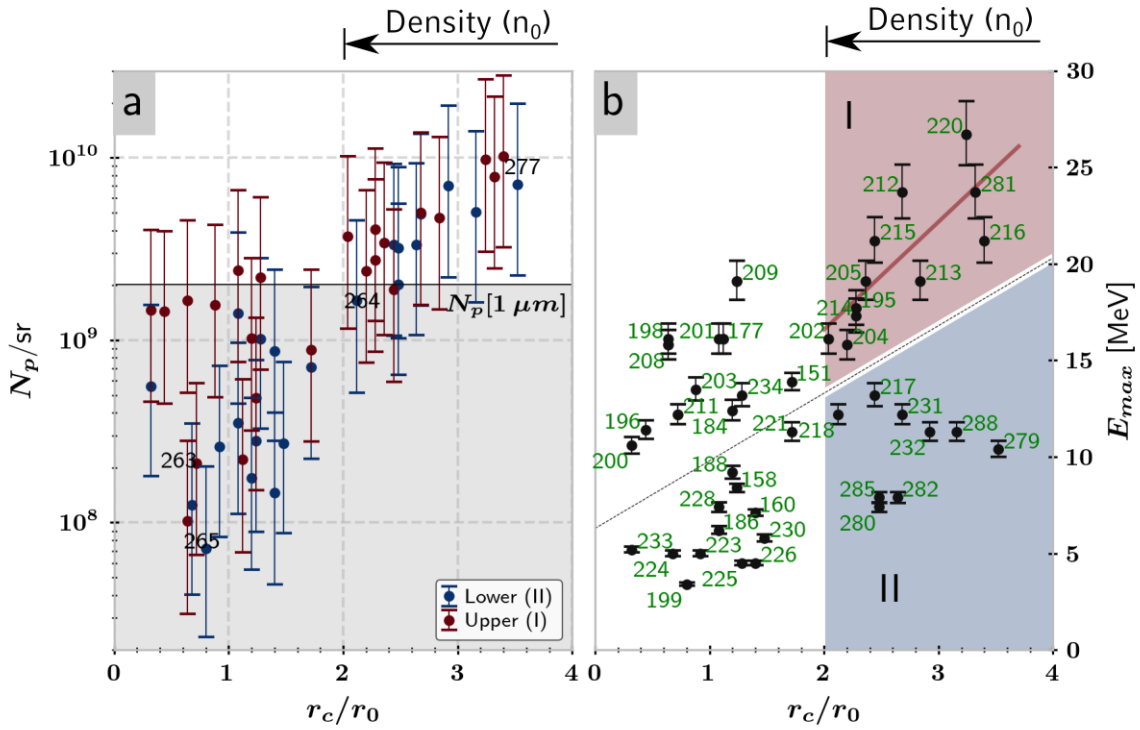

Fig. 4.6. *I (a) Particle number versus normalized ordering parameter. Red and blue color of data points correspond to upper and lower area marked in (b). (b) Maximum energy versus the normalized ordering parameter. For $r_c/r_0 > 2$, two distinct populations of the maximum proton energies emerge.*

and the ones with more than 10 MeV proton energies, there is no clear dependence on r_c/r_0. In the reduced density regime (r_c/r_0>2), two distinct branches emerge. On the lower branch (blue area, marked II), the proton energy does not increase with r_c/r_0. The best shot in this population yielded an energy of (13.0 ± 0.5) MeV at $r_c/_0 = 2.42$, and the maximum energy decreased for increasing r_c/r_0. For all shots that are below the dashed line in Fig. 4.6 (b) we did not observe carbon ions, see Fig. A.1.

In population I, the maximum cut-off energy increases from (16.1 ± 0.8) MeV (202) to (27 ± 2) MeV (220). The linear trend of all shots in the red area yields a scaling factor of 5.6 MeV/(r_c/r_0). In Fig. 3.30, we marked r_c of shot 202 and 216 with red dots and a dashed line on the red transmitted energy curve. The linear line between these to points, indicates that for a 1 µm sphere the energy missing in that interval is approximately linear, meaning that in this area the maximum particle

energy scales approx. with 20 MeV/$J_{blocked}$, considering a 1.4 J laser pulse. Compared to population I, for most of the shots here we also detected carbon ions, see Fig. A.2.

In Fig. 4.6 (a) we re-plotted the particle numbers and color coded the symbols according to their affiliation in plot (b). Here blue means that the shot is located in the lower area (below the dashed line) and red are shots that are above the dashed line. In the reduced density interval ($r_c/r_0 > 2$) the shots are not distinguishable according to their particle number. In the area $r_c/r_0 > 1$, which we interpret mainly as grazing shots, shots with a high proton energy also tend to have an order of magnitude higher particle numbers, as their comparable low proton energy counter parts. All spectra for the shots are shown in the appendix divided by the low energy branch (Fig. A.1) and the high energy branch (Fig. A.2). Selected shots in the reduced density interval will be discussed in further detail in Section 4.2.4.

4.2.4. Selected energy distributions for expanded 1 µm spheres

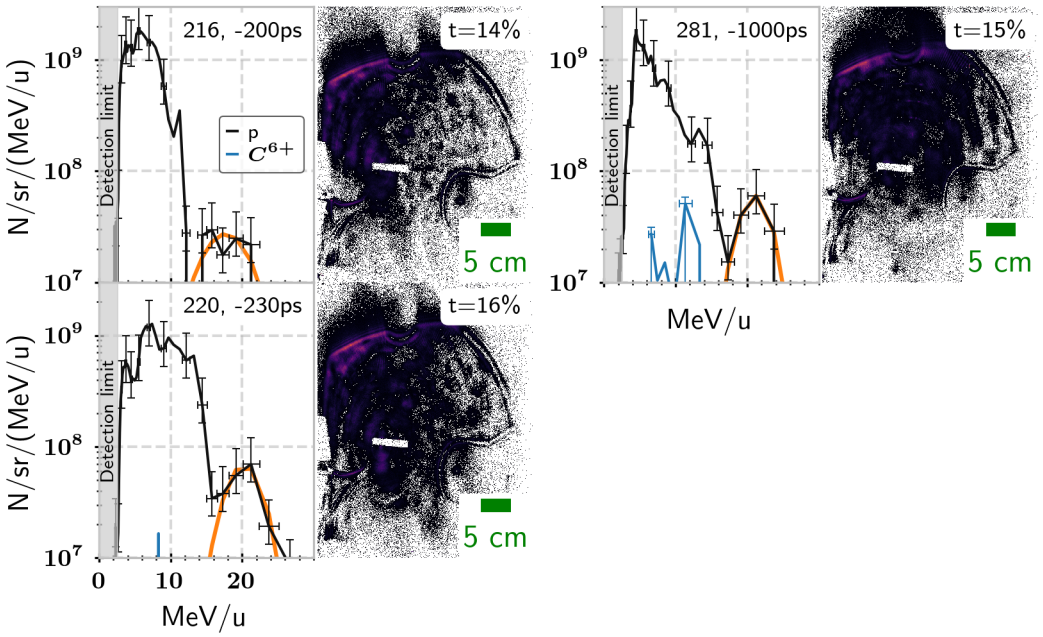

Fig. 4.7. | *Proton and carbon spectra and transmitted beam profiles for three shots that represent the reduced density region (I in Fig. 4.6). The orange curves represent a Gaussian fit to the high energetic part of the proton spectrum.*

Table 4.3. *| Beam parameters of the high energetic parts of the beam with $E_0(proton) >$ 12 MeV. Left fitting parameters of a corresponding Gauss curve. Right part shows the experimental parameters of the high energetic beam.*

	A_0 N/sr	E_0 MeV	σ MeV	N_{bump}	N_{tot}
216	$2.7 \cdot 10^7$	17.8	3.3	$2.2 \cdot 10^8$	$1.0 \cdot 10^9$
220	$6.9 \cdot 10^7$	20.3	2.4	$4.5 \cdot 10^8$	$9.7 \cdot 10^9$
281	$6.0 \cdot 10^7$	21.1	2.2	$3.2 \cdot 10^8$	$7.8 \cdot 10^9$

We select the three shots from population I, that yielded the highest proton energy as the most relevant shots in the reduced density region. Shot 216, 220 and 281 are very similar in terms of maximum proton energy, proton number and the ordering parameter r_c . In all three shots the proton energy exceeds the energy we detected from foil shots by more than a factor of 2, with a maximum proton energy up to (27 ± 2) MeV for the best shot, 220. Fig. 4.7 shows the proton spectrum for the three shots and reveals a strong, low energetic component that extends to 12 to 14 MeV and a weaker high energetic part. For shot 216, the proton number actually drops to the noise level of the detector between 12 MeV and 14 MeV. For shots 220 and 281, the dip is around 15 MeV. From 16 MeV to the maximum proton energy, a maximum around 20 MeV is evident. We can fit a Gaussian function $A * \exp(-(E - E_0)/\sigma)$ to the high energy part, the results of these fits are summarized in Table 4.3. Considering the laser energy on target of 1.45 ± 0.08 J, the maximum proton energy scales with (18 ± 3) MeV/J.
For shot 216 we did not record carbons, and for shot 220 only a weak signal can be identified. Shot 281 shows a carbon spectrum that is peaked between 10 MeV/u and 13.7 MeV/u.

Fig. 4.8 shows spectra of representative shots in region II (221, 225, 285 and 288). Shots 221 and 225 had a pre-pulse intensity comparable to shot 220, and 285, 288 were shot with a reduced pre-pulse intensity, comparable to shot 281. Just comparing these shots to each other, the expansion time was longer as for the respective shots in region I. As explained before, the ordering parameter in these cases (region II) is similar to the cases in region I shown in Fig. 4.7. But there were no carbons observed and the high energy part of the proton spectrum is missing. The low energy part has similar proton yields though.

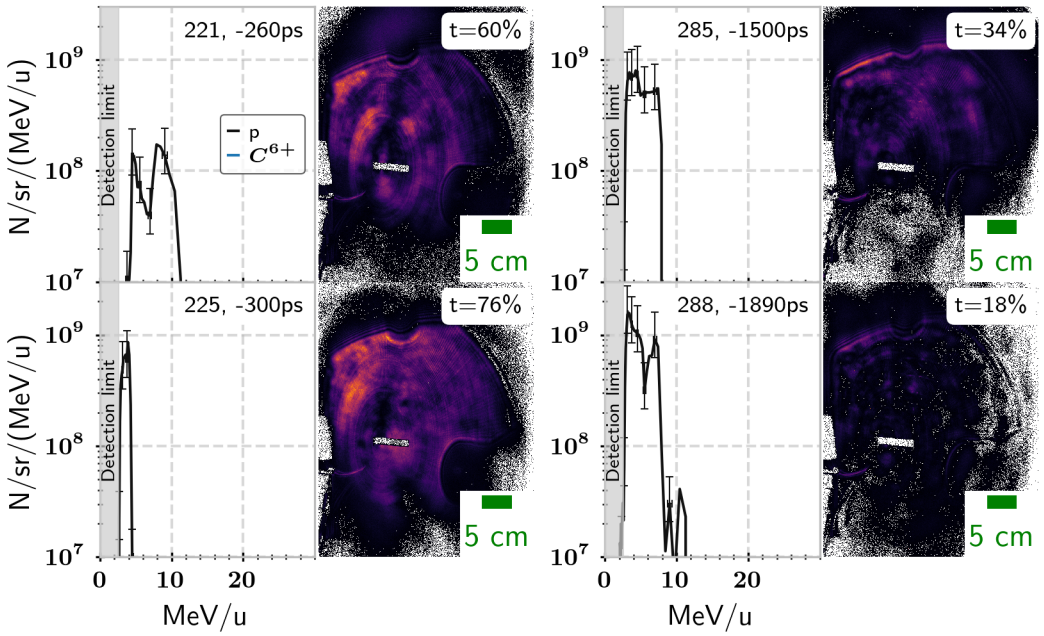

Fig. 4.8. *| Selected spectra and transmitted beam profiles in the under critical density regime.*

Using Fig. 3.30, we can estimate the central density for the respective shots. For shots 220, 281, 216, $r_c \approx 1.7$, results in a central density of the order of $n_c \gtrapprox 10$. With a relativistic critical density of $\gamma n_c \approx 8.5$ for a pulse with $a_0 = 12$, this indicates a target density range that is slightly overcritical. For the shots in population I the central density becomes comparable to the relativistic critical density and the transmission through the plasma becomes more complicated, where the simple model breaks down, and even a crude density estimate can not be stated.

Chapter 5

Particle-in-Cell Simulations

In understanding underlying physical processes, numerical simulations of laser-plasma interaction play a key role. In the field of high-power laser physics, Particle-in-Cell (PIC) [111, 112] simulations are widely used. In contrast to experiments, simulations can deliver time-resolved diagnostics for parameters that are either time integrated, such as the differential energy spectrum or inaccessible during an experiment such as the particle distribution functions and their evolution during the interaction. PIC simulations presented here are optimized to model the laser plasma interaction in a non-collisional regime at relativistic intensities. This requires assumptions on the input parameters, such as peak laser intensity, focus shape and target constitution.
In this section we present 3D3V simulations that were performed with the substantial support by Bin Liu on the JUWELS supercomputer [113], using the SMILEi PIC code [114].

5.1. Simulation setup

The focused laser pulse has a Gaussian intensity profile of the form

$$I = I_0 \exp\left(-\frac{y^2+z^2}{\sigma_L^2}\right) \exp\left(-\frac{(x-x_c)^2}{(c\tau)^2}\right), \tag{5.1}$$

where $\tau = 19\,\text{fs}$ is the pulse length, equivalent to $\tau_{FWHM} = 2\sqrt{\ln(2)} \cdot \tau = 32\,\text{fs}$, a beam waist $\sigma_L = 1.1\,\mu\text{m}$, equivalent to a $d_{FWHM} = 2\sqrt{\ln(2)} \cdot \sigma_L = 1.8\,\mu\text{m}$ spatial focus in the experiment, at a central wavelength of $\lambda = 800\,\text{nm}$. The simulation

spans a 3D domain of $40 \times 20 \times 20\,\mu m$ with $(x, y, z) = 1600 \times 800 \times 800$ cells, resulting in a spatial resolution of $\Delta x \times \Delta y \times \Delta z = 25\,nm$ with $\Delta t = 42\,as$. All boundaries are open for the particles, i.e. macro-particles that leave the simulation box are removed, and absorbing for the electro-magnetic fields. The laser propagates along the positive x direction and is, without specific note, linearly polarized along the y axis. The center of the spherical particle is initialized at $x_c = 80 \cdot c/\omega_L = 400$ cells from the left boundary. Unless specified otherwise, the total energy of the laser pulse is 0.4 J, yielding a normalized laser amplitude of $a_0 = 12$. The laser peak reaches the target center, due to the existence of the plasma slightly after 5100 simulation steps, that is 215 fs after start. In the evaluation, we relate all time stamps to the simulation time step 5100, i.e. negative times mean before the laser peak has reached the target center.

The plasma parameters are derived from a polystyrene sphere C_8H_8 with a radius $r_0 = 0.5\,\mu m$. Polystyrene is a 1:1 mixture of carbon and hydrogen. Assuming full ionization defines the electron density of $n_e = 3.4 \times 10^{23}\,/cm^3 = 195\,n_c$. This corresponds to a total of $1.78 \cdot 10^{11}$ electrons, $2.54 \cdot 10^{10}$ protons and $2.54 \cdot 10^{10}$ carbon 6^+-ions. In the non-expanded case each particle species is represented by 965 macro particles per cell. The initial electron temperature is set to 2 keV. The non-expanded case is resembled by a step function with a sharp vacuum target boundary and a density of $195\,n_c$. The pre-expanded cases are modeled with a truncated spherically symmetric Gaussian profile,

$$n_e = \begin{cases} n_0 \cdot \exp\left(-\frac{x^2+y^2+z^2}{\sigma_r^2}\right) & (x^2+y^2+z^2)^{1/2} < 6 \cdot \sigma_r \\ 0 & (x^2+y^2+z^2)^{1/2} > 6 \cdot \sigma_r \end{cases} \tag{5.2}$$

with maximum initial central densities n_0. The plasma scale length $\sigma_r = (4/3 \cdot 1/\pi^{1/2} \cdot 195/n_0)^{1/3} \cdot r_0$, is given by particle number conservation from a non-expanded sphere. The particles are represented by macro-particles, where macro-particles per cell are also distributed according to Eq. (5.2), with $n_0 = 50$ particles. At a position $x = 200 \cdot c/\omega_L = 1000$ downstream of the laser a screen diagnostics is positioned. This generates an integrated, angular resolved differential energy spectrum of protons and carbon atoms, already converted from macro-particles to real particle numbers. It has been checked that at this position the acceleration process is over and no significant changes to the energy distribution have been ob-

served beyond that point for most cases. The final spectrum can be obtained after the simulation has finished, i.e at 1273 fs. We generate the particle spectra within a cone angle of $\theta < 0.1$ rad in the forward direction, to compare the data from simulation with differential spectra recorded in the spectrometer of the experiment. The simulated spectra are normalized to 1 sr by scaling the particle numbers with $\pi / \tan(0.1)^2$.
Around the laser peak we take snapshots, every 75 simulation steps, corresponding to $\delta t = 3.2$ fs. After 6500 steps, equaling to 274 fs simulation time (60 fs after peak interaction), we reduce the temporal resolution to 300 steps, corresponding to $\delta t = 12$ fs. The snapshots contain data of the electric, magnetic fields and carbon, electron and proton distributions in planes at $(x, y, z) = (x, y, 0)$ (in the polarization direction of the laser) and $(x, y, z) = (x, 0, z)$, (perpendicular to the laser polarization). The snapshots also save ParticleBinning diagnostics, containing the phase space $x - p_x$ and angular kinetic energy distribution for carbon ions and protons.

5.2. Benchmark simulation to experiment

Motivated by the ordering parameter r_c and the discussion in Section 4.2, we performed simulations for various target densities, ranging from $n_0 < 8.5 n_c$ up to $n_0 = 195 n_c$ with a step like density profile, and compared the particle spectra to the experimental data. For direct comparison over this wide range of densities, we choose shot 209 as the representative non expanded shot, 220 as the medium expanded shot with a initial central density $n_0 \approx 10 - 20\, n_c$ and 288 as a maximum expanded shot, $n_0 \approx 2 - 5\, n_c$. Fig. 5.1 shows the experimental proton and ion spectra for these 3 cases in direct comparison to results from simulation with corresponding, most likely densities according to the ordering parameter. For all three simulations the proton- and carbon spectra are in fair agreement, though detailed shapes are not reproduced. For shot 209, Fig. 5.1(a, d), we see a flat proton spectrum with particle numbers of the order of $4 \cdot 10^7$ N/sr/MeV. The medium expanded spheres show increased particle numbers, at the low energetic part of the spectrum at a level of $1 \cdot 10^7$ N/sr/MeV up to 11 MeV protons and a plateau with reduced particle numbers extending towards the cut-off energy slightly be-

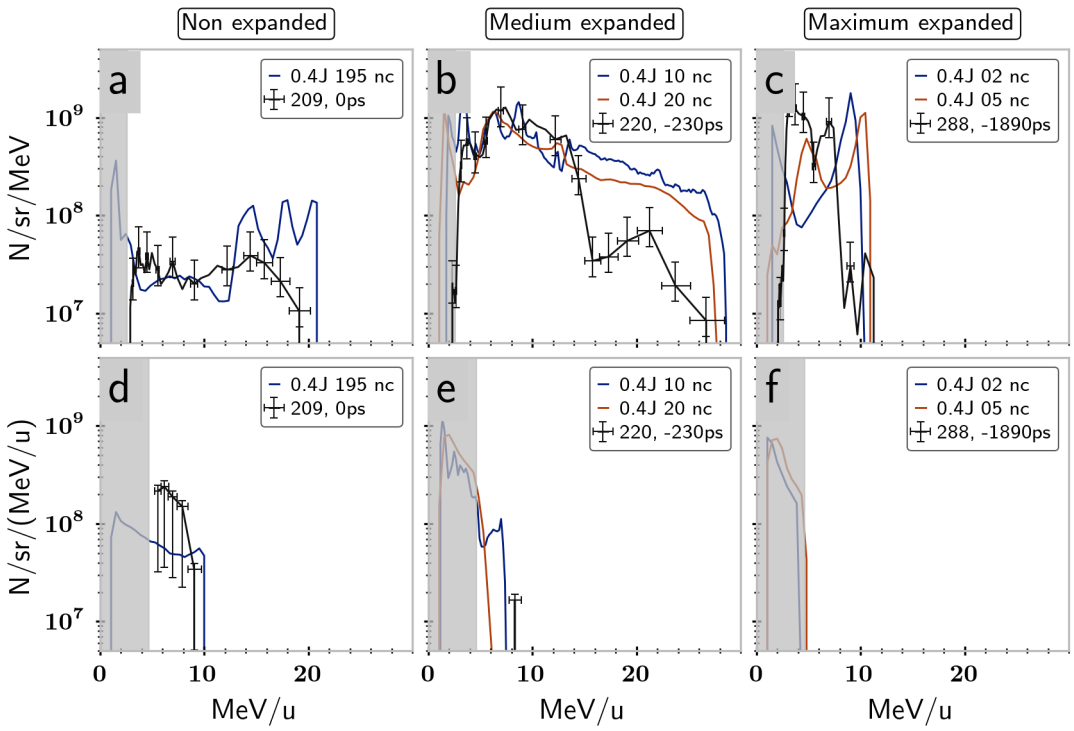

Fig. 5.1. *| Comparison of selected shots with PIC simulation results. First row shows proton spectra and the bottom row the corresponding carbon spectra for a non expanded sphere (a, d), a medium expanded sphere (b, e), and a maximum expanded sphere (c, f). The gray area indicates the detection threshold.*

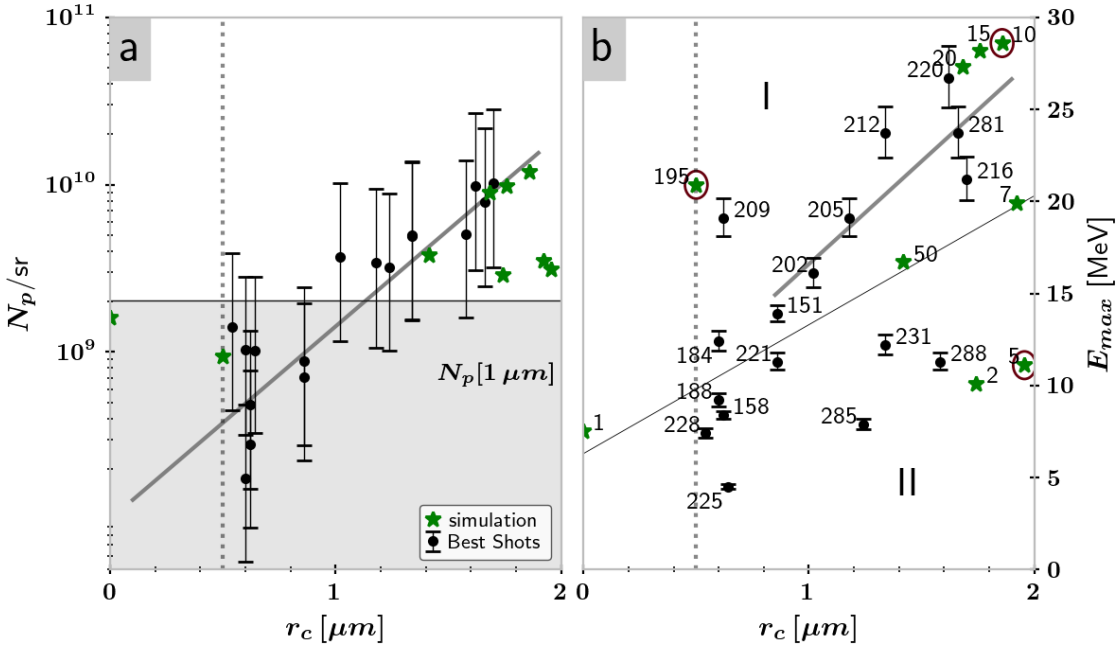

Fig. 5.2. *| Proton numbers (a) and maximum proton energies (b) for* 1 µm *spheres, with respect to ordering parameter for best shots per delay setting. Green stars represent the simulations.*
(a) Gray area could be in line with isotropic emission, gray line indicates of exponential growth of proton number with orderings parameter. (b) Gray line indicates linear growth of E_{max} *with ordering parameter in region I. The vertical gray dotted line represents non-expanded cases.*

low 30 MeV. The experimental carbon spectrum actually extends to lower carbon energies, which seem to be at a comparable or higher level as experimental data point, but at these low carbon energies the overlap with proton traces on the image plates cannot be totally excluded. Most importantly though, particle numbers and maximum cut-off energy are in good agreement between experiment and simulation (we limit the simulated spectrum to the detectable region of the spectrometer, i.e. protons with energies below 2.6 MeV were removed for the particle number comparison). For the maximum expanded spheres, Fig. 5.1(c, f) the maximum cut-off energy decreases, and no carbon ions are registered, in agreement with experiment. The overall agreement between the simulated and experimentally measured maximum energies and particle numbers over a wide range of densities is supported by Fig. 5.2, where the experiment observable proton number (N_p) and proton maximum energy (E_{max}) have been incorporated into the ordering param-

eter map. The gray area in Fig. 5.2a indicates that 2×10^9 protons/sr would be expected if the emission was perfectly isotropic. The gray line serves as a guide of the eye and highlights that the proton number per sr increases exponentially with ordering parameter and for $r_c > 1$ exceeds this threshold, i.e. proton emission becomes more forward directed. Fig. 5.2b indicates that for $r_c > 1$, the E_{max} results split into two populations, one with linear slope represented by the gray line and in line with PIC simulations for $n_0/_n c = 10 - 20$ (referred to as region I), and one that appears independent of r_c in line with PIC simulations at densities $n_0 = 2 - 5$ (referred to as region II). This suggests that in the experiments we have indeed captured representative shots for the three cases non-expanded ($n_0 = 195\, n_c$), medium expanded ($n_0 = 10\, n_c$), and maximum expanded ($n_0 = 5\, n_c$). The respective simulation results are highlighted by red circles. The largest energies and particle numbers are observed in simulations with $n_0 = 10\, n_c$. In the following we will use the PIC results for gaining deeper insight into these three cases and discuss the physical processes that are at play in particular in the efficient acceleration observed in the medium expanded case. This region is special, because the observed proton numbers per solid angle are higher than expected for an isotropic expansion. This threshold is marked by the gray area in Fig. 5.2a.

5.3. Acceleration dynamics observed in PIC simulations

5.3.1. Maximum Expanded (region II)

In this section we describe the case, where the target has a radial Gaussian distribution with $n_0 = 5\, n_c$, with a plasma scale length of $\sigma_r = 1.5\,\mu$m. Fig. 5.3 shows the evolution of the electron, proton and carbon densities and the longitudinal phase space at 3 distinct time steps around the intensity maximum of the laser pulse. The electron density maps are superimposed with the laser pulse electric field maps in the same plane at the respective times. The time stamps at $t = -11$ fs and $t = 14$ fs show that the plasma is transparent to the peak of the laser pulse. This is because $5\, n_c$ is smaller than the relativistic critical density for $a_0 = 12$. After surpassing the relativistic density threshold, latest at $t \approx -24$ fs for the simulated pulse, the laser penetrates through the target. Therefore, the electron density is modulated with $\lambda/2$, which is particularly visible in off-center regions. The mod-

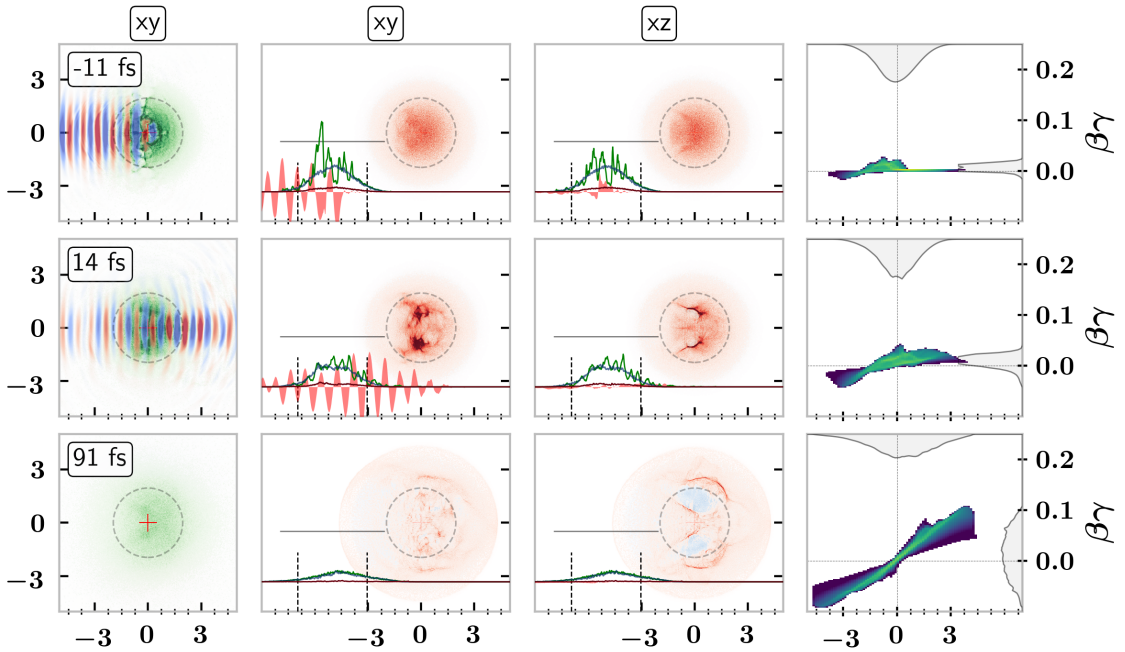

Fig. 5.3. *| Temporal evolution of electron, proton and carbon density profiles along the central laser axis for a central density of $n_{e0}/n_c = 5$. The first column shows the electron distribution (green) in the polarization plane (xy) and the E_y-component of the laser field. The second column shows the density distribution of protons (red) and carbons (blue) in the polarization plane of the laser (xy), while the third column is perpendicular to the laser plane (xz). The insets are moved to the left by 5 µm for clearer visibility and show the electron, proton and carbon lineouts along the central axis of the density distributions with colors corresponding to the 2D distributions. Column 2 additionally shows the laser field and column 3 the axial field E_x. The solid line indicates $\gamma\, n_c$ and the dashed lines the radius of $n_{e0}/n_c = 1$. The last column shows the longitudinal proton phase space.*

ulated electron density is co-propagating with the laser pulse and sweeps over the ions. Between the electron buckets an axial electric field is built up, which also sweeps over the ions. It propagates quite fast such that ions cannot keep up with the speed of this potentially accelerating field. Instead, the electrons are pushed away from the axis and the resulting field points rather radially.

This is because the ponderomotive force, strongest on the laser axis, and the laser creates a bow wave and depopulates the central channel, similar as reported in [115]. Fig. 5.4a shows the proton spectrum in forward direction as a function of time and reveals that most of the proton's energy gain is achieved after the laser

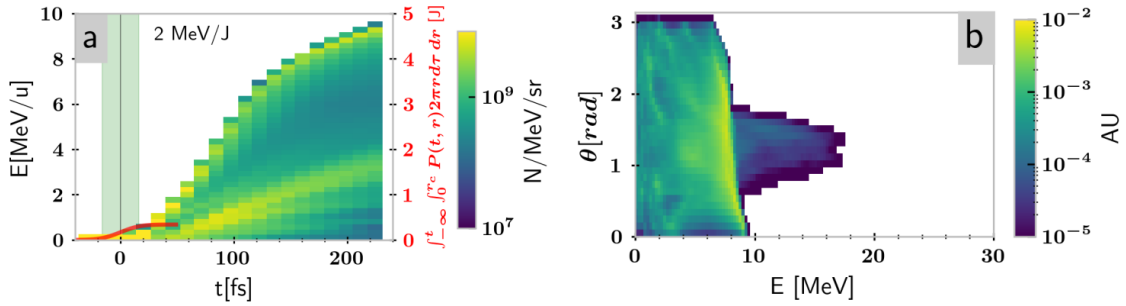

Fig. 5.4. *| (a) Temporal evolution the proton spectrum within an angle of* 0.1 *rad in forward direction. The red line indicates the integrated laser energy, that pass through the target. (b) Emission angle of protons, at* 205 *fs after main pulse arrival.*

pulse has passed the plasma. 80 fs after the peak interaction, the target core starts moving, and finally reaches an energy of 1 MeV/u. The center of mass motion is also represented by the slight shift of the momentum and position distributions in the phase space of protons and ions at 91 fs in Fig. 5.3. Integrating the proton energy that passed through the r_c radius of the target, shows an energy gain of the protons of 2 MeV/J. The fastest protons gain momentum until almost 180 fs after interaction with the peak of the pulse and the main emission direction is in 1 rad with respect to laser propagation (Fig. 5.4b). Yet, the angular distribution is broad, such that the most significant contribution is also visible in forward direction, which we captured in experiments. The scenario shows similarities to what has been reported by Hilz, [43, 68] for a 500 fs pulse.

5.3.2. Non-expanded targets

In the non-expanded case ($n_{e0}/n_c = 195$) the laser cannot penetrate the target and only drives electrons on the target surface. This remains true throughout the complete interaction as represented by the electron density distribution snapshots in Fig. 5.5. A thin shell of protons is emitted in 4π, already at $t \approx -24$ fs, and much before the peak of the pulse reaches the target center. With increasing intensity the ponderomotive force on the target front side pushes electrons inwards, and an electron density spike appears. Proton and carbon density subsequently follow to neutralize the charge separation. This density spike broadens, while it moves into the bulk, between time $t \approx -11$ fs and -27 fs. Due to the higher mass of the

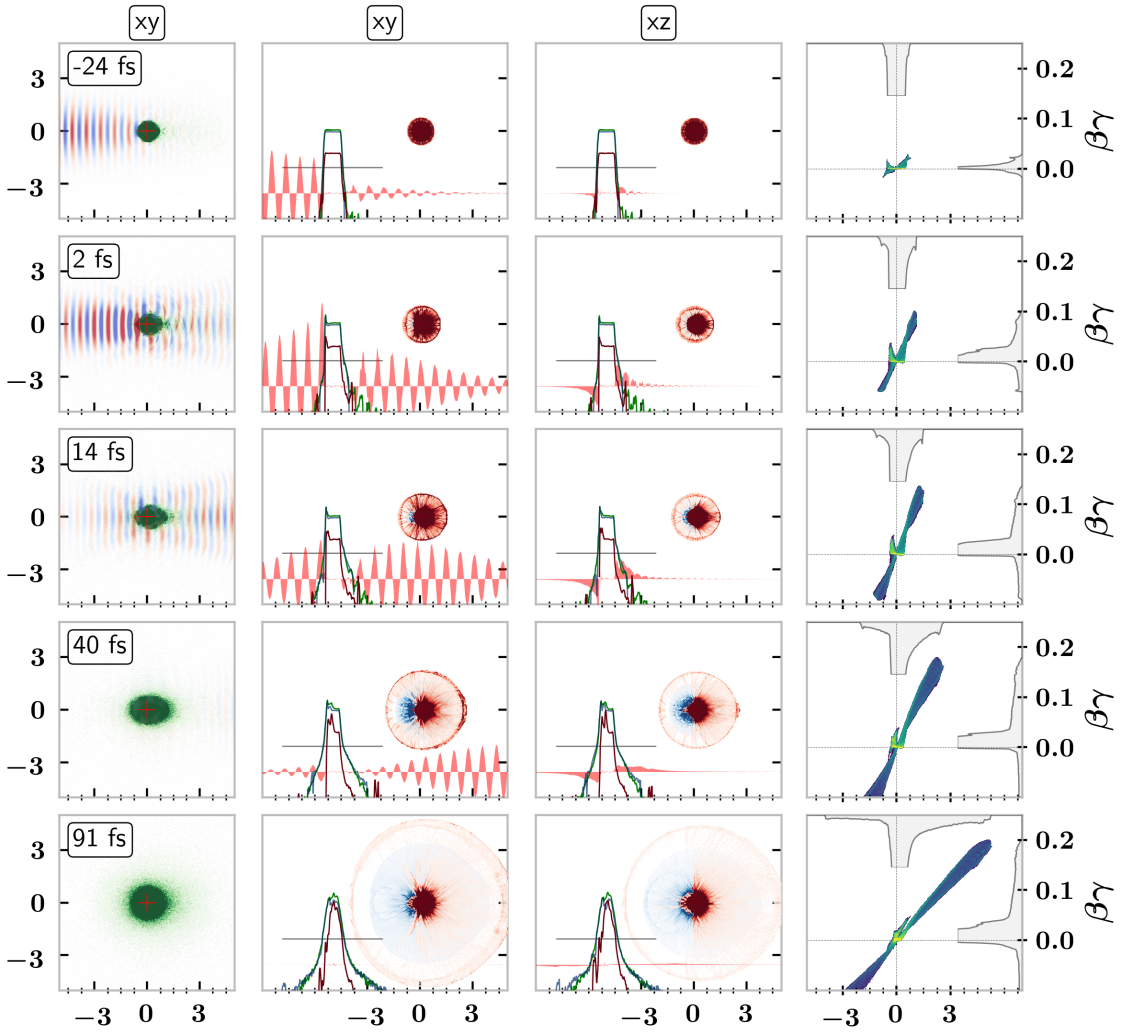

Fig. 5.5. *| Temporal evolution of electron, proton and carbon density profiles along the central laser axis for a non-expanded* 1 µm *sphere. The first column shows the electron distribution (green) in the polarization plane (xy) and the E_y-component of the laser field. The second column shows the particle number distribution of protons (red) and carbons (blue) in the polarization plane of the laser (xy), while the third column is perpendicular to the laser plane (xz). The insets are moved to the left by* 5 µm *for clearer visibility and show the electron, proton and carbon charge density along the central laser axis with colors corresponding to the 2D distributions in a logarithmic scale. Column 2 additionally shows the laser field and column 3 the acceleration field E_x (filled red). The solid line indicates $\gamma\, n_c$. The last column shows the longitudinal proton phase space.*

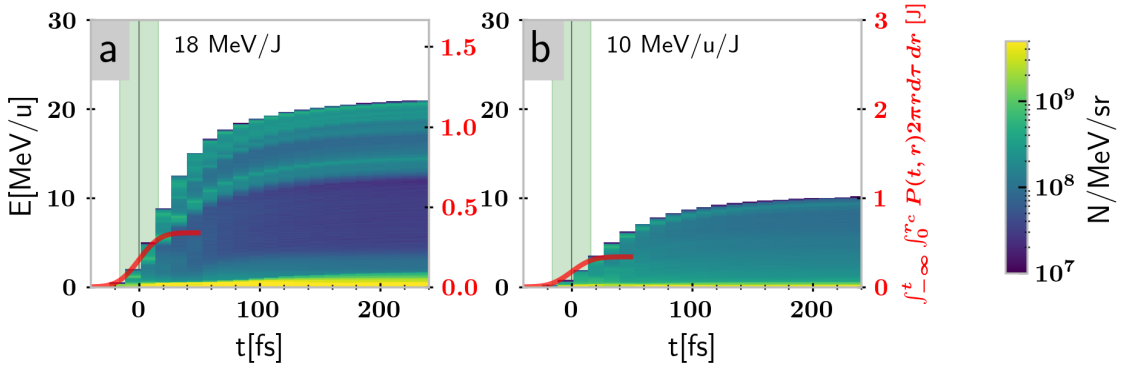

Fig. 5.6. *| Temporal evolution of the proton (a) and carbon spectrum. (b) In forward direction within in an angle of 0.1 rad. The red line is the integrated laser energy through the central target plane at $x = 0$, re-scaled with 18 MeV/J (a) and 10 MeV/u/J (b).*

carbon ions, the proton peak outruns the carbon peak. This imbalance suppresses further expansion of protons towards the target's laser upstream side, and pushes the protons forward to the target rear side (laser down-stream). This component is visible in the phase space diagrams of the protons. The population accelerated forward does not gain high momentum though.

While the electrons are energized by the laser pulse, the electron density expands into vacuum and creates a non-oscillating electric field at the plasma-vacuum boundary. The target bulk of the plasma remains field free. As the plasma diameter remains smaller than the FWHM of the laser focus, the laser wraps around the plasma and confines electrons on the target rear side, which creates an accelerating field that is modulated with half the laser frequency $\lambda/2$. The fastest protons quickly decouple from this accelerating field. Their main acceleration ends after $\approx$ 40 fs, after which the bunch expands due to intra-pulse expansion, and the highest energetic protons reach up to 21 MeV. The target bulk, however, is barely affected by the laser plasma interaction and also gains little momentum, compared to the maximum expanded case. Fig. 5.6 shows the time evolution of the proton (a) and carbon (b) spectrum. It appears that the fastest carbon ions with 10 MeV/u drive protons forward and thin out the spectrum of protons below this energy, an observation that is known from foil target experiments [116–118] and has also been reported by Ostermayr in the framework of multi species ambi polar

expansion of spherical targets, [72]. The most energetic protons gain almost twice the energy and reach 20 MeV.

5.3.3. Medium Expanded (region I)

This scenario is arguably the most interesting case. It yields the highest proton energies and up to 100 times higher particle numbers within the detectable range of the experiment. Therefore, we have performed more detailed simulations with n_0 of 7, 10, 15 20 and 50 n_c to study this regime in more detail. The 10, 15 and 20 n_c cases show very similar results. 7 and 50 n_c show some of the prominent characteristics, but are rather transition cases. Here we present the case of $n_{e0}/n_c = 10$ as a representative case for this scenario, which in the simulation also yields the highest maximum energies.

For a central density of $n_0 = 10\,n_c$, the plasma scale length is 1.22 µm. The relativistic critical density diameter is $d(\gamma n_c) = 0.97$ µm and the critical density diameter is $d(n_c) = 3.7$ µm. With a laser focus of 1.8 µm FWHM, the overcritical core is smaller than the laser focus. Fig. 5.7 presents the results of the simulation. The diameter of γn_c and n_c are indicated by the dashed circles in the 2D particle density projections and as dashed lines in the insets of the profiles along the central laser axis. As the laser hits the target, it only interacts with the target front side and propagates up to the relativistic critical density surface at $\gamma n_c = 8.5$. In fact the target rear side is almost unchanged up to the arrival of the peak of the pulse. Over the course of the interaction, the laser snow plows the electron density visibly forward and the laser radiation is diffracted radially outwards. A dense, and relatively slow moving electron bunch forms and remains confined during the complete time of interaction. The strongest axial field now establishes between this electron bunch and the ions, and because the electron bunch remains radially confined and moves slowly, the proton density (and at later times also the carbon density) can reshape in response to this axial field. From -8 fs to $+5$ fs the proton bunch and the electron front form a synchronously moving accelerating alliance, in which the electron spike precedes the dense and continuously adapting proton layer, even though the linear polarized laser pulse violently drives the electrons forward by the $v \times B$ term with twice the laser frequency. The asymmetry of trans-

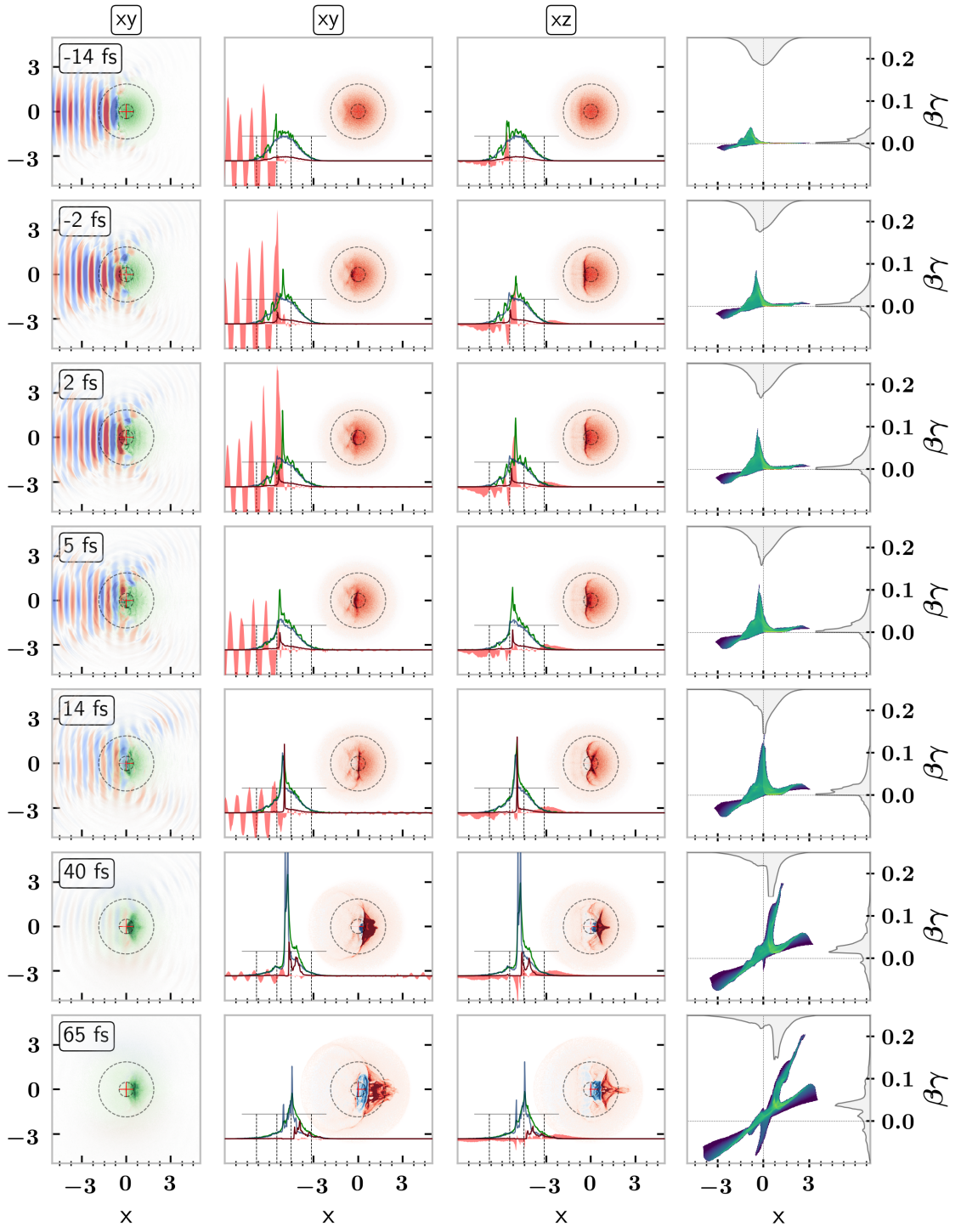

Fig. 5.7. *| Temporal evolution of electron, proton and carbon density profiles along the central laser axis for a central density of $n_{e0}/n_c = 10$. The first column shows the electron distribution (green) in the polarization plane (xy) and the E_y-component of the laser field. The second column shows the density distribution of protons (red) and carbon ions (blue) in the polarization plane of the laser (xy), while the third column is perpendicular to the laser plane (xz). The insets are moved to the left by 5 µm for clearer visibility and show the electron, proton and carbon lineouts along the central axis of the density distributions with colors corresponding to the 2D distributions. Column 2 additionally shows the laser field and column 3 the acceleration field E_x. The solid line indicates $\gamma\, n_c$ and the dashed lines the radius of $n_{e0}/n_c = 1$ and $n_{e0}/n_c = \gamma n_c = 8.5$. The last column shows the longitudinal proton phase space.*

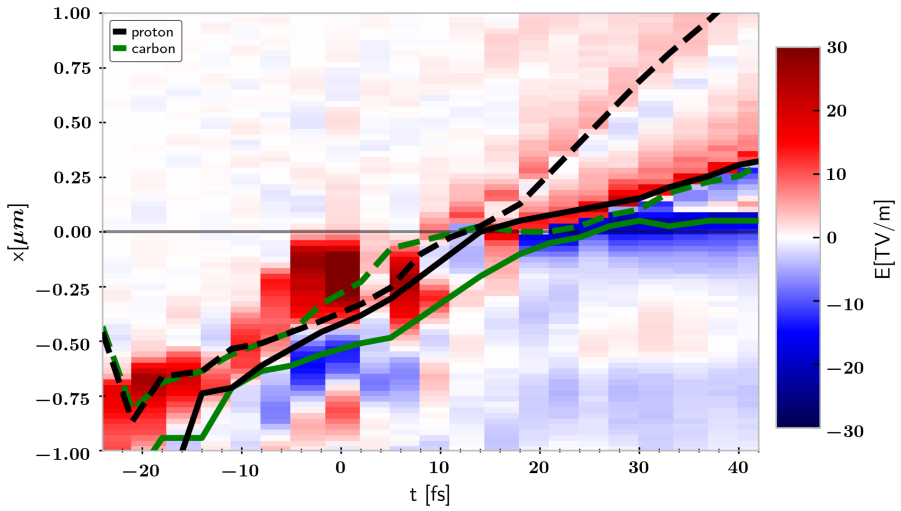

Fig. 5.8. *| Temporal evolution of the ion bunches and the axial field (colormap). The solid lines represent the trailing edge of the bunch (density spike), and the dashed lines the leading edge for protons and carbons. $x = 0$ is the target center along the laser axis, and $t = 0$ equals the arrival of the laser pulse at the center.*

verse electron motion due to the linear laser polarization manifests in the distinct differences of the proton density distributions in the two planes. In the polarization plane (xy, 2nd column), the density first converges but starts diverging after 40 fs. In the xz projection (perpendicular to the laser polarization) the proton density remains converging. The longitudinal phase evolution clearly shows that the fastest protons originate from the acceleration structure that is driven by the laser pulse. The contribution from the plasma-vacuum boundary remains visible but is less pronounced.

However, the well defined axial field is observed only up to time 2 fs. Between 2 fs and 5 fs the polarity of the laser field switches, and the accelerating structure of electrons preceding protons and carbons breaks down. In the next cycle, a new electron peak is formed, but behind the proton peak and therefore the acceleration of the proton bunch stagnates. Instead, the axial field now establishes between electron and carbon ions and the bunching can be observed in the density projections at 65 fs. It is interesting to note that the center of mass moves forward, significantly, which is visible in both density as well as phase-space distribution plots.

In this first acceleration phase, which terminates at around the laser intensity max-

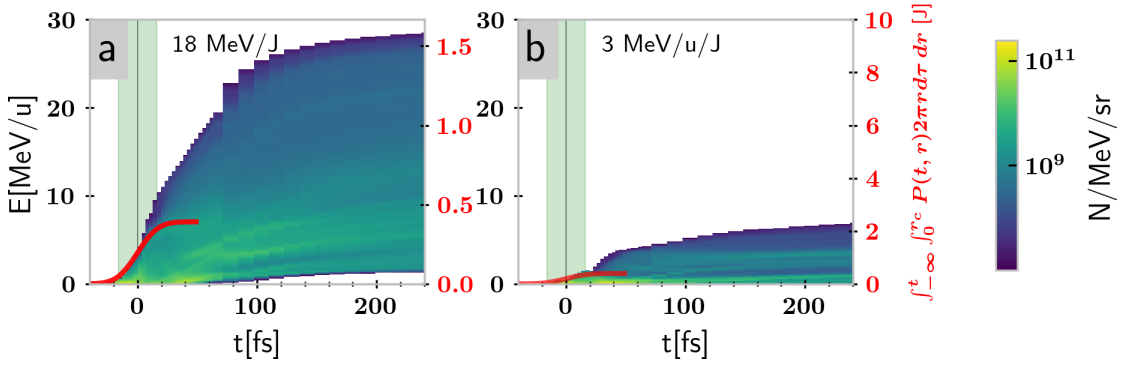

Fig. 5.9. *| Temporal evolution of the (a) proton and (b) carbon spectrum in the forward direction within an angle of* 0.1 *rad. The red line shows the integrated laser energy, which has passed through the target. The green area depicts the FWHM of a* 400 *mJ laser pulse. The color encodes the particle number density.*

imum, the fastest front side protons have gained a longitudinal momentum of $p_x = 0.1$, equaling a kinetic energy of only 5 MeV. Following the phase space further in time, they gain additional momentum and a characteristic X-shape forms in the longitudinal phase space, and that the fastest protons here indeed originate from the laser irradiated front side becomes obvious. In the course of leaving the plasma, the fastest protons gain approximately the same momentum again and reach $p_x \approx 0.2$, or 28 MeV. It is, however, instructive to illuminate the rather 'controlled' first phase of acceleration in more detail.

Fig. 5.8 reveals a temporally resolved insight into the proton and carbon dynamics as the bunches are accelerated in the first phase. It shows the leading and trailing edge of the proton and carbon bunches that were manually extracted by inspecting the density line outs at different times. The positions are superimposed to the axial field E_x on the central laser axis. Red regions accelerate, blue regions decelerate. Up to $t < 2$ fs the accelerating field increases. Both leading fronts of protons and carbons can keep up with the field, but only the trailing edge of the proton bunch remains in the accelerating part. The trailing carbons lose touch and are only picked up again at $t = 10$ fs, after the acceleration phase for the protons has ended and the electron spike and with it the axial field swaps backwards. Regardless of whether we consider the leading or trailing edge, the slope of the bunch trajectories is nearly constant, during the laser plasma interaction (-14 fs $< t <$ 14 fs), and the propagation speed is between 0.07c and 0.09c. For a

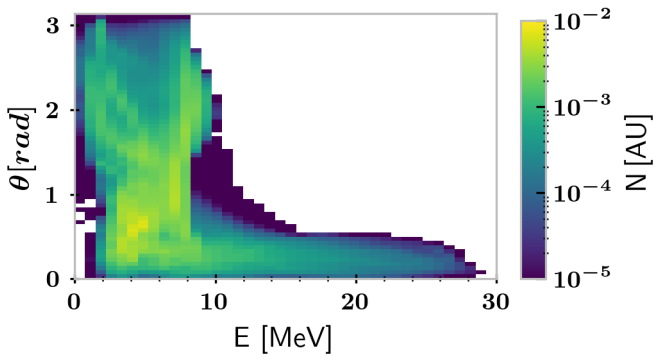

Fig. 5.10. *| Emission angles of proton 167 fs after main-pulse arrival. The fastest protons are ejected in the forward direction.*

homogeneous density target with $n_0 = 10\,n_c$, we estimate a hole boring velocity (Eq. (2.43)) of $v_{hb}/c = 0.06$, but we note that the front side of the target is less dense than the core of the Gaussian.

At $t \approx 14$ fs the bunch has an axial FWHM extent of only 0.03 µm and its highest proton density of $n_p = 26\,n_c$, which is comparable to the proton density in a solid polystyrene sphere. Thereafter, the confining field does not reestablish (because the laser pulse is over) and hence the bunch explodes. The bunch front side then accelerates to a speed of $v_{back}/c = 2 \cdot v_{front}/c = 0.16$ (corresponding to a proton energy of 12 MeV), which is what one would also expect from collision-less shock acceleration. After 40 fs the fastest protons enter the sheath field at the rear of the expanding target, where they get further accelerated from the field that has established at the plasma-vacuum boundary. The field is maintained for many 10 fs and the protons gain their final energy of up to 28 MeV.

To conclude this description, Fig. 5.9 shows the temporal evolution of the proton and carbon spectra in the forward direction. In the first half of the laser pulse, the maximum proton- and carbon energies follow closely the cumulated laser energy that has passed through the target plane at $x = 0$, within a disk of diameter $d(n_c)$, as indicated by the red line. The proportionality factor between proton energy and laser energy is estimated to 18 MeV/J for the proton and 3 MeV/u/J for the carbon ions. This conversion factor is ~ 10 times higher than the 2 MeV/J determined for the maximum expanded regime in section Section 5.3.1

Finally, Fig. 5.10 shows the angular dependent differential proton spectrum ob-

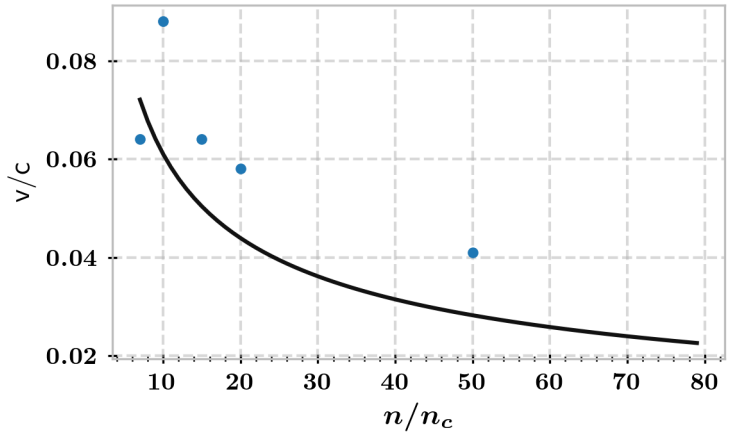

Fig. 5.11. *| The solid line shows the hole-boring velocity of a homogeneous density target. The blue dots indicate the velocity of the proton bunch. As expected we see an increase in the velocity for less dense targets. Below* $8.5\,n_c$ *the laser transmits through the target and no distinct proton front is formed.*

tained at 167 fs after the main pulse interaction from the simulation. Protons with energies up to 8 MeV are emitted isotropically, higher energetic protons are highly directed forward and confined within an angle of ± 0.5 rad to the laser propagation direction. The bunch contains about 30% of the total number of particles in the beam, which is about 2 times more than what one would expect from isotropic expansion. This closely resembles the results of our measurement.

5.4. Discussion

5.4.1. Optimal target density

It is important to note that we restrict the discussion of our results to the practicably applicable case of one selected initial target sphere diameter (1 µm). As we vary the central density, the scale length varies as well due to the constant number of protons, carbons and electrons across the different simulations. From each simulation we generated the trajectories of the proton bunches as in Fig. 5.8, and estimated the velocity of accelerating structure and the proton bunch during the laser plasma interaction, within the time interval $t = -14\,fs$ to $t = 14\,fs$. Fig. 5.11 shows these velocity values as function of initial target density n_0. For $n > 10n_c$,

the data points lie consistently above the hole boring velocity calculated for a homogeneous plasma density n_0. As we calculate the hole-boring velocity based on the central density, we expect the measured velocities in the less denser regions to be higher than the estimated hole boring velocity.
For spheres, with a central density well below the relativistic critical density, $n_0 \ll 8.5$, no such acceleration structure is formed, because the plasma is transparent to the laser. For densities slightly below the relativistic critical density, eg. $n_0 = 7\,n_c$, the laser is still reflected in the rising edge of the pulse, where a small bunch forms. At the peak, the laser can break through, and the induced accelerating field sweeps too quickly over the target, such that the protons cannot be captured. In accordance with an increased hole-boring velocity for less dense targets, the reflection front moves at the greatest speed of a target density that is a low as possible, while still maintaining a sufficient reflection (or absorption) of the pulse. For a 0.4 J laser pulse and the target that comes from a 1 µm polystyrene sphere, this is the case at a central density of $10\,n_c$.
Similar schemes have been studied by [46] for homogeneous spherical targets of different density, while the sphere diameter there was larger than the laser focus diameter. In accordance with our simulations they report on a similar transition to a HB dominated acceleration around the critical density. However, targets with these reduced, homogeneous shapes will remain very challenging for experimental studies. Additionally [45] found that the longitudinal Gaussian shape, can be beneficial for the acceleration of protons.
An optimal acceleration mechanism from isolated spheres was reported by [119], when the relativistic skin depth of the laser pulse becomes comparable to the thickness of the shock at the time of peak intensity. This favors the existence of an optimally tuned isolated target to the laser pulse, which might be close to what we achieved here, although comparison between linear and circular polarization is not straight forward and in particular the proton spectra are expected to differ dramatically.

5.4.2. Extrapolation to higher laser energies

We performed a set of simulations at higher intensities by scaling up the laser pulse energy to study the scaling in the medium expanded regime. We kept the

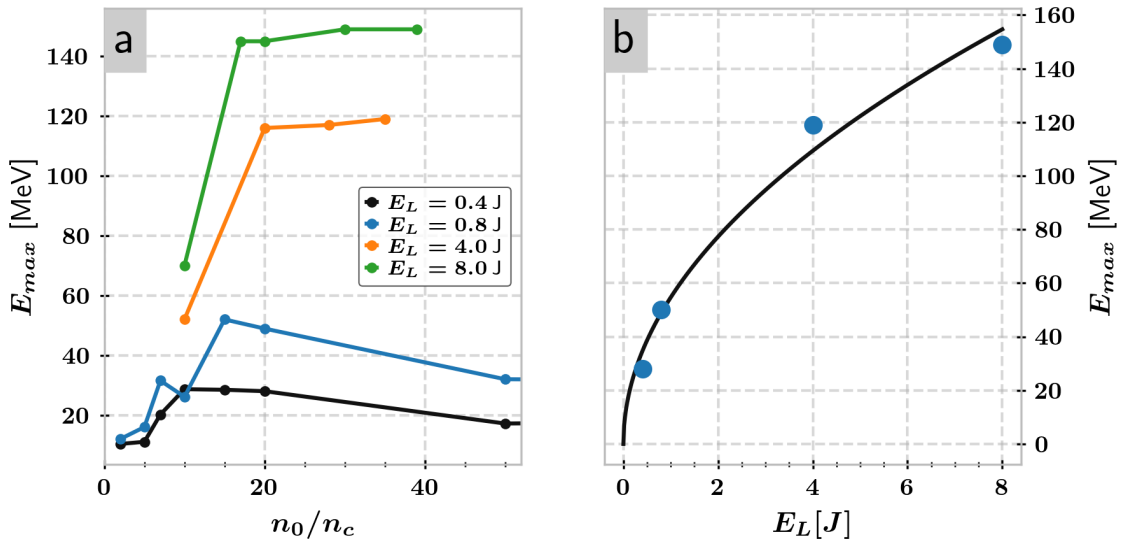

Fig. 5.12. *| a) Maximum proton energy versus central density for four distinct laser energy values as indicated in the legend. b) Maximum energy at optimum density and scaling* $54.7\,MeV \cdot (E_L/J)^{1/2}$ *(black curve).*

laser focus, laser pulse length and initial target constant for all simulations. Using the same initial reservoir of ions and electrons, we varied the central density of the radial Gaussian, while adjusting the scale length to have conserved particle numbers as before. The laser energy was increased to a level achievable by up to date laser facilities such as, e.g., Centre for Advanced Laser Applications (CALA). As a side note, we expect very comparable results in terms of maximum particle energy, particle numbers and spectral shape, if $E_L/d^2_{FWHM_L} = \text{const}$, i.e. for unchanged peak fluence. Increasing for example the laser energy and at the same time using a weaker focusing optics, will leave parts of the laser energy unused as it passes the target without participating in the interaction.

Fig. 5.12a shows the maximum proton energy as a function of the central density for different laser energies. The black line shows the maximum proton energies for the 0.4 J case described in length in the previous section. The function peaks at $n_0 = 10\,n_c$, $E_{max} = 28$ MeV.

Doubling the laser energy to 0.8 J ($a_0 = 18$) shifts the optimum density to $n_0 = 15\,n_c$, again slightly above the relativistic critical density 12.5 nc. The maximum energy increases to 50 MeV.

For further increased laser energies, we can not identify an optimum around the

relativistic critical density, which is $\gamma n_c = 26$ for 4 J ($a_0 = 38$) and $\gamma n_c = 37$ for 8 J ($a_0 = 53$). Fig. 5.12a shows in the case of 4 J and 8 J the maximum proton energy is almost independent of the central target density, for the simulations performed. Even for targets that are initially relativistic under-critical, we see the reflection front appearing. In the temporal evolution the created shock front stays overcritical. We find a maximum proton energy of 119 MeV for a 4 J laser pulse and a target with central density of $n_0 = 38\, n_c$, which is a 5 times increase compared to the 0.4 J simulations. The same applies to the 8 J simulations with a highest proton energy of 149 MeV, and a 7 times increase in the proton energy compared to the 0.4 J shots, but 20× the laser energy. Empirically we find that the maximum proton energy scales with

$$E_{max} = 57 \frac{MeV}{J^{1/2}} \cdot E_L^{1/2}, \tag{5.3}$$

as shown in Fig. 5.12b. It is interesting to investigate potential reasons for this unfavorable scaling at larger laser energies.

Fig. 5.13 shows the evolution of the proton spectrum for $n_0 = 20\, n_c$ and 8 J laser energy. Again, the cumulated laser energy that passed the target (red line) is superimposed. In the initial phase, the maximum proton energy scales with the integrated laser energy with a scaling factor 18 MeV/J, quite similar as for the 0.4 J case. But already before the peak intensity, the fastest protons detach from the acceleration front, move into the bulk target, and run out of the acceleration structure that is driven by the laser reflection front. As the fastest protons reach the target backside, they get further accelerated by the sheath field on the rear side. For the case shown in Fig. 5.13 the fastest protons detach from the front at −6 fs, and are then ahead of the actual laser reflection front. For more dense targets the detachment happens earlier and the effect becomes even more prominent in the spectral evolution. Harvesting only parts of the laser energy in the rising edge of the pulse is an explanation, why we see the plateau in Fig. 5.12a for the maximum proton energy. It is likely that an independent variation of density and density scale length (for example by adapting the initial sphere diameter) allows identification of a steeper scaling with laser energy.

Finally Fig. 5.14 shows the angular distribution of the protons for the 8 J case. The forward directed proton beam within a angle of 0.5 rad, hosts about 70 % of

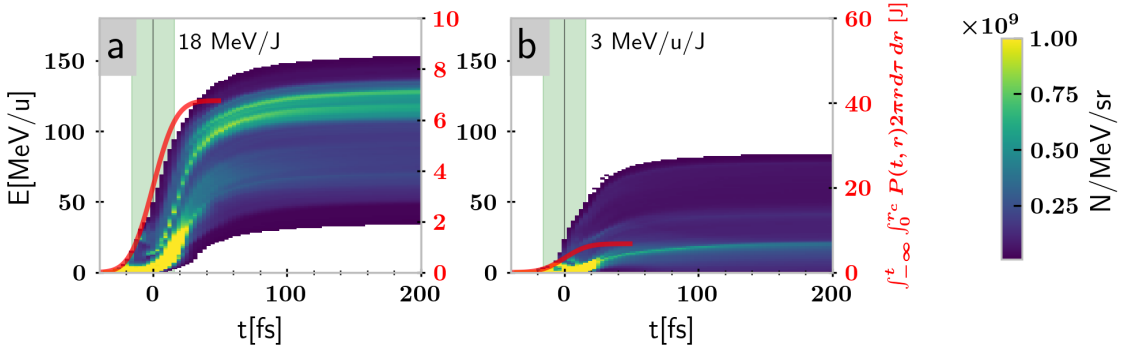

Fig. 5.13. | *Temporal evolution of the (a) proton and (b) carbon spectrum in the forward direction within an angle of* 0.1 *rad. The initial central density is* $n_0/n_c = 20$. *The red line shows the integrated laser energy, which has passed through the target within a radius of* $r(n_c) = 1.9\,\mu m$. *The green area depicts the FWHM of a* 8 *J laser pulse. The color encodes the particle number density.*

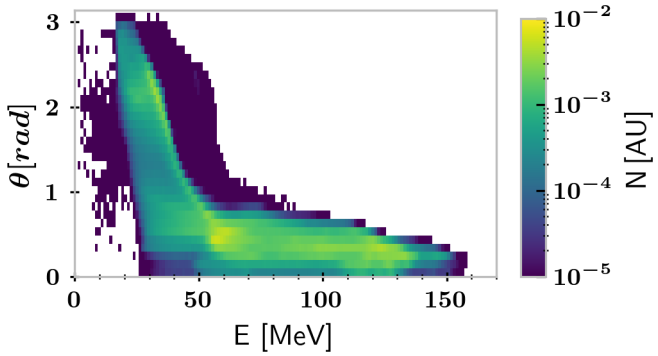

Fig. 5.14. | *Emission angles of protons 167 fs after main pulse arrival. The fastest protons are ejected in the forward direction.*

the particles provided by the sphere. Compared to the $a_0 = 12$, $n_0 = 10$ case with 28 % in the forward beam, the proton fluence is approximately 10 times higher.

5.4.3. Concluding remarks

In the simulations we found a three staged acceleration mechanism for isolated reduced density targets. In the first phase, a hole-boring front is created due to the laser ponderomotive pressure. Either when the rising edge of the laser pulse has passed, or when the plasma pressure exceeds the laser pressure this phase terminates, and a shock front is detached from the hole-boring front, propagating

through the target. For a narrow bandwidth and dense proton bunch, one would like to optimize the hole-boring acceleration phase, by matching the laser temporal shape to the axial density shape. Additionally, in order to reduce target heating, and trigger the coherent acceleration of the target, one could use a circularly polarized laser. Using a 33 fs pulse, [45] theoretically found a linear scaling of the proton energy with the laser energy, what could be a sign of an RPA like acceleration mechanism. A scenario for a constant hole boring velocity as an application for fusion, has gained wide interest. [120], applied an inhomogeneous, exponentially decaying density profile. The scenario of a matched target to the laser shape, has also been studied theoretically by Weng et. al. [75]. Their approach suggests a time-independent hole-boring velocity $v_{HB0} = c\sqrt{B_0}/(1+\sqrt{B_0})$, with B_0 as a time independent pistioning parameter, such that all ions that are captured by the axial acceleration field gain the same velocity. For an experimentally accessible Gaussian temporal profile, this requires also a Gaussian density profile along the laser propagation direction. The study by Weng et. al. was centered around ($\sim$ps) pulses. The applicability for fs, with much faster rise times still has to be demonstrated.

However, in view of this approach, requesting a constant velocity of the acceleration field is not ideal for proton acceleration, because the bunches are not relativistic yet. Therefore, it seems very interesting to study the approach of engineering the plasma and laser temporal profile together in a much more general approach. Even after more than two decades of research into laser-driven ion acceleration in plasmas, this topic has more surprises in store, which we can further decode with improved target technology.

Chapter 6

Summary and Outlook

6.1. Target system for isolated spheres

We have extended the capabilities of the target system for isolated targets for the needs at a high-power laser system, and proven its functionality at a 200 TW (JETi 200) laser system and a 5 TW system (ZEUS). The key developments include automation of all mechanical components and the integration in a software system that allows remote control and semi-automated target replacement. The software control reduces the probability of operator errors and increases the control on the relevant parameters in the process. The parameters include trapping voltage, trapping frequency, charging time, and charging current. The reproducible charging and higher rigidity results in comparable charge-to-mass ratios of the loaded particle and massively simplifies the operation of the trap, after finding a parameter set that allows reliable positioning. As repeated positioning of consecutive targets is still limited to $\pm 2\,\mu m$, overlapping the target with the laser focus requires the focus diagnostics, as other imaging systems were not tested for the reliability. Improving a retro-imaging system via the focusing OAP and the diagnostics camera in the damping system might avoid the time consuming overlap of the sphere and the laser focus in the focus diagnostics in future. This, however, will also require laser stability over several hours.

The interplay of the Paul trap with the Supervisory Control and Data Acquisition Software Tango-Controls, allows integration into larger experimental setups. It also simplifies the extension of the system to other target materials, as e.g. videos of the spheres and post-processing routines for positioning accuracy can be auto-

Table 6.1. | *Experimental parameters for Peta-Watt class laser campaigns. [42, 43]*

	Hilz	Ostermayr	This work
	f/2.5	f/2.5	f/1.5
E_L [J]	150	55	1.5
τ_L [fs]	500	170	32
λ_0 [nm]	1054	1054	800
I_0 [W/cm^2]	$7 \cdot 10^{20}$	$3 \cdot 10^{20}$	$4 \cdot 10^{20}$
d_{FWHM} [µm]	4	10	2
hit	12/12	19/33	73/125
target	PMMA	PS	PS

mated, thus reducing training time on the system.

6.2. Ion Acceleration from isolated spheres

We described the interaction of focus-sized mass limited targets with a high-power laser pulse. This study extends previous work with laser pulse energies of many 10 J in many 100 fs on micron-sized spheres. We performed shots with high temporal contrast on non-expanded spheres, as well as shots on pre-expanded spheres, that were illuminated with a dedicated prepulse to manipulate the plasma density at main pulse arrival. We studied the influence of this pre-pulse on laser ion acceleration. We find that the particle number in the laser propagation direction increases by more than one order of magnitude with pre-expanded targets. The increased particle number is accompanied by an increase in the maximum proton energy, yielding maximum values of up to 27.4 MeV from a 1.4 J laser pulse. From PIC simulations we dedicate this energy increase to an initial hole-boring phase, that boosts the particle energy and pushes the target as a whole forward. A crucial requirement for the process is the creation of a laser reflection front in the target. For increased laser intensities, PIC simulations suggest an increase of the maximum proton energy with the square root of laser pulse energy, at otherwise constant target and focus parameters.

Table 6.1 compares our parameters to the two studies conducted at Peta-Watt class laser facilities. While Ostermayr et al. [42] and Hilz et al. [43] used a glass

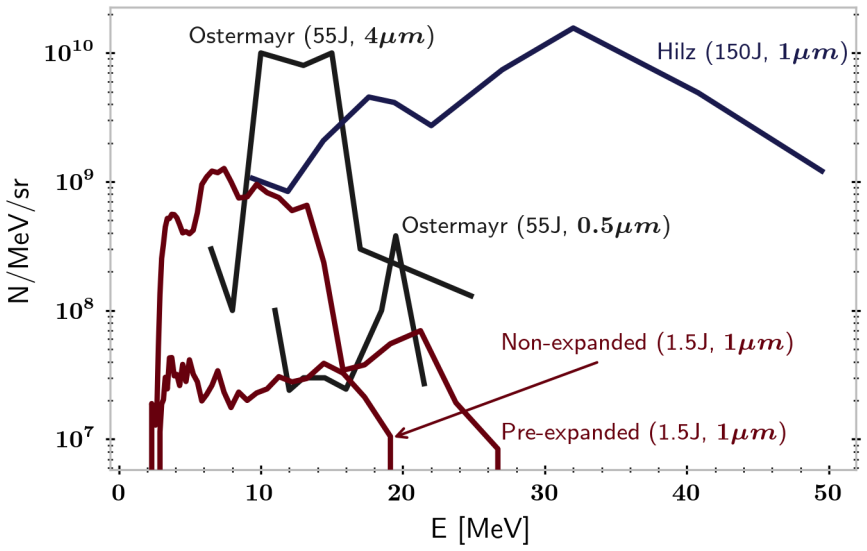

Fig. 6.1. *| Selected shots from the three campaigns conducted on truly isolated spheres, Hilz et al.[43], Ostermayr et al. [42] and this work.*

laser system, with laser energies in excess of many 10 J and a pulse length greater than 100 fs, this study was performed at lower laser energies (1.5 J) and a shorter pulse duration (32 fs). Fig. 6.1 shows selected spectra from the three campaigns. Ostermayr et al. aims for the best available laser contrast, by applying a plasma mirror at the TPW laser. These experiments can be compared to the non-expanded shots of this work. The selected shots for a 0.5 µm and 4 µm PS sphere show comparable maximum proton energies as obtained in this work. The particle number for the 0.5 µm is at the same level as the non expanded shots in this work, even though the smaller spheres only contained 1/8 of the protons. A similar case can be made for the 4 µm spheres, the measured proton number of particles is $\sim$ 140 times higher than for the non-expanded shot of this thesis, while the number of protons contained in the sphere was larger by a factor of 64. For both cases we see an increased particle number that can not solely be explained by variation in number of protons contained in the sphere and thus participating in the laser-plasma interaction.

Hilz et. al. uses the inherent pre-pulse level of the PHELIX, which ignited a plasma about 200 ps before the main pulse arrival. The plasma pre-expansion yielded a reduced density target for the main pulse interaction, and thus these

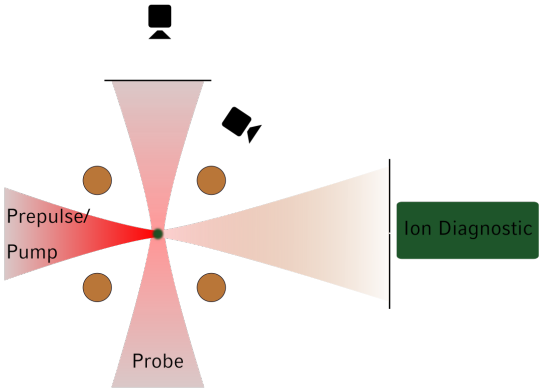

Fig. 6.2. *| Scheme of a pump-probe setup. The pre-pulse and the main pulse are co-propagating, while the probe is probing the plasma at the main pulse arrival from bottom up.*

experiments compare to the pre-expanded shots in this work. The experiment used a Polymethylmethacrylat ($C_5H_8O_2$) (PMMA) sphere with 1 µm in diameter. PMMA has a similar number of protons as polysterene. Comparing these shots, the maximum proton energy roughly scales with the laser intensity, which was about a factor of 2 higher in the case of Hilz et al.. The 100-fold increase in laser energy could not efficiently be converted to higher proton energies. From our simulations, we see a similar increase in the maximum proton energy, when doubling the laser energy and thus yielding twice the laser peak intensity. The particle number for Hilz et al. is about 20 times higher than in this work, indicating a higher directionality. From the simulations we can also see a lower divergence of the high energetic part of the beam with increased laser energy, but it does not reach the level as in Hilz et al.. For the simulations that compare well to the experiment, the forward cone within 1 rad contains about 54% of the particles, while doubling the energy, the particle number in this cone increases to 70%. For the simulation with the highest laser energy (8 J), the cone contained up to 85% of the protons initially contained in the sphere.

Follow up experimental as well as numerical studies of isolated micro spheres remains interesting. For an experimental study, a next step could improve control of the laser- and target parameters. In a dedicated pump-probe setup, [88] we have studied the plasma expansion at intensities of $10^{16}\,\mathrm{W/cm^2}$. The analysis of the probe- and transmission images resulted in a good estimate for the plasma

density in the near critical density regime. The design of the Paul trap allows for various viewing angles, such that probing and ion acceleration could be realized in a united setup, as sketched in Fig. 6.2. This would enable clearer identification of the interplay of target densities and ion acceleration and reduce uncertainties in data interpretation.

For higher laser pulse energies, such as available with the ATLAS 3000 at CALA, the PIC simulations suggest that proton maximum energies beyond 100 MeV are achievable with 1 µm spheres, in particular when appropriately pre-expanded. It is likely, that the rather weak scaling with the square root of the laser energy does not represent the ideally achievable best scaling. Pragmatically, it seems obvious that a small laser spot and a high laser energy is beneficial. The studies by Hilz et al. and Ostermayr et al. suggest that increased pulse duration and pulse energy could increase the particle yield. Optimizing for maximum particle yield or maximum proton energies, by varying the initial sphere diameter and the laser pulse duration, however, are interesting possibilities to further optimize laser ion acceleration performance in the next numerical and experimental endeavors.

Appendix A

Appendix

A.1. Spectra $1\,\mu m$ spheres

Here we present the corresponding spectra to the shots in Fig. 4.6. The shots are sorted by their belonging to population I and II. Spectra in population II do not show carbon ions. Especially the spectra in reduced intensity area ($r_c/r_0 > 2$) of population II have a very similar shape, with a cut-off energy of about 10 MeV, a flat differential proton distribution, which ends abruptly towards the end. Meaning that the cut-off energies are not defined as the point, where the signal vanishes in noise level of the detector, see Fig. A.1.

Fig. A.2 shows spectra of the shots of population I. The best shots for each delay setting are marked with an orange border around the annotation for better visibility. Interestingly, we detect carbon ions in a majority of the shots here. Quantifying these spectra just by means of a maximum cut-off energy does not include the unique features of the different spectra in this population, as all spectra show either peaked or flat particle number distributions over the proton energy. Even tough not yielding the highest proton energies, shots 196, 198, 234, 184, 202 and 215 show an distinct peaked spectrum at the high energetic end of the proton spectrum. The shots with the highest proton energies are discussed separately in Section 4.2.4

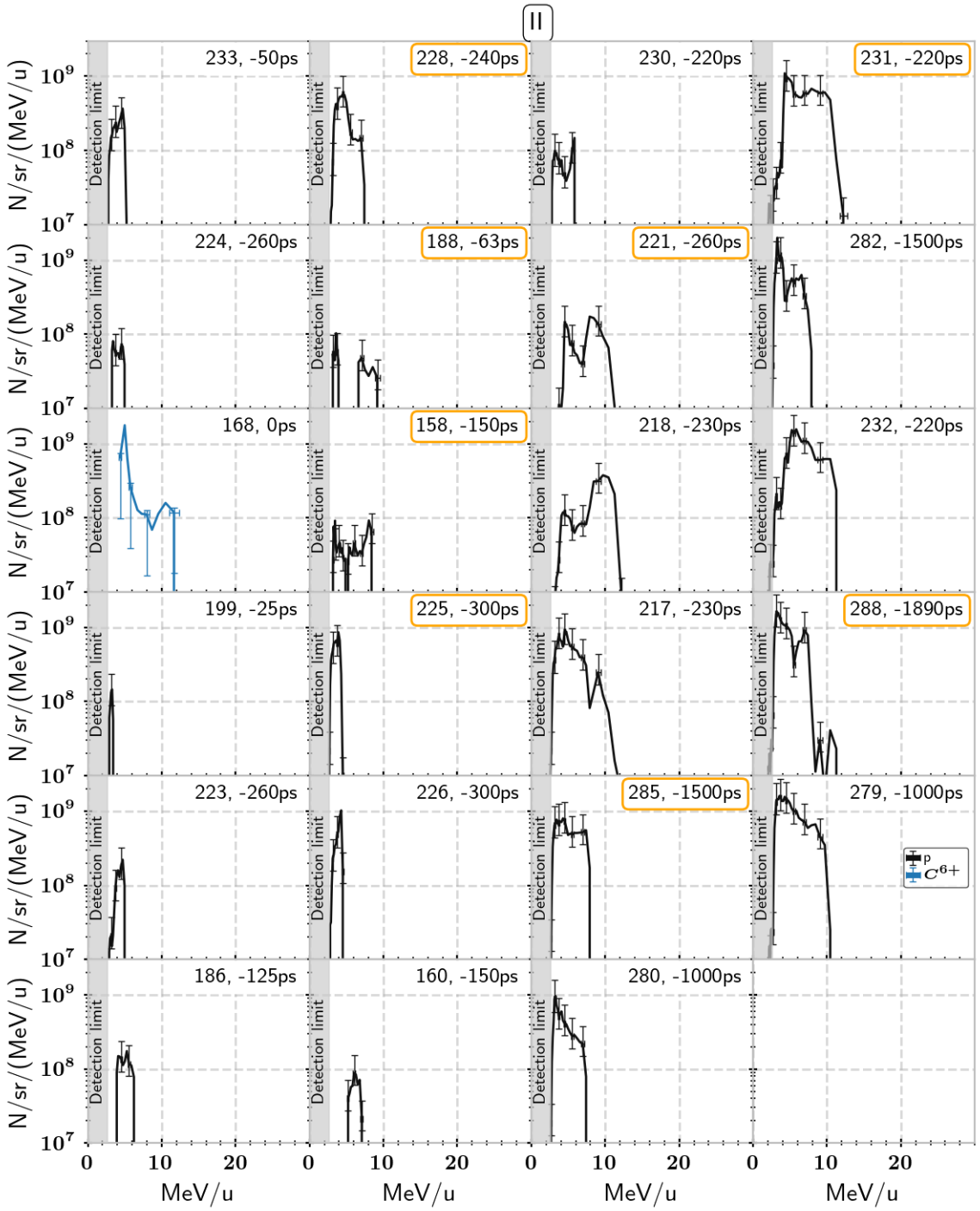

Fig. A.1. *| Shots that are in the area II of Fig. 4.6 (b). Shots are sorted column wise by increasing $r[n/n_c = 1]$. Except for shots 147 and 168 all shots solely show proton ions. Orange Boxes around the shotnumber indicate the best shots per delay setting.*

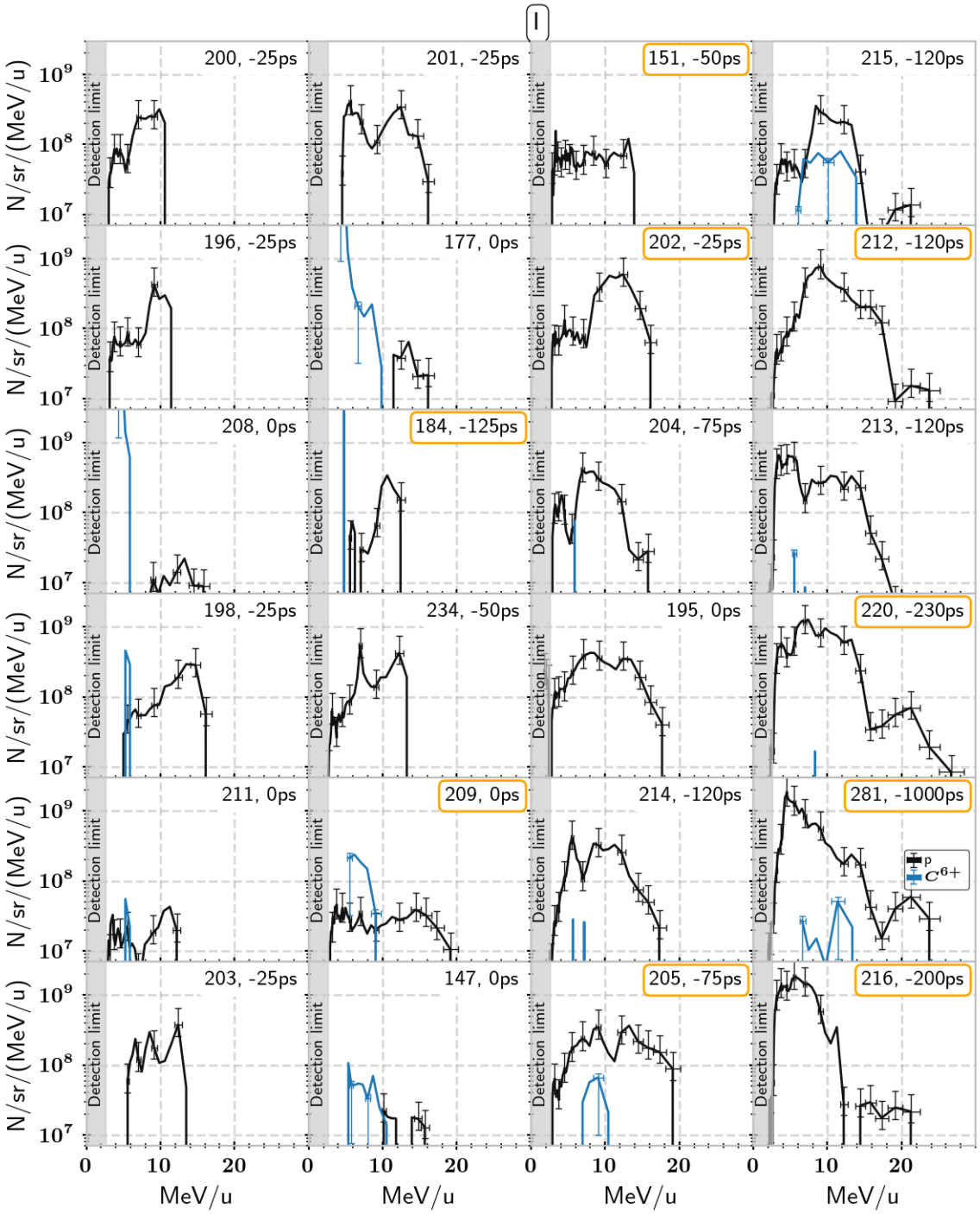

Fig. A.2. *I Shots that are in the area I of Fig. 4.6 (b). Shots are sorted column wise by increasing $r[n/n_c = 1]$. Especially the shots in excess of 20 MeV show an additional peak appearing. Shots are sorted column wise by increasing $r[n/n_c = 1]$. Orange Boxes around the shotnumber indicate the best shots per delay setting.*

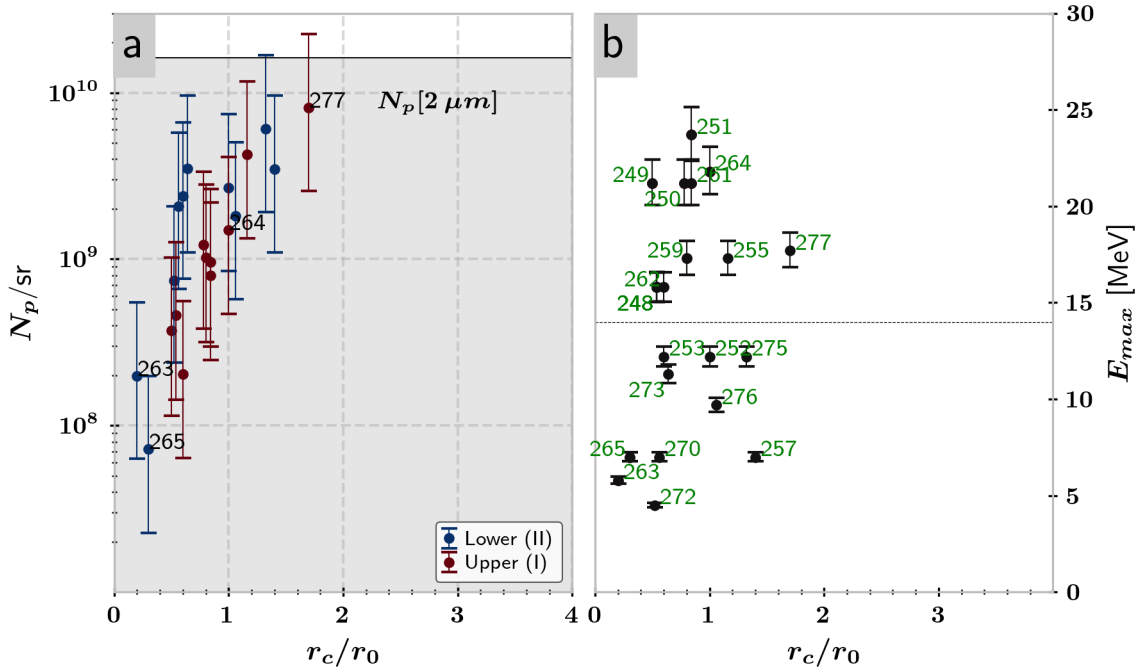

Fig. A.3. *I (a) shows the particle number against the ordering parameter. (b) shows the maximum cut-off energy against the ordering parameter per solid angle from experiment for a* 2 µm *spheres. The dashed line indicates the unperturbed target radius of* 1 µm*. In the maximum energy plot, the data can be split in two distinct areas. The numbers in the graph are the shot numbers corresponding to the best shots per delay setting. The vertical white interruption indicateas the point, where the central density starts decreasing.* r_c *>2.1 is the reduced density area. Best shots per delay setting are labeled with an orange dot.*

A.2. 2 µm spheres

The data set with 2 µm spheres contains 20 data points, of which 10 are shots on solid density spheres. The data was recorded on 4 days. For these shots the prepulse energy varied between 150 µJ and 100 µJ, yielding a peak intensity between $0.8 - 1.2 \cdot 10^{15}$W/cm^2.Fig. 4.6, shows the particle number against the ordering parameter (a) and the maximum proton energy against the ordering parameter (b). Compared to the 1 µm shots, for 2 µm we did not reach the reduced density interval ($r_c/r_0 > 2$ Especially we did not reach the reduced density area. Based on the maximum energy, we split the shots in two populations, with high and low cut-off energy, independent of the ordering parameter Fig. 4.6 (b). In terms of particle

numbers the 2 µm shots follow the same path as the 1 µm shots, and comparing the best shot with out pre-pulse to a shot with pre-pulse, the particle number increases by a factor 6, from $1.5 \cdot 10^{09}$ N/sr (shot 264) to $8.2 \cdot 10^{09}$ N/sr (shot 277). In terms of maximum proton energy, we see a decrease from 22 ± 2 MeV (264) to 17.7 ± 0.9 MeV (277). Carbon ions are only detected in the upper population, that also yielded higher proton energies. The proton spectra in this area seem to be dominated by a multi-species effect from the carbon ions, where parts of the proton spectrum are depopulated by the carbon ions. An example here is shot 277, where we detect carbons between 7.8 MeV/u and 11 MeV/u and the proton signal drops to the noise level between 8.2-9.8 MeV for the protons, see Fig. A.4.

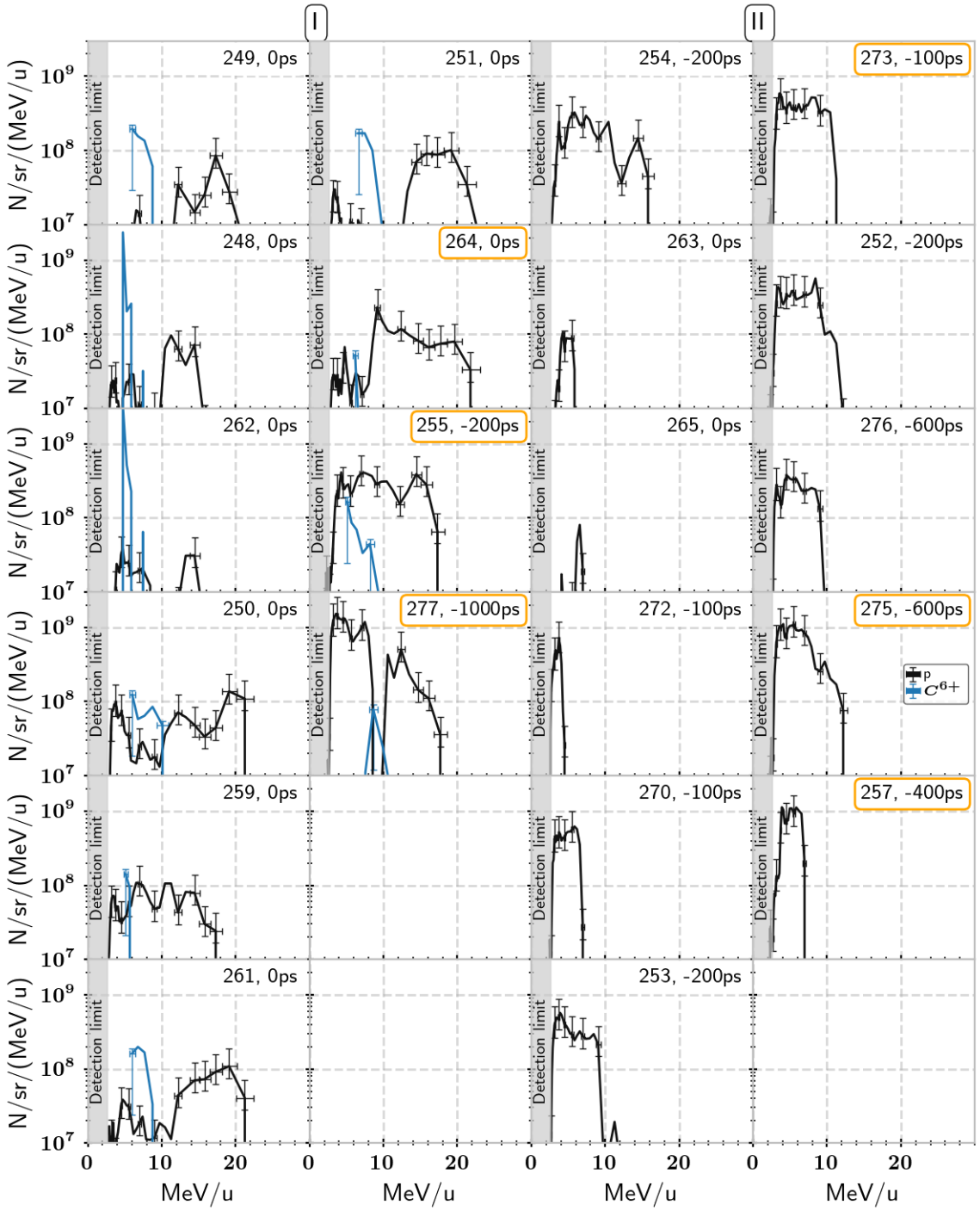

Fig. A.4. *| The left two columns are the shots in area I of Fig. 4.6 (d), where as the right two columns are shots in area II. Interestingly all shots on the high energetic branch show carbon ions in addition to the accelerated proton ions. Orange Boxes around the shotnumber indicate the best shots per delay setting.*

Bibliography

1. Henning, W. & Shank, C. *Accelerators for America's Future* 2010.
2. Hinterberger, F. in *Physik Der Teilchenbeschleuniger Und Ionenoptik* 211–238 (Springer Berlin Heidelberg, Berlin, Heidelberg, 2008). ISBN: 978-3-540-75282-0. doi:10.1007/978-3-540-75282-0_5.
3. Wideröe, R. Über ein neues Prinzip zur Herstellung hoher Spannungen. *Archiv f. Elektrotechnik* **21,** 387–406. ISSN: 0003-9039, 1432-0487. doi:10.1007/BF01656341 (July 1928).
4. Albert, F. *et al.* 2020 Roadmap on Plasma Accelerators. *New J. Phys.* **23,** 031101. ISSN: 1367-2630. doi:10.1088/1367-2630/abcc62 (Mar. 2021).
5. *Facts and Figures about the LHC | CERN* https://home.cern/resources/faqs/facts-and-figures-about-lhc.
6. Breuer, J. & Hommelhoff, P. Laser-Based Acceleration of Nonrelativistic Electrons at a Dielectric Structure. *Phys. Rev. Lett.* **111,** 134803. ISSN: 0031-9007, 1079-7114. doi:10.1103/PhysRevLett.111.134803 (Sept. 2013).
7. Maiman, T. H. Optical and Microwave-Optical Experiments in Ruby. *Phys. Rev. Lett.* **4,** 564–566. ISSN: 0031-9007. doi:10.1103/PhysRevLett.4.564 (June 1960).
8. Veksler, V. I. The Principle of Coherent Acceleration of Charged Particles. *The Soviet Journal of Atomic Energy* **2,** 525–528. ISSN: 1063-4258, 1573-8205. doi:10.1007/BF01491001 (Sept. 1957).
9. Strickland, D. & Mourou, G. Compression of Amplified Chirped Optical Pulses. *Optics Communications* **56,** 219–221. ISSN: 0030-4018. doi:10.1016/0030-4018(85)90120-8 (1985).
10. *The Nobel Prize in Physics 2018* https://www.nobelprize.org/prizes/physics/2018/.

11. Yanovsky, V. *et al.* Ultra-High Intensity- 300-TW Laser at 0.1 Hz Repetition Rate. 6 (2008).

12. Yoon, J. W. *et al.* Achieving the Laser Intensity of 5.5×10^{22} W/Cm^2 with a Wavefront-Corrected Multi-PW Laser. *Opt. Express, OE* **27,** 20412–20420. ISSN: 1094-4087. doi:10.1364/OE.27.020412 (July 2019).

13. Danson, C. N. *et al.* Petawatt and Exawatt Class Lasers Worldwide. *High Power Laser Science and Engineering* **7.** ISSN: 2095-4719, 2052-3289. doi:10.1017/hpl.2019.36 (2019).

14. Daido, H., Nishiuchi, M. & Pirozhkov, A. S. Review of Laser-Driven Ion Sources and Their Applications. *Rep. Prog. Phys.* **75,** 056401. ISSN: 0034-4885, 1361-6633. doi:10.1088/0034-4885/75/5/056401 (May 2012).

15. Snavely, R. A. *et al.* Intense High-Energy Proton Beams from Petawatt-Laser Irradiation of Solids. *Phys. Rev. Lett.* **85,** 2945–2948. ISSN: 0031-9007, 1079-7114. doi:10.1103/PhysRevLett.85.2945 (Oct. 2000).

16. Clark, E. L. *et al.* Energetic Heavy-Ion and Proton Generation from Ultraintense Laser-Plasma Interactions with Solids. *Phys. Rev. Lett.* **85,** 1654–1657. ISSN: 0031-9007, 1079-7114. doi:10.1103/PhysRevLett.85.1654 (Aug. 2000).

17. Yin, L., Albright, B. J., Hegelich, B. M. & Fernández, J. C. GeV Laser Ion Acceleration from Ultrathin Targets: The Laser Break-out Afterburner. *Laser Part. Beams* **24,** 291–298. ISSN: 0263-0346, 1469-803X. doi:10.1017/S0263034606060459 (June 2006).

18. Wagner, F. *et al.* Maximum Proton Energy above 85 MeV from the Relativistic Interaction of Laser Pulses with Micrometer Thick CH 2 Targets. *Phys. Rev. Lett.* **116,** 205002. ISSN: 0031-9007, 1079-7114. doi:10.1103/PhysRevLett.116.205002 (May 2016).

19. Higginson, A. *et al.* Near-100 MeV Protons via a Laser-Driven Transparency-Enhanced Hybrid Acceleration Scheme. *Nat Commun* **9,** 724. ISSN: 2041-1723. doi:10.1038/s41467-018-03063-9 (Dec. 2018).

20. Cowan, T. E. *et al.* Ultralow Emittance, Multi-MeV Proton Beams from a Laser Virtual-Cathode Plasma Accelerator. *Phys. Rev. Lett.* **92,** 204801. ISSN: 0031-9007, 1079-7114. doi:10.1103/PhysRevLett.92.204801 (May 2004).

21. Dromey, B. *et al.* Picosecond Metrology of Laser-Driven Proton Bursts. *Nat Commun* **7,** 10642. ISSN: 2041-1723. doi:10.1038/ncomms10642 (Apr. 2016).

22. Macchi, A., Borghesi, M. & Passoni, M. Ion Acceleration by Superintense Laser-Plasma Interaction. *Rev. Mod. Phys.* **85,** 751–793. ISSN: 0034-6861, 1539-0756. doi:10.1103/RevModPhys.85.751 (May 2013).

23. Barberio, M. *et al.* Laser-Accelerated Particle Beams for Stress Testing of Materials. *Nat Commun* **9,** 372. ISSN: 2041-1723. doi:10.1038/s41467-017-02675-x (Dec. 2018).

24. Ostermayr, T. M. *et al.* Laser-Driven x-Ray and Proton Micro-Source and Application to Simultaneous Single-Shot Bi-Modal Radiographic Imaging. *Nat Commun* **11,** 6174. ISSN: 2041-1723. doi:10.1038/s41467-020-19838-y (Dec. 2020).

25. Roth, M. *et al.* Fast Ignition by Intense Laser-Accelerated Proton Beams. *Phys. Rev. Lett.* **86,** 436–439. ISSN: 0031-9007, 1079-7114. doi:10.1103/PhysRevLett.86.436 (Jan. 2001).

26. Rösch, T. F. *et al.* A Feasibility Study of Zebrafish Embryo Irradiation with Laser-Accelerated Protons. *Review of Scientific Instruments* **91,** 063303. ISSN: 0034-6748, 1089-7623. doi:10.1063/5.0008512 (June 2020).

27. Linz, U. & Alonso, J. What Will It Take for Laser Driven Proton Accelerators to Be Applied to Tumor Therapy? *Phys. Rev. ST Accel. Beams* **10,** 094801. ISSN: 1098-4402. doi:10.1103/PhysRevSTAB.10.094801 (Sept. 2007).

28. Linz, U. & Alonso, J. Laser-Driven Ion Accelerators for Tumor Therapy Revisited. *Phys. Rev. Accel. Beams* **19,** 124802. ISSN: 2469-9888. doi:10.1103/PhysRevAccelBeams.19.124802 (Dec. 2016).

29. Chaudhary, P. *et al.* Radiobiology Experiments With Ultra-high Dose Rate Laser-Driven Protons: Methodology and State-of-the-Art. *Front. Phys.* **9,** 624963. ISSN: 2296-424X. doi:10.3389/fphy.2021.624963 (Apr. 2021).

30. Kroll, F. *et al.* Tumour Irradiation in Mice with a Laser-Accelerated Proton Beam. *Nat. Phys.* **18,** 316–322. ISSN: 1745-2473, 1745-2481. doi:10.1038/s41567-022-01520-3 (Mar. 2022).

31. Gibbon, P. *Short Pulse Laser Interactions with Matter: An Introduction* ISBN: 978-1-86094-135-1 (Imperial College Press, London, 2005).

32. McKenna, P. *et al.* Lateral Electron Transport in High-Intensity Laser-Irradiated Foils Diagnosed by Ion Emission. *Phys. Rev. Lett.* **98,** 145001. doi:10.1103/PhysRevLett.98.145001 (Apr. 2007).

33. Schwoerer, H. *et al.* Laser-Plasma Acceleration of Quasi-Monoenergetic Protons from Microstructured Targets. *Nature* **439,** 445–448. ISSN: 0028-0836, 1476-4687. doi:10.1038/nature04492 (Jan. 2006).

34. Karsch, S. *et al.* High-Intensity Laser Induced Ion Acceleration from Heavy-Water Droplets. *Phys. Rev. Lett.* **91,** 015001. ISSN: 0031-9007, 1079-7114. doi:10.1103/PhysRevLett.91.015001 (July 2003).

35. Sokollik, T. *et al.* Directional Laser-Driven Ion Acceleration from Microspheres. *Phys. Rev. Lett.* **103,** 135003. doi:10.1103/PhysRevLett.103.135003 (Sept. 2009).

36. Becker, G. A. *et al.* Characterization of Laser-Driven Proton Acceleration from Water Microdroplets. *Sci Rep* **9,** 17169. ISSN: 2045-2322. doi:10.1038/s41598-019-53587-3 (Dec. 2019).

37. Fukuda, Y. *et al.* Energy Increase in Multi-MeV Ion Acceleration in the Interaction of a Short Pulse Laser with a Cluster-Gas Target. *Phys. Rev. Lett.* **103,** 165002. ISSN: 0031-9007, 1079-7114. doi:10.1103/PhysRevLett.103.165002 (Oct. 2009).

38. Henig, A. *et al.* Laser-Driven Shock Acceleration of Ion Beams from Spherical Mass-Limited Targets. *Phys. Rev. Lett.* **102,** 095002. ISSN: 0031-9007, 1079-7114. doi:10.1103/PhysRevLett.102.095002 (Mar. 2009).

39. Paul, W. Electromagnetic Traps for Charged and Neutral Particles. *Rev. Mod. Phys.* **62,** 531–540. ISSN: 0034-6861, 1539-0756. doi:10.1103/RevModPhys.62.531 (July 1990).

40. Sokollik, T. *et al.* Laser-Driven Ion Acceleration Using Isolated Mass-Limited Spheres. *New J. Phys.* **12,** 113013. ISSN: 1367-2630. doi:10.1088/1367-2630/12/11/113013 (Nov. 2010).

41. Ostermayr, T. M. *et al.* A Transportable Paul-trap for Levitation and Accurate Positioning of Micron-Scale Particles in Vacuum for Laser-Plasma Experiments. *Review of Scientific Instruments* **89,** 013302. ISSN: 0034-6748, 1089-7623. doi:10.1063/1.4995955 (Jan. 2018).

42. Ostermayr, T. M. *et al.* Proton Acceleration by Irradiation of Isolated Spheres with an Intense Laser Pulse. *Phys. Rev. E* **94,** 033208. ISSN: 2470-0045, 2470-0053. doi:10.1103/PhysRevE.94.033208 (Sept. 2016).

43. Hilz, P. *et al.* Isolated Proton Bunch Acceleration by a Petawatt Laser Pulse. *Nat Commun* **9,** 423. ISSN: 2041-1723. doi:10.1038/s41467-017-02663-1 (Dec. 2018).

44. Sgattoni, A., Londrillo, P., Macchi, A. & Passoni, M. Laser Ion Acceleration Using a Solid Target Coupled with a Low-Density Layer. *PHYSICAL REVIEW E,* 9 (2012).

45. Bhagawati, A. & Das, N. Laser-Accelerated Protons Using Density Gradients in Hydrogen Plasma Spheres. *J. Plasma Phys.* **87,** 905870413. ISSN: 0022-3778, 1469-7807. doi:10.1017/S0022377821000817 (Aug. 2021).

46. Stockem Novo, A., Kaluza, M. C., Fonseca, R. A. & Silva, L. O. Optimizing Laser-Driven Proton Acceleration from Overdense Targets. *Sci Rep* **6,** 29402. ISSN: 2045-2322. doi:10.1038/srep29402 (Sept. 2016).

47. Fiuza, F. *et al.* Laser-Driven Shock Acceleration of Monoenergetic Ion Beams. *Phys. Rev. Lett.* **109,** 215001. ISSN: 0031-9007, 1079-7114. doi:10.1103/PhysRevLett.109.215001 (Nov. 2012).

48. Chen, F. F. *Introduction to Plasma Physics and Controlled Fusion* ISBN: 978-3-319-22309-4. doi:10.1007/978-3-319-22309-4 (Springer International Publishing, Cham, 2016).

49. Macchi, A. *A Superintense Laser-Plasma Interaction Theory Primer* ISBN: 978-94-007-6124-7 978-94-007-6125-4. doi:10.1007/978-94-007-6125-4 (Springer Netherlands, Dordrecht, 2013).

50. Kiefer, D. *Relativistic Electron Mirrors from High Intensity Laser Nanofoil Interactions* PhD thesis (LMU Munich, Munich, 2012).

51. Griffiths, D. J. *Introduction to Electrodynamics* 3rd ed. ISBN: 978-0-13-805326-0 (Prentice Hall, Upper Saddle River, N.J, 1999).

52. Haffa, D. *et al.* Temporally Resolved Intensity Contouring (TRIC) for Characterization of the Absolute Spatio-Temporal Intensity Distribution of a Relativistic, Femtosecond Laser Pulse. *Sci Rep* **9,** 7697. ISSN: 2045-2322. doi:10.1038/s41598-019-42683-z (Dec. 2019).

53. Wilks, S. C., Kruer, W. L., Tabak, M. & Langdon, A. B. Absorption of Ultra-Intense Laser Pulses. *Phys. Rev. Lett.* **69,** 1383–1386. ISSN: 0031-9007. doi:10.1103/PhysRevLett.69.1383 (Aug. 1992).

54. Pirozhkov, A. S. *et al.* Approaching the Diffraction-Limited, Bandwidth-Limited Petawatt. *Opt. Express* **25,** 20486. ISSN: 1094-4087. doi:10.1364/OE.25.020486 (Aug. 2017).

55. Bin, J. H. *et al.* Ion Acceleration Using Relativistic Pulse Shaping in Near-Critical-Density Plasmas. *Phys. Rev. Lett.* **115,** 064801. ISSN: 0031-9007, 1079-7114. doi:10.1103/PhysRevLett.115.064801 (Aug. 2015).

56. McKenna, P. *Laser-Plasma Interactions and Applications* ISBN: 978-3-319-00037-4 (Springer, New York, 2013).

57. Wilks, S. & Kruer, W. Absorption of Ultrashort, Ultra-Intense Laser Light by Solids and Overdense Plasmas. *IEEE J. Quantum Electron.* **33,** 1954–1968. ISSN: 00189197. doi:10.1109/3.641310 (1997).

58. Brunel, F. Not-so-Resonant, Resonant Absorption. *Phys. Rev. Lett.* **59,** 52–55. ISSN: 0031-9007. doi:10.1103/PhysRevLett.59.52 (July 1987).

59. Kruer, W. L. & Estabrook, K. J×B Heating by Very Intense Laser Light. *Physics of Fluids* **28,** 430–432. ISSN: 0031-9171. doi:10.1063/1.865171 (Jan. 1985).

60. Roth, M. & Schollmeier, M. Ion Acceleration—Target Normal Sheath Acceleration. *CERN Yellow Reports,* 231 Pages. doi:10.5170/CERN-2016-001.231 (Feb. 2016).

61. Wilks, S. C., Langdon, A. B. & Cowan, T. E. Energetic Proton Generation in Ultra-Intense Laser–Solid Interactions. *Phys. Plasmas* **8,** 9 (2001).

62. Schreiber, J. *et al.* Analytical Model for Ion Acceleration by High-Intensity Laser Pulses. *Phys. Rev. Lett.* **97,** 045005. ISSN: 0031-9007, 1079-7114. doi:10.1103/PhysRevLett.97.045005 (July 2006).

63. Fuchs, J. *et al.* Laser-Driven Proton Scaling Laws and New Paths towards Energy Increase. *Nature Phys* **2,** 48–54. ISSN: 1745-2473, 1745-2481. doi:10.1038/nphys199 (Jan. 2006).

64. Esirkepov, T., Borghesi, M., Bulanov, S. V., Mourou, G. & Tajima, T. Highly Efficient Relativistic-Ion Generation in the Laser-Piston Regime. *Phys. Rev. Lett.* **92,** 175003. ISSN: 0031-9007, 1079-7114. doi:10.1103/PhysRevLett.92.175003 (Apr. 2004).

65. Henig, A. *et al.* Radiation-Pressure Acceleration of Ion Beams Driven by Circularly Polarized Laser Pulses. *Phys. Rev. Lett.* **103,** 245003. ISSN: 0031-9007, 1079-7114. doi:10.1103/PhysRevLett.103.245003 (Dec. 2009).

66. Yin, L. *et al.* Three-Dimensional Dynamics of Breakout Afterburner Ion Acceleration Using High-Contrast Short-Pulse Laser and Nanoscale Targets. *Phys. Rev. Lett.* **107,** 045003. ISSN: 0031-9007, 1079-7114. doi:10.1103/PhysRevLett.107.045003 (July 2011).

67. Yu, W. *et al.* Direct Acceleration of Solid-Density Plasma Bunch by Ultraintense Laser. *Phys. Rev. E* **72,** 046401. ISSN: 1539-3755, 1550-2376. doi:10.1103/PhysRevE.72.046401 (Oct. 2005).

68. Hilz, P. *Volumetric Laser Ion Acceleration* PhD thesis (LMU Munich, München, 2020).

69. Macchi, A., Cattani, F., Liseykina, T. V. & Cornolti, F. Laser Acceleration of Ion Bunches at the Front Surface of Overdense Plasmas. *Phys. Rev. Lett.* **94,** 165003. ISSN: 0031-9007, 1079-7114. doi:10.1103/PhysRevLett.94.165003 (Apr. 2005).

70. Macchi, A., Veghini, S. & Pegoraro, F. "Light Sail" Acceleration Reexamined. *Phys. Rev. Lett.* **103,** 085003. doi:10.1103/PhysRevLett.103.085003 (Aug. 2009).

71. Yan, X. Q. *et al.* Generating High-Current Monoenergetic Proton Beams by a CircularlyPolarized Laser Pulse in the Phase-StableAcceleration Regime. *Phys. Rev. Lett.* **100,** 135003. ISSN: 0031-9007, 1079-7114. doi:10.1103/PhysRevLett.100.135003 (Apr. 2008).

72. Ostermayr, T. *Relativistically Intense Laser–Microplasma Interactions* ISBN: 978-3-030-22207-9 978-3-030-22208-6. doi:10.1007/978-3-030-22208-6 (Springer International Publishing, Cham, 2019).

73. Schlegel, T. *et al.* Relativistic Laser Piston Model: Ponderomotive Ion Acceleration in Dense Plasmas Using Ultraintense Laser Pulses. *Physics of Plasmas* **16,** 083103. ISSN: 1070-664X, 1089-7674. doi:10.1063/1.3196845 (Aug. 2009).

74. Robinson, A. P. L. *et al.* Relativistically Correct Hole-Boring and Ion Acceleration by Circularly Polarized Laser Pulses. *Plasma Phys. Control. Fusion* **51,** 024004. ISSN: 0741-3335, 1361-6587. doi:10.1088/0741-3335/51/2/024004 (Feb. 2009).

75. Weng, S. *et al.* Optimization of Hole-Boring Radiation Pressure Acceleration of Ion Beams for Fusion Ignition. *Matter and Radiation at Extremes* **3,** 28–39. ISSN: 2468080X. doi:10.1016/j.mre.2017.09.002 (Jan. 2018).

76. Major, F. G., Gheorghe, V. N. & Werth, G. *Charged Particle Traps: Physics and Techniques of Charged Particle Field Confinement Springer Series on Atomic, Optical, and Plasma Physics* **37.** ISBN: 978-3-540-22043-5 (Springer, Berlin ; New York, 2005).

77. Werth, G., Gheorghe, V. N. & Major, F. G. *Charged Particle Traps II* ISBN: 978-3-540-92260-5 978-3-540-92261-2. doi:10.1007/978-3-540-92261-2 (Springer Berlin Heidelberg, Berlin, Heidelberg, 2009).

78. Earnshaw, S. On the Nature of the Molecular Forces Which Regulate the Constitution of the Luminiferous Ether. *Transactions of the Cambridge Philosophical Society* **7,** 97 (1848).

79. Denison, D. R. Operating Parameters of a Quadrupole in a Grounded Cylindrical Housing. *Journal of Vacuum Science and Technology* **8,** 266–269. ISSN: 0022-5355. doi:10.1116/1.1316304 (Jan. 1971).

80. Alheit, R., Enders, K. & Werth, G. Isotope Separation by Nonlinear Resonances in a Paul Trap. *Appl. Phys. B* **62,** 511–513. ISSN: 0946-2171, 1432-0649. doi:10.1007/BF01081052 (May 1996).

81. *microParticles Onlineshop* https://www.microparticles-shop.de/.

82. *tectra* https://tectra.de/.

83. *Arduino Uno Rev3* http://store.arduino.cc/products/arduino-uno-rev3.

84. *Home - TANGO Controls* https://www.tango-controls.org/.

85. Cermak, I. *Laboruntersuchung Elektrischer Aufladung Kleiner Staubteilchen* PhD thesis (Ruprecht-Karls-Universität, Heidelberg, 1994).

86. Drewsen, M. & Brøner, A. Harmonic Linear Paul Trap: Stability Diagram and Effective Potentials. *Phys. Rev. A* **62,** 045401. ISSN: 1050-2947, 1094-1622. doi:10.1103/PhysRevA.62.045401 (Sept. 2000).

87. Dahl, D. A. Simion for the Personal Computer in Reflection. *International Journal of Mass Spectrometry* **200,** 3–25. ISSN: 13873806. doi:10.1016/S1387-3806(00)00305-5 (Dec. 2000).

88. Speicher, M. *Optical Probing of Laser-induced Expansion of Levitating Mcrospheres* PhD thesis (LMU Munich, Munich, 2022).

89. Oksenhendler, T. *et al.* Self-Referenced Spectral Interferometry. *Appl. Phys. B* **99,** 7–12. ISSN: 0946-2171, 1432-0649. doi:10.1007/s00340-010-3916-y (Apr. 2010).

90. Kapteyn, H. C., Szoke, A., Falcone, R. W. & Murnane, M. M. Prepulse Energy Suppression for High-Energy Ultrashort Pulses Using Self-Induced Plasma Shuttering. *Opt. Lett.* **16,** 490. ISSN: 0146-9592, 1539-4794. doi:10.1364/OL.16.000490 (Apr. 1991).

91. Ziener, C. *et al.* Specular Reflectivity of Plasma Mirrors as a Function of Intensity, Pulse Duration, and Angle of Incidence. *Journal of Applied Physics* **93,** 768–770. ISSN: 0021-8979, 1089-7550. doi:10.1063/1.1525062 (Jan. 2003).

92. Dromey, B., Kar, S., Zepf, M. & Foster, P. The Plasma Mirror—A Subpicosecond Optical Switch for Ultrahigh Power Lasers. *Review of Scientific Instruments* **75,** 645–649. ISSN: 0034-6748, 1089-7623. doi:10.1063/1.1646737 (Mar. 2004).

93. Poole, P. L. *et al.* Experiment and Simulation of Novel Liquid Crystal Plasma Mirrors for High Contrast, Intense Laser Pulses. *Sci Rep* **6,** 32041. ISSN: 2045-2322. doi:10.1038/srep32041 (Aug. 2016).

94. Speicher, M. *et al.* Integrated Double-Plasma-Mirror Targets for Contrast Enhancement in Laser Ion Acceleration. *J. Phys.: Conf. Ser.* **1079,** 012002. ISSN: 1742-6588, 1742-6596. doi:10.1088/1742-6596/1079/1/012002 (Aug. 2018).

95. Obst, L. *et al.* On-Shot Characterization of Single Plasma Mirror Temporal Contrast Improvement. *Plasma Physics and Controlled Fusion* **60,** 054007 (2018).

96. Jung, D. *et al.* A Novel High Resolution Ion Wide Angle Spectrometer. *Review of Scientific Instruments* **82,** 043301. ISSN: 0034-6748, 1089-7623. doi:10.1063/1.3575581 (Apr. 2011).

97. Tipler, P. A. & Mosca, G. *Physik für Wissenschaftler und Ingenieure* 7. deutsche Auflage (ed Wagner, J.) trans. by Basler, M., Dohmen, R., Heinisch, C., Schleitzer, A. & Zillgitt, M. ISBN: 978-3-642-54165-0 978-3-642-54166-7 (Springer Spektrum, Berlin Heidelberg, 2015).

98. Ziegler, J. F., Ziegler, M. & Biersack, J. SRIM – The Stopping and Range of Ions in Matter (2010). *Nuclear Instruments and Methods in Physics Research Section B: Beam Interactions with Materials and Atoms* **268,** 1818–1823. ISSN: 0168583X. doi:10.1016/j.nimb.2010.02.091 (June 2010).

99. Camacho, J. M. & Sosa, V. Alternative Method to Calculate the Magnetic Field of Permanent Magnets with Azimuthal Symmetry. *Rev. Mex. Fis. E,* 10 (2013).

100. Reinhardt, S. *Detection of Laser–Accelerated Protons* PhD thesis ().

101. Morrison, J. T. *Selective Deuteron Acceleration Using Target Normal Sheath Acceleration* PhD thesis (The Ohio State University, 2013).

102. Mančić, A., Fuchs, J., Antici, P., Gaillard, S. A. & Audebert, P. Absolute Calibration of Photostimulable Image Plate Detectors Used as (0.5–20MeV) High-Energy Proton Detectors. *Review of Scientific Instruments* **79,** 073301. ISSN: 0034-6748, 1089-7623. doi:10.1063/1.2949388 (July 2008).

103. Doria, D. *et al.* Calibration of BAS-TR Image Plate Response to High Energy (3-300 MeV) Carbon Ions. *Review of Scientific Instruments* **86,** 123302. ISSN: 0034-6748, 1089-7623. doi:10.1063/1.4935582 (Dec. 2015).

104. Alejo, A. *et al.* Characterisation of Deuterium Spectra from Laser Driven Multi-Species Sources by Employing Differentially Filtered Image Plate Detectors in Thomson Spectrometers. *Review of Scientific Instruments* **85,** 093303. ISSN: 0034-6748, 1089-7623. doi:10.1063/1.4893780 (Sept. 2014).

105. Bethe, H. Zur Theorie des Durchgangs schneller Korpuskularstrahlen durch Materie. *Ann. Phys.* **397,** 325–400. ISSN: 00033804, 15213889. doi:10.1002/andp.19303970303 (1930).

106. Ditmire, T., Donnelly, T., Rubenchik, A. M., Falcone, R. W. & Perry, M. D. Interaction of Intense Laser Pulses with Atomic Clusters. *Phys. Rev. A* **53,** 3379–3402. ISSN: 1050-2947, 1094-1622. doi:10.1103/PhysRevA.53.3379 (May 1996).

107. Anand, M., Gibbon, P. & Krishnamurthy, M. Laser Absorption in Microdroplet Plasmas. *Europhys. Lett.* **80,** 25002. ISSN: 0295-5075, 1286-4854. doi:10.1209/0295-5075/80/25002 (Oct. 2007).

108. Hartmann, J. *et al.* The Spatial Contrast Challenge for Intense Laser-Plasma Experiments. *J. Phys.: Conf. Ser.* **1079,** 012003. ISSN: 1742-6588, 1742-6596. doi:10.1088/1742-6596/1079/1/012003 (Aug. 2018).

109. Henig, A. *et al.* Enhanced Laser-Driven Ion Acceleration in the Relativistic Transparency Regime. *Phys. Rev. Lett.* **103,** 045002. ISSN: 0031-9007, 1079-7114. doi:10.1103/PhysRevLett.103.045002 (July 2009).

110. Yan, X. Q., Tajima, T., Hegelich, M., Yin, L. & Habs, D. Theory of Laser Ion Acceleration from a Foil Target of Nanometer Thickness. *Appl. Phys. B* **98,** 711–721. ISSN: 0946-2171, 1432-0649. doi:10.1007/s00340-009-3707-5 (Mar. 2010).

111. Dawson, J. M. Particle Simulation of Plasmas. *Rev. Mod. Phys.* **55,** 403–447. ISSN: 0034-6861. doi:10.1103/RevModPhys.55.403 (Apr. 1983).

112. Tskhakaya, D., Matyash, K., Schneider, R. & Taccogna, F. The Particle-In-Cell Method. *Contrib. Plasma Phys.* **47,** 563–594. ISSN: 08631042, 15213986. doi:10.1002/ctpp.200710072 (Dec. 2007).

113. Jülich Supercomputing Centre. JUWELS Cluster and Booster: Exascale Pathfinder with Modular Supercomputing Architecture at Juelich Supercomputing Centre. *Journal of large-scale research facilities* **7.** doi:10.17815/jlsrf-7-183 (2021).

114. Derouillat, J. *et al.* SMILEI: A Collaborative, Open-Source, Multi-Purpose Particle-in-Cell Code for Plasma Simulation. *Computer Physics Communications* **222,** 351–373. ISSN: 00104655. doi:10.1016/j.cpc.2017.09.024 (Jan. 2018).

115. Esirkepov, T. Z., Kato, Y. & Bulanov, S. V. Bow Wave from Ultraintense Electromagnetic Pulses in Plasmas. *Phys. Rev. Lett.* **101,** 265001. ISSN: 0031-9007, 1079-7114. doi:10.1103/PhysRevLett.101.265001 (Dec. 2008).

116. Kar, S. *et al.* Ion Acceleration in Multispecies Targets Driven by Intense Laser Radiation Pressure. *Phys. Rev. Lett.* **109,** 185006. ISSN: 0031-9007, 1079-7114. doi:10.1103/PhysRevLett.109.185006 (Nov. 2012).

117. Steinke, S. *et al.* Stable Laser-Ion Acceleration in the Light Sail Regime. *Phys. Rev. ST Accel. Beams* **16,** 011303. ISSN: 1098-4402. doi:10.1103/PhysRevSTAB.16.011303 (Jan. 2013).

118. Huebl, A. *et al.* Spectral Control via Multi-Species Effects in PW-class Laser-Ion Acceleration. *Plasma Phys. Control. Fusion* **62,** 124003. ISSN: 0741-3335, 1361-6587. doi:10.1088/1361-6587/abbe33 (Dec. 2020).

119. Matsui, R., Fukuda, Y. & Kishimoto, Y. Quasimonoenergetic Proton Bunch Acceleration Driven by Hemispherically Converging Collisionless Shock in a Hydrogen Cluster Coupled with Relativistically Induced Transparency. *Physical Review Letters* **122.** doi:10.1103/physrevlett.122.014804 (Jan. 2019).

120. Naumova, N. *et al.* Hole Boring in a DT Pellet and Fast-Ion Ignition with Ultraintense Laser Pulses. *Phys. Rev. Lett.* **102,** 025002. ISSN: 0031-9007, 1079-7114. doi:10.1103/PhysRevLett.102.025002 (Jan. 2009).

Abbreviations

AR	Anti Reflection
ASE	Amplified Spontaneous Emission
CALA	Centre for Advanced Laser Applications
CCD	Charge Coupled Device
CPA	Chirped Pulse Amplification
FWHM	Full Width at Half Maximum
HB	Hole Boring
HDR	High Dynamic Range
HIJ	Helmholtz Institue Jena
IP	Image Plates, BAS-TR
iWASP	Ion Wide Angle Spectrometer
JETi 200	Jenaer Titanium:Sapphire 200 Terawatt Laser System
LDR	Low Dynamic Range
OAP	Off-axis Parabolic Mirror
PHELIX	Petawatt Hoch-Energie Laser für Schwerionenexperimente
PIC	Particle-in-Cell
PMMA	Polymethylmethacrylat ($C_5H_8O_2$)
PS	Polystyrene (C_8H_8)
PSL	Photo Stimulated Luminescence
RPA	Radiation Pressure Acceleration
TCC	Target Chamber Center
Ti:Sa	Titanium Sapphire
TNSA	Target Normal Sheath Acceleration
TPW	Texas Petawatt Laser
XPW	Cross-polarized wave
ZEUS	Zinth's extremely useful superlaser

List of Figures

Peer-Reviewed Publications

1. F. Lindner, D. Haffa, J. H. Bin, F. Englbrecht, Y. Gao, **J. Gebhard**, J. Hartmann, P. Hilz, C. Kreuzer, S. Lehrack, T. Ostermayr, T. Rösch, M. Speicher, M. Würl, K. Parodi, J. Schreiber, and P. Thirolf. *"Towards swift ion bunch acceleration by high-power laser pulses at the center for advanced laser applications (CALA)."* Nuclear Instruments and Methods in Physics Research Section B: Beam Interactions with Materials and Atoms 402, 354-357 (2017)

2. P. Hilz, T.M. Ostermayr, A. Huebl, V. Bagnoud, B. Borm, M. Bussmann, M.Gallei, **J. Gebhard**, D. Haffa, J. Hartmann, T. Kluge, F.H. Lindner, P. Neumayr, C.G. Schaefer, U. Schramm, P.G. Thirolf, T.F. Rösch, F. Wagner, B. Zielbauer, J. Schreiber. *"Isolated Proton Bunch Acceleration by a Peta-Watt Laser Pulse."* Nature Communications 9(1), 423 (2018)

3. T. M. Ostermayr, **J. Gebhard**, D. Haffa, D. Kiefer, C. Kreuzer, K. Allinger, C. Bömer, J. Braenzel, M. Schnürer, I. Cermak, J. Schreiber and P. Hilz, *"A transportable Paul-trap for levitation and accurate positioning of micron-scale particles in vacuum for laser-plasma experiments"*, Review of Scientific Instruments 89, 013302 (2018).

4. D. Haffa, R. Yang, J.H. Bin, S. Lehrack, H. Ding, F.S. Englbrecht, Y. Gao, **J. Gebhard**, J. Goetzfried, M. Gilljohann, J. Hartmann, S. Herr, P. Hilz, C. Kreuzer, F.H. Lindner, E. Ridente, T.F. Rösch, G. Schilling, M. Speicher, D. Taray, T.M. Ostermayr, M. Würl, W. Assmann, S. Karsch, K. Parodi, J. Schreiber, *"I-BEAT: Ultrasonic method for online measurement of the energy distribution of a single ion bunch"* Scientific Reports 9, 6714 (2019)

5. T. M. Ostermayr, C. Kreuzer, F. S. Englbrecht, **J. Gebhard**, J. Hartmann, A. Huebl, D. Haffa, P. Hilz, K. Parodi, J. Wenz, M. E. Donovan, G. Dyer, E. Gaul, J. Gordon, M. Martinez, E. Mccary, M. Spinks, G. Tiwari, B. M. Hegelich and J. Schreiber, *"Laser-driven x-ray and proton micro-source and application to simultaneous single-shot bi-modal radiographic imaging"*. Nat Commun 11, 6174 (2020).

Conference Contributions

1. **Poster:** A Paul Trap for isolated targets at High-power laser systems, European Advanced Accelerators Concepts, Elba,Italy (2017)

2. **Oral:** Truly isolated Targets for High Power Lasers using a Paul Trap, Target Fabrication workshop, Darmstadt, Germany(2018)

3. **Oral:** Coherent proton acceleration from isolated micro-plasmas, EPS (2018)

4. **Invited:** Individually Isolated Targets for High Power Lasers Using a Paul Trap, Targ4, Milano, Italy (2019)

5. **Oral:** Fully Isolated Targets for High Power Laser Interaction applying a Paul Trap, Targ5, Dresden, Germany (2022)

Danksagung

Zu guter Letzt möchte ich die Möglichkeit zu einem großen DANKE ergreifen, und all jenen Personen danken, die diese Arbeit erst ermöglicht haben, und mich durch alle Höhen und Tiefen begleitet haben.
Mein besonderer Dank gilt Jörg Schreiber für die Bereitstellung der notwendigen Ressourcen für diese Dissertation, die Betreuung, die Diskussionen, die Zusammenarbeit und das in mich gesetzte Vertrauen in den letzten Jahren. Mein Dank gilt hier auch an Tobias Ostermayr und Peter Hilz, die mich ursprüglich in die "Falle" gelockt haben und mich sehr gut in die Gruppe aufgenommen haben. Mit der Paul Falle habt ihr mir ein einzigartiges Experiment zur Weiterarbeit überlassen. Die beiden experimentellen Kampagnen am PHELIX Laser in Darmstadt und am Texas Pett-Watt in Austin, Texas waren besondere Highlights während meiner Masterarbeit. Euch auch vielen Dank für die Diskussionen über die Paul-Falle auch über die Zeit der Masterarbeit hinaus. Besonders möchte ich mich bei Peter Hilz zudem bedanken, dass er mir die Tore zum JETi laser geöffnet hat und die hier präsentierte Studie in langen Nächten mit mir zusammen durchgeführt hat. In diesem Zusammenhang gilt mein Dank hier Matt Zepf, der uns die notwendige Zeit in Target 2 verschafft hat um alle Herausforderungen zu lösen, die mit der Inbetriebnahme eines neuen Experimentierbereichs in Kombination mit einem sehr komplexen Experiment einhergehen. Ohne die herausragende Unterstützung beim Betrieb des JETi Lasers durch Alexander Sävert und Georg Schäfer, wäre das Experiment nicht zu schaffen gewesen. Auch hierfür mein herzlicher Dank.
Vielen Dank an Rolf Öhm, Stefan Rößl und das Team der mechanischen Werkstatt. Von euch durfte ich viel lernen, wenn mir wieder die wildesten Gedanken über technische Bauteile durch den Kopf spukten. Ohne eure fachmännische Unterstützung wären viele Aufbauten nicht realisierbar gewesen. Vielen Dank auch an Johann Krapfl und die elektronische Werkstatt für die kompetente Unterstützung bei der Automatisierung des experimentellen Setups.
Außerdem möchte mich bei Katharina Adler, Martin Groß und Hans Wirth bedanken für den verwaltungstechnische und technische Unterstützung beim Aufbau des Zeus-Labors. Mein Dank gilt auch Andrea Leinthaler, die als gute Seele der LS Parodi den Laden am Laufen hält.
Mein Dank geht auch an Johannes Götzfried, Max Gilljohann und Stefan Karsch für die Unterstützung und Beratung bei der Inbetriebnahme des Zeus-Labors und des Lasersystems. Mein Dank gilt auch den CALA-Special forces, Oliver Gosau,

Nik Gjotev und Florian Saran. Es war mir immer eine große Freude mit euch über Vakuum, Spiegel, Wasserlecks, oder das lebende Ultraschallbad zu diskutieren. In diesem Zuge auch herrlichen Dank an Felix Rauscher, der immer dafür gesorgt hat, dass die Daten frei fließen können.
Vielen Dank an die Studenten, die ich während meiner Arbeit betreuen durfte. Hier sind besonders mein einziger Bachelorstudent Sebastian Kiesser und meine Masterstudenten Felix Balling, Joey Kalis und Nils Weiße zu nennen. Euer Beitrag hat die jeweiligen Experimente deutlich voran gebracht. Vielen Dank auch an die drei studentischen Hilfskräfte, Michael Härtl, Franz Wolf und Markus Stein, mit denen ich zusammen einen vakuumtauglichen Positioniertisch entwickelt habe. Mein Dank gilt auch den Lektoren dieser Arbeit.
Besonderer Dank gilt auch an die Co-Doktoranden, Felix Balling, Leonard Doyle, Jens Hartmann, Christian Kreuzer, Daniel Haffa, Franz Englbrecht, Tobias Ostermayr, Peter Hilz, Sonja Gerlach, Lianren He, Ying Gao, Martin Speicher, Florian Lindner und Thomas Rösch, die meine Zeit in Garching immer zu eine großen Freude gemacht haben, sodass ich jeden Tag gern nach Garching gekommen bin. Vielen Dank an meinen Bürokollegen Thomas Rösch, es war mir eine große Ehre für diese besondere Lebensphase das Büro mit einen guten Freund teilen zu dürfen. Vielen Dank an den Durch-die-Wand-Bürokollegen Florian Linder mit den Kaffee-Pausen in Franz's Büro hat sich hier eine sehr besondere Freundschaft entwickelt. Zudem auch besonderen Dank an Martin Speicher für die lange Zusammenarbeit bei den Experimenten am Zeus-laser, die es zwar nicht in diese Arbeit geschafft haben, aber um so besser in deiner Arbeit präsentiert werden. Ich hab mich immer darauf gefreut auf den gemeinsamen Radl-Fahrten über alle möglichen Themen zu diskutieren.
Vielen Dank an die Studienstiftung des deutschen Volkes, die mich für mehr als 4 Jahre während der Promotion finanziell unterstützt hat.
Fast am Ende dieser Danksagung, gilt mein großer Dank meinem Rückhalt in der Familie. Liebe Mama lieber Papa, und meine lieben Schwestern, ohne eure Liebe und unermüdliche Unterstützung in jeglicher Hinsicht wäre ich heute nicht was ich bin.
Zu guter letzt gilt mein Dank meiner lieben Verena und Valentin, die mir jeden Tag eine große Freude bereiten, und mir insbesondere in den zurückliegenden Monaten den Rücken freigehalten haben und viel auf mich verzichten mussten.